ANALYSIS OF SEISMIC ANISOTROPY PARAMETERS FOR SEDIMENARY ROCKS AND STRATA

A Dissertation Presented to

the Faculty of the Department of Earth and Atmospheric Sciences

University of Houston

In Partial Fulfillment

of the Requirements for the Degree

Doctor of Philosophy

By

Fuyong Yan

December 2015

ANALYSIS OF SEISMIC ANISOTROPY PARAMETERS FOR

SEDIMENARY ROCKS AND STRATA

Fuyong Yan

APPROVED:

Dr. Hua-Wei Zhou, Chairman

Dr. De-hua Han, Co-chairman

Dr. Aibing Li

Dr. Yingcai Zheng

Dr. Samik Sil

Dean, College of Natural Sciences and Mathematics

ABSTRACT

The most prominent feature of sedimentary basins is often its layered structure. The effective elastic properties of the layered media are anisotropic. Mudstones account for most of the volume of the sedimentary rocks, and the elastic properties are usually approximated by transverse isotropy. Therefore, seismic anisotropy is very important for exploration geophysics. Study of the relationships between the anisotropy parameters may supply very useful constraints for the estimation of the anisotropy parameters and be critically important for simplification of the problems in anisotropic-seismic-data processing and interpretation.

Based on the theory of anisotropic elasticity and observation from the mechanical measurements on mudstones, tight physical constraints on c_{13} by c_{11}, c_{33}, and c_{66} are derived. The physical constraints on c_{13} are used to evaluate the quality control of the laboratory anisotropy-measurement data from the literature. It is found that there are significant uncertainties in the determination of c_{13} and δ. When the measurement data of bad quality control are identified and discarded, the intrinsic relationship between c_{13} and other TI elastic constants, and the relationship between δ and the other Thomsen parameters are revealed. Considering the difficulty and significant uncertainty in

laboratory anisotropy-measurements, a practical and robust method for laboratory determination of c_{13} and δ is proposed.

Based on laboratory ultrasonic-measurement data of sedimentary rocks and using Monte Carlo simulation and Backus averaging, the layering effects on seismic anisotropy are analyzed. If the sedimentary strata consist of fully brine-saturated isotropic rocks, δ is usually negative; and if the sedimentary strata are gas bearing, δ increases. For an effective TI medium consisting of isotropic layers, c_{13} can be determined by other TI elastic constants; and therefore, δ can be predicted from the other Thomsen parameters with confidence.

The layering effects on seismic anisotropy at the high-frequency limit are compared with those at the low-frequency limit. Relative to the Backus averaging, ray theory usually underestimates the Thomsen parameters ε and γ and overestimates δ. For the sedimentary strata consisting of isotropic layers, the differences are very significant.

ACKNOWLEDGEMENTS

First of all, I want to thank my supervisor, Dr. De-hua Han, for his continuous encouragements and advice during my research. Most of all, I would like to express my deepest gratitude to Dr. Han for guiding me into academic research and for his generous help in my personal life. Without his help, my life might be on a completely different track. In addition, I would like to thank him for giving me the trust and freedom in exploring the exciting and important field of seismic-rock physics. I do have fun in the research. In short, thank you very much, Dr. Han.

I would also like to thank my doctoral committee chair, Dr. Hua-Wei Zhou, and the committee members, Dr. Aibing Li, Dr. Yingcai Zheng, and Dr. Samik Sil for their advice, time, and commitment. Their constructive suggestions and reviews of this dissertation are greatly appreciated.

I would like to acknowledge the Rock Physics Laboratory at the University of Houston and all researchers working there. I would like to thank my former colleagues, Huizhu Zhao, Dr. Qiuliang Yao, and a current colleague, Min Sun, for many beneficial discussions and aid in the research and laboratory measurements. Min Sun, also my office mate, is the nicest person I know in the world. Thank you for many things and I wish you all the best, Min Sun.

Finally, I am most indebted to my wife Donna and daughter Zoe, for their patience and encouragement. Without their support and sacrifice, I would not be able to enjoy my academic life.

TABLE OF CONTENTS

Chapter 7

LIST OF FIGURES

Chapter 1

Introduction

1.1 Motivation

Transverse isotropy is the most important type of anisotropy and has general applicability in geophysical problems (Anderson, 1989). Transverse isotropy can be caused by the layering effect and preferred alignment of minerals, cracks, or fractures. In the global scale, the generally used preliminary reference earth model (Dziewonski and Anderson, 1981) includes an alternative anisotropic model for the top 220 km section. When the velocity of a geological model is approximated as a function of depth, the effective elastic property is transversely isotropic and scale dependent. As it can be observed from the outcrops and seismic sections, the most prominent feature of sedimentary basins is often its layered structure. The effective elastic properties of the layered media are anisotropic. Mudstones or shales account for most of the volume of the sedimentary rocks, and the elastic properties are usually described by transverse isotropy. The hydrocarbon resources are usually stored in sedimentary basins. Therefore, seismic anisotropy is important for both global geophysics and exploration geophysics.

In geophysical problems, there is often a trade-off between accuracy and simplicity. Compared to isotropy, three extra parameters are introduced in transverse isotropy. It is often challenging to solve the geophysical problem when isotropic elastic properties are assumed; introducing three more parameters quite often will make the problem more complicated. Although theoretically, the five TI elastic constants are independent variables, for the natural rocks with transverse isotropy, good correlations often exist between c_{11} and c_{66}, and between c_{33} and c_{44}. If we could find good correlations between c_{13} and the other elastic constants, the geophysical problem may be greatly simplified. This is one of the primary goals of this study.

The most important and convenient method to study the anisotropic properties of sedimentary rocks is laboratory measurements, especially the ultrasonic-velocity-anisotropy measurements. Compared to the traditional ultrasonic-velocity measurements, velocity-anisotropy measurements are not simply to measure more velocities in different directions. For a reliable measurement of c_{13} and the Thomsen parameter, δ, it is critical to understand the differences between the phase angle and group (ray) angle, and between the phase velocity and the group (ray) velocity, and the strict requirements on the dimensions of the piezoelectric transducers and the sample. Designing an efficient and robust setup for velocity-anisotropy measurements is another goal of this study.

In laboratory anisotropy measurements, the dimensions of the sample are known and the measurement directions are controllable, but there are still significant uncertainties in determining the anisotropy parameters. In estimating the anisotropy parameters from

field-seismic data, there may be more uncertainties and limitations since we do not know the geometry of the subsurface media and the measurement directions are limited. It would be worthwhile to evaluate the uncertainties in estimating the anisotropy parameters from seismic data.

Since the layered structure is the most prominent feature of sedimentary basins, it is important to study the characteristics of seismic anisotropy caused by the layering effect. The layering effect on seismic anisotropy is also frequency dependent. The laboratory anisotropy-measurement utilizes ultrasonic waves whose central frequencies are much higher than those of the seismic waves. The seismic waves usually detect the effective properties of the sedimentary strata, but ray theory is often used to estimate the anisotropy parameters from seismic data. Therefore, it is important to study the differences in the layering effect on seismic anisotropy at the low-frequency limit and at the high-frequency limit.

1.2 State of Art

Thomsen (1986) defined a set of parameters (ε, γ, and δ) and brought up weak anisotropy approximations for the phase velocities in a transversely isotropic (TI) medium. These parameters and the linearized approximations are widely accepted and applied in the industry. With increasing importance of organic shale as a reservoir rock, laboratory anisotropy measurements on core plugs are done routinely. The results are usually reported in terms of the Thomsen parameters (Vernik and Nur, 1992; Johnston, 1995; Vernik and Liu, 1997; Jakobsen and Johansen, 2000; Sondergeld et al., 2000; Wang, 2002; Sondergeld and Rai, 2011; Sone, 2012; Yan et al., 2012). Of the three

parameters, δ is one of the most important parameters for an exploration geophysicist since it describes the relationship between the vertical velocity and the normal-moveout velocity (Thomsen, 1986 and Tsvankin, 2012). As Thomsen (1986) pointed out, δ is an "awkward" combination of elastic parameters and its physical meaning is not straightforward. In spite of a large amount of laboratory measurements, our understanding of δ is still not clear (Banik, 1987; Sayers, 2004). The laboratory measurements show that δ has a poor correlation with the other Thomsen parameters and even the rational range of δ is not certain.

In seismic exploration, the dimensions of the seismic source or the seismic signal receiver are much smaller than the subsurface media through which the seismic waves propagate, so they can be treated as a point source and a point receiver. Therefore, the velocity estimated from seismic data is usually the ray velocity (group velocity). Whereas in laboratory measurements, the dimensions of the piezoelectric transducer can make a large difference in velocity-anisotropy measurements (Dellinger, 1991). It would be preferred if we could directly measure the ray velocities at different directions on the core samples. Blum et al. (2012; 2013) used laser technology to measure the elastic anisotropy of a horizontal-shale core plug. When the laser beam hits an optically absorbing surface, part of the energy is absorbed and converted to heat, which leads to a local thermal expansion. The thermal expansion leads to generation of elastic waves in the ultrasonic frequency range. In their measurement, no stress is applied to the horizontal core sample, so the sample can be rotated freely for group-velocity measurements at different angles. This technology is innovative, but the published data

showed unclear first-arrival signals and the measurement results gave abnormally high values of δ. There exists a technical bottleneck in putting the measurement unit into a pressure vessel. Therefore, significant improvements are required to make this method feasible.

Seismic anisotropy can have a significant impact on seismic-data processing and interpretation (Helbig and Thomsen, 2005). The most critical step for anisotropic-seismic-data processing is to estimate the anisotropic parameters. There are different methods for the estimation of the anisotropy parameters. Most of them are based on the assumption of weak or elliptic anisotropy. Xiao (2006) made a comparative study of the different methods of anisotropy-parameter estimations. She found the non-hyperbolic quartic equation formulated by Alkhalifah and Tsvankin (1995) is applicable to TI media of arbitrary anisotropy. It has the best performance among the methods of anisotropy parameter-estimation using the velocity-analysis approach. Many applications of TI anisotropy-parameter estimation are based on this formulation (Alkalifah, 1997; Grechka and Tsvankin, 1998; Toldi et al., 1999; Wang and Tsvankin, 2009). Sil (2013) brought up a methodology to estimate the anisotropy parameters of the horizontal transversely isotropic media.

At various scales, the earth and the subsurface are often modeled as a layered sequence of different constituents. The elastic properties of the layered media can be described by transverse anisotropy and the anisotropic properties are frequency dependent (Postma, 1955; Anderson, 1961; Backus, 1962; Helbig, 1984).

At the low-frequency limit, i.e., when the wavelength is much greater than the layer thicknesses, the effective anisotropic properties of two periodically alternating isotropic layers are described by Postma (1955). Backus (1962) extended the model to any combination of layers with either isotropic or transversely isotropic properties. Schoenberg and Muir (1989) further extended the Backus model to more general cases in which the constituent layers can be any type of anisotropic media. Based on the Backus averaging and Monte Carlo simulation of the layer-cake models for two and three isotropic layers, Berryman (1999) analyzed the relationships among the Thomsen parameters. Berryman's (1999) study showed little indication of correlations between the anisotropy parameters except for the possible range and sign of the parameters. The simulation results were not very helpful for our understanding of the seismic anisotropic properties of the sedimentary rocks.

The frequency effect on seismic velocities in a layered medium was experimentally studied by Marion and Nur (1994). Significant velocity variations are observed when the layer thicknesses are one tenth of the wavelength. The experimental results were theoretically interpreted by Hovem (1995). The studies show the frequency dependence of seismic velocities in the direction of the TI symmetry axis. The low-frequency limit and high-frequency limit of seismic velocities in the TI symmetry axis are represented by the Backus averaging and the Wyllie time-averaging (or ray theory), respectively (Stovas and Bjorn Ursin, 2007). Extra assumptions are usually needed to solve the frequency effect on the elastic anisotropic properties in the non-oblique directions. The assumptions include infinite periodic layers and a plane harmonic wave (Helbig, 1984;

Shapiro, 1994; Potel et al., 1995; Wang and Rokhlin, 2002). These assumptions may not be proper for seismic exploration of sedimentary basins.

Silva and Stovas (2006) compared the equivalent anisotropic properties of a layer-cake model estimated by the Backus averaging and ray theory, respectively. The layer-cake model consists of two isotropic layers with given elastic properties. The study is quite limited due to the oversimplified model and a lack of freedom in parameterization of the layer properties.

1.3 Research Objective and Approach

Of the five independent elastic constants (c_{11}, c_{33}, c_{44}, c_{66}, and c_{13}) of a TI medium, good to excellent mutual correlations are found existing between c_{11}, c_{33}, c_{44}, and c_{66} from laboratory velocity-anisotropy measurements on the hydrocarbon-source rocks (Horne, 2013), although mathematically, they are free independent variables. Nevertheless, the behavior of c_{13} is erratic. The correlations between c_{13} and the other elastic constants are usually poor. This might be due to that the estimation of c_{13} from the oblique-velocity measurement introduces extra uncertainties compared to the traditional ultrasonic-velocity measurement. For hydrocarbon-source rocks with TI anisotropy, the constraints should exist on c_{13} if the elastic properties in the directions perpendicular and parallel to the symmetry axis are known. If we know the relation between c_{13} and other TI elastic constants, the relation between δ and the other Thomsen parameters can be found. Because estimations of c_{11}, c_{33}, c_{44}, and c_{66} are generally reliable, if the physical constraints on c_{13} by other TI elastic constants can be derived, we can now evaluate the uncertainty in the oblique-velocity measurement.

Using the data with the best quality control, we may find the intrinsic relations between c_{13} and the other elastic constants, or δ with other Thomsen parameters. If these correlations are strong, the number of parameters controlling TI anisotropy could be reduced. These relations should have important applications in anisotropic-seismic-data processing and interpretation.

In laboratory velocity-anisotropy measurements, the dimensions of the rock samples are known, and the measuring directions are controllable, but there are significant uncertainties in the estimation of δ. For field-seismic data, we do not know the subsurface geometry and the measuring directions are restricted. It is expected that the estimation of the anisotropic parameters becomes more challenging. Therefore, it is necessary to evaluate the uncertainties and limitations associated with anisotropy-parameter estimation from seismic data. The uncertainties can be evaluated by synthetic-seismic modeling.

The layering effect is one of the most important factors causing seismic anisotropy. The Backus average defines the low-frequency limit of the anisotropy caused by the layering effect, whereas the equivalent anisotropic properties of the layered media at the high-frequency limit can be estimated by ray theory. Based on Monte Carlo simulation of the layered media, the differences in the layering effect on seismic anisotropy at the low- and high-frequency limits can be characterized.

1.4 Chapter Organization and Contribution

My dissertation consists of seven chapters, including an introduction. The chapters are written in the style of a journal paper. Chapter 2 is published in Geophysical Prospecting, 2015.

Chapter 2 discusses the physical constraints on c_{13} and the Thomson parameters δ for shales. The constraints are heuristic bounds based on laboratory observation and physical intuition. The physical constraints can be a tool of quality control for laboratory anisotropy measurements. Various factors that cause significant uncertainty in c_{13} are analyzed. The physical constraints should have potential applications in anisotropic-seismic-data processing.

Chapter 3 discusses the correlations between the TI elastic constants and the correlations among the Thomsen parameters based on the laboratory anisotropy-measurement data from the public literature. When bad data points are identified and discarded, the intrinsic relationship between c_{13} and other TI elastic constants, and the relationship between δ and the other Thomsen parameters are revealed. The relationship between c_{13} and other TI elastic constants may have important geomechanical applications. The correlation between δ and the other Thomsen parameters may have important applications in seismic-data processing and interpretation.

In Chapter 4, a practical and robust method is proposed to determine c_{13} and δ in the laboratory. There are various designs for laboratory anisotropy measurements, but most

of them have significant uncertainties in the estimation of c_{13} and δ. Measurements based on > 6 core plugs is too expensive for an industrial application. The method proposed in this study is economical, robust, and reliable.

Chapter 5 discusses uncertainties in anisotropy-parameter estimation from seismic data. Based on the TI layer-cake model randomly parameterized by the laboratory anisotropy-measurements, the commonly used quartic non-hyperbolic-moveout velocity-analysis was used to estimate seismic-anisotropy parameters. The methodology is tested on its sensitivities to the layering effect, the source-receive offset, the vertical interval velocity error, and the time-picking error. The results show that the methodology is theoretically well-established and it works better for deeper layers and shorter source-receiver offset data. However, in presence of normal-level noises, the estimation of the seismic anisotropy parameters is sensitive to the time-picking error. The uncertainties increase rapidly the deeper the layers. Sensitivity analysis demonstrates the challenges for seismic anisotropy measurements in practical applications.

Chapter 6 discusses the layering effect on seismic anisotropy in sedimentary strata. Although sandstones and carbonate rocks usually have isotropic seismic properties, the layering effect due to compositional and texture variation and the interbedding with shales can cause noticeable seismic anisotropy. If the sedimentary strata consist of only isotropic sedimentary layers and are brine saturated, the δ value for the effective TI medium is usually negative. However, the δ value will increase in gas bearing thin beds. It is found that c_{13} can be determined by other TI elastic constants in an effective

TI medium consisting of isotropic layers. Therefore, δ can be predicted from the other Thomsen parameters with confidence. Based on simulation results, the theoretical expression of δ for an effective TI medium consisting of isotropic sedimentary rocks can be simplified into a neat form with an excellent accuracy and a clear physical meaning.

Chapter 7 discusses the differences in the layer-induced seismic anisotropy of sedimentary strata at both the low-frequency and the high-frequency limits. ε and γ estimated by ray theory are usually less than estimated by the Backus averaging; while δ estimated by ray theory is usually greater than estimated by the Backus averaging. For the sedimentary strata consisting of isotropic layers, the differences in estimated ε and γ by ray theory and the Backus average are very significant. The differences are less significant when shales with intrinsic anisotropy are included.

1.5 References

Alkhalifah T. and Tsvankin I. 1995. Velocity analysis for transversely isotropic media. *Geophysics* **60**, 1550-1566.

Anderson D.L. 1961. Elastic wave propagation in layered anisotropic media. *Journal of Geophysical Research* **66**, 2953-2963.

Anderson D.L. 1989. *Theory of the Earth*, Blackwell Scientific Publications.

Backus G.E. 1962. Long-wave elastic anisotropy produced by horizontal layering. *Journal of Geophysical Research* **67**, 4427-4440.

Banik N. 2012. Effects of VTI anisotropy on shale reservoir characterization, *SPE Middle East Unconventional Gas Conference and Exhibition*, Abu Dhabi, UAE, SPE paper 150269.

Berryman J.G. 1999. Analysis of Thomsen parameters for finely layered VTI media. *Geophysical Prospecting* **47**, 959-978.

Dellinger J.A. 1991. *Anisotropic Seismic Wave Propagation*. Ph.D. thesis, Stanford University.

Dellinger J.A. and Vernik L. 1994. Do traveltimes in pulse-transmission experiments yield anisotropic group or phase velocities? *Geophysics* **59**, 1774-1779.

Dziewonski A.M. and Anderson, D.L. 1981. Preliminary reference earth model. *Physics of the Earth and Planetary Interiors* **25**, 297-356.

Horne S.A. 2013. A statistical review of mudstone elastic anisotropy. *Geophysical Prospecting* **61**, 817-826.

Hovem J.M. 1995. Acoustic waves in finely layered media. *Geophysics* **60**, 1217-1221.

Helbig K. 1984. Anisotropy and dispersion in periodically layered media. *Geophysics* **49**, 364-373.

Jakobsen M. and Johansen T.A. 2000. Anisotropic approximations for mudstones: A seismic laboratory study. *Geophysics* **65**, 1711-1725.

Johnston J.E., and Christensen N.I. 1995. Seismic anisotropy of shales. *Journal of Geophysical Research* **100**, 5591-6003.

Marion D., Mukerji T. and Mavko G. 1994. Scale effects of velocity dispersion: From ray to effective medium theories in stratified media. *Geophysics* **59**, 1613-1619.

Potel C., de Belleval J.F. and Gargouri Y. 1995. Floquet waves and classical pane waves in an anisotropic periodically multilayered medium: Application to the validity

domain of homogenization. *Journal of the Acoustical Society of America* **97**, 2815-2825.

Postma G.W. 1955. Wave propagation in a stratified medium. *Geophysics* **20**, 780-806.

Sayers C.M. 2004. Seismic anisotropy of shales: What determines the sign of Thomsen's delta parameter? *SEG Expanded Abstracts*.

Schoenberg M. and Muir F. 1989. A calculus for finely layered anisotropic media. *Geophysics* **54**, 581-589.

Shapiro S.A., Zien H. and Hubra P. 1994. A generalized O'Doherty-Anstey formula for waves in finely layered media. *Geophysics* **59**, 1750-1762.

Sil S., 2013. Fracture parameter estimation from well-log data. *Geophysics* **78**, D129-D134.

Silva M.B.C. and Stovas A. 2009. Correspondence between the low- and high-frequency limits for anisotropic parameters in a layered medium. *Geophysics* **74**, WA25–WA33.

Sone H. 2012. *Mechanical Properties of Shale Gas Reservoir Rocks and Its Relation to In-situ Stress Variation Observed in Shale Gas Reservoirs*. Ph.D. thesis, Stanford University.

Sone H. 2013. Mechanical properties of shale-gas reservoir rocks−Part 1: Static and dynamic elastic properties and anisotropy. *Geophysics* **78**, D381-D392.

Sondergeld C.H., Rai C.S., Margesson R.W. and Whidden K.J. 2000. Ultrasonic measurement of anisotropy on the Kimmeridge Shale. *SEG Expanded Abstracts*.

Sondergeld C.H. and Chandra S.R. 2011. Elastic anisotropy of shales. *The Leading Edge* **30**, 325-331.

Stovas A. and Ursin B. 2007. Equivalent time-average and effective medium for periodic layers, *Geophysical Prospecting* **55**, 871-882.

Thomsen L. 1986. Weak elastic anisotropy. *Geophysics* **51**, 1954-1966.

Tsvankin I. 2012. *Seismic Signatures and Analysis of Reflection Data in Anisotropic Media*. 3rd edition, SEG.

Vernik L. and Nur A. 1992. Ultrasonic velocity and anisotropy of hydrocarbon source rocks. *Geophysics* **57**, 727-735.

Vernik L. and Liu X. 1997. Velocity anisotropy in shales: A petrophysical study. *Geophysics* **62**, 521-532.

Wang L. and Roklin S.I. 2002. Floquet wave ultrasonic method for determination of single ply moduli in multidirectional composites. *Journal of the Acoustical Society of America.* **112**, 916-924.

Wang Z. 2002a. Seismic anisotropy in sedimentary rocks, part 1: A single-plug laboratory method. *Geophysics* **67**, 1415-1422.

Wang Z. 2002b. Seismic anisotropy in sedimentary rocks, part 2: Laboratory data: *Geophysics* **67**, 1423-1430.

Chapter 2

Physical Constraints on c_{13} and Thomsen Parameter δ for Shales

2.1 Abstract

Based on the theory of anisotropic elasticity and observation from mechanical measurements on the transversely isotropic hydrocarbon-source rocks or rock-like materials, we reasoned that one of the three principal Poisson's ratios of transversely isotropic hydrocarbon-source rocks should always be greater than the other two and they should be generally positive. From these relations we derived tight physical constraints on c_{13}, the Thomsen δ parameter, and the anellipticity parameter η. Some of the published data from laboratory velocity-anisotropy measurements lie outside of these constraints. These outliers are primarily caused by the substantial uncertainties associated with oblique-velocity measurements. These physical constraints will be useful for our understanding of δ, data quality checking, and predicting δ from measurements perpendicular and parallel to the TI

[1] This chapter is published in *Geophysical Prospecting*, 2015. doi: 10.1111/1365-2478.12265

symmetry axis. The physical constraints should also have potential applications in anisotropic-seismic-data processing.

2.2 Introduction

Thomsen (1986) defined a set of parameters (ε, γ and δ) and proposed weak anisotropy approximations for phase velocities in a transversely isotropic (TI) medium. These parameters and the linearized approximations are widely accepted and used in the industry. With increasing importance of organic shale as a reservoir rock, laboratory measurements on velocity anisotropy of core plugs are done routinely. The results are usually reported in terms of Thomsen parameters (Vernik and Nur, 1992; Johnston, 1995; Vernik and Liu, 1997; Jakobsen and Johansen, 2000; Sondergeld et al., 2000; Wang, 2002; Sondergeld and Rai, 2011; Sone, 2012). Of the three parameters, δ is one of the most important parameters for exploration geophysicist since it describes the relationship between the vertical velocity and the normal-moveout velocity (Thomsen, 1986; Tsvankin, 2012). As Thomsen (1986) pointed out that δ is an "awkward" combination of elastic parameters and its physical meaning is not straightforward. In spite of a large amount of laboratory measurement, our understanding of the parameter δ is still not clear (Banik, 1987; Sayers, 2004). The laboratory measurement found that δ has a poor correlation with the other Thomsen parameters, and even the rational data range of δ is not certain.

Of the five independent elastic constants (c_{11}, c_{33}, c_{44}, c_{66}, and c_{13}) of a TI medium, although theoretically, they are free independent variables, good to excellent mutual

correlations are found existing between c_{11}, c_{33}, c_{44}, and c_{66} from laboratory velocity-anisotropy measurements on hydrocarbon-source rocks. Nevertheless, behavior of c_{13} is erratic. The correlations between c_{13} and the other elastic constants are usually poor. This might be because the estimation of c_{13} from oblique-velocity measurement introduces extra uncertainties compared to traditional ultrasonic measurement. We believe that, for transversely isotropic hydrocarbon-source rocks, there should exist some forms of constraints on c_{13} if the elastic properties in directions perpendicular and parallel to the symmetry axis are known. If we know behavior of c_{13}, we can constrain δ.

2.3 Theory

Young's modulus (E) and Poisson's ratio (ν) are basic parameters used to describe the mechanical properties of materials. For an isotropic medium, from the definitions and using Hooke's law, they are related to the elastic constants as follows (Mavko et al., 1998):

$$E=\frac{9K\mu}{3K+\mu}, \quad \nu=\frac{3K-2\mu}{2(3K+\mu)}=\frac{3\lambda}{2(3K+\mu)}, \tag{2.1}$$

where K is the bulk modulus, μ is the shear modulus, and λ is the Lame parameter. The theoretical value of ν lies between [-1, 0.5] (Landau and Lifshitz, 1970; Thomsen, 1990; Carcione and Cavallili, 2002). The Poisson's ratio of a common natural material is positive. Materials of negative materials were believed to be non-existing (Landau and Lifshitz, 1970), but they do exist. Materials of negative

Poisson's ratio are called "auxetic" materials and have important applications nowadays (Evans et al., 1991; Greaves et al., 2011). Most of the auxetic materials are synthetic materials and have special network structures. Figure 2.1 shows one of the deformation mechanisms leading to a negative Poisson's ratio. This kind of network structure is rarely found in natural rocks. For natural isotropic rocks, the practical limits of Poisson's ratios are given as 0 at the low side and is theoretically by 0.5 at the high side (Gercek, 2007).

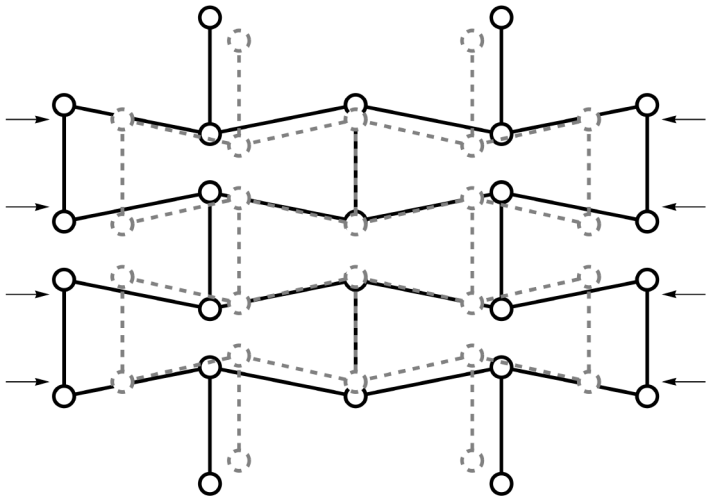

Figure 2.1 Network structure of a material with negative Poisson's ratio (After Lakes, 1991 and Dimitritiv et al., 2001). Grey dashed lines and circles represent the deformed network under axial compression.

The concepts of Young's modulus and Poisson's ratio can be straightforwardly extended to a TI medium using Hooke's law (King, 1964; Banik, 2012). Their relations with the elastic constants are as follows:

$$E_V=\frac{c_{33}(c_{11}-c_{66})-c_{13}^2}{c_{11}-c_{66}} \qquad (=E_3), \tag{2.2}$$

$$E_H=\frac{4c_{66}(c_{33}(c_{11}-c_{66})-c_{13}^2)}{c_{11}c_{33}-c_{13}^2} \qquad (= E_1=E_2), \tag{2.3}$$

$$\nu_V = \frac{c_{13}}{2(c_{11}-c_{66})} \qquad (= \nu_{31} = \nu_{32}), \tag{2.4}$$

$$\nu_{HV}=\frac{2c_{13}c_{66}}{c_{11}c_{33}-c_{13}^2} \qquad (= \nu_{13} = \nu_{23}), \tag{2.5}$$

$$\nu_{HH} = \frac{c_{33}(c_{11}-2c_{66})-c_{13}^2}{c_{11}c_{33}-c_{13}^2} \qquad (= \nu_{12} = \nu_{21}). \tag{2.6}$$

The coordinate system used for the notation is shown in Figure 2.2.

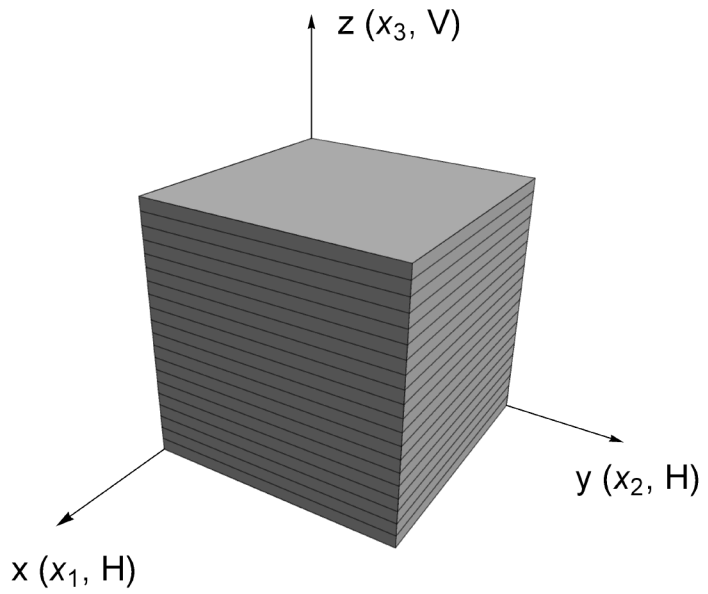

Figure 2.2 The right-hand coordinate system used for the notation in this study.

An important relation exists between ν_V and ν_{HV}:

$$\frac{\nu_{HV}}{\nu_V} = \frac{E_H}{E_V}. \tag{2.7}$$

For hydrocarbon-source rocks with TI anisotropy, the Young's modulus in the horizontal direction (parallel to the bedding direction) should always be greater than along the TI symmetry axis ($E_H > E_V$), so that $\nu_{HV} > \nu_V$.

2.4 Physical Constraints on c_{13} and δ

Figure 2.3 shows the schematic views of the deformation of a vertical plug and a horizontal plug of organic shales under axial compression test. From the left panel, the transversal deformation is identical in every direction, and there is only one Poisson's ratio (ν_V). It is physically intuitional that the plug will not shrink transversely under axial compression, and ν_V is positive. From equation (2.4) and $c_{11} > c_{66}$ for a TI medium (Dellinger, 1991), we get

$$c_{13} > 0. \tag{2.8}$$

In the right panel of Figure 2.3, when a horizontal plug is under uniform axial compression, the deformation in the transversal directions will not be uniform. There are two principal Poisson's ratios: ν_{HH} and ν_{HV}. Since the hydrocarbon-source rocks are usually stiffer in the horizontal direction (along the bedding) than in the vertical direction (perpendicular to the bedding) ($E_H > E_V$), when under axial

compression, the rock is more resistant to deformation (expansion) in the horizontal direction than in the vertical direction. Thus we have $\nu_{HH} < \nu_{HV}$. If there are fractures perpendicular to the bedding, it may lead to $\nu_{HH} > \nu_{HV}$. In this case, the effective medium does not belong to a TI medium. The TI media we considered here are referred to the clastic sediments with TI anisotropy primarily caused by preferred orientation of minerals and cracks. If a horizontal plug of this type of media is under uniform axial compression, the passive expansion in the transverse direction is a matter of more (perpendicular to the bedding) or less (along the bedding). There is no compressional force in the transverse directions according to the definition of Poisson's ratio. The rock does not have the special network structure leading to a negative Poisson's ratio. Therefore, there should be no shrinkage in the transverse directions. From the above analysis, for hydrocarbon-source rocks with TI anisotropy, we have:

$$0 < \nu_{HH} < \nu_{HV}. \tag{2.9}$$

This inequality is the fundamental relation to be used for derivation of the physical constraints on c_{13}. It is validated by laboratory static measurement, as shown in Figure 2.4. There is an obvious pattern of $0 < \nu_{HH} < \nu_{HV.}$ Most of the samples are from organic shales. Sone's data (Sone, 2012) are all static measurement on organic shales. Each pair of ν_{HH} and ν_{HV} is measured on a single horizontal plug. Several samples of synthetic rock-like materials with TI anisotropy are included to demonstrate ν_{HV} can be higher than the high limit of Poisson's ratio (0.5) for an

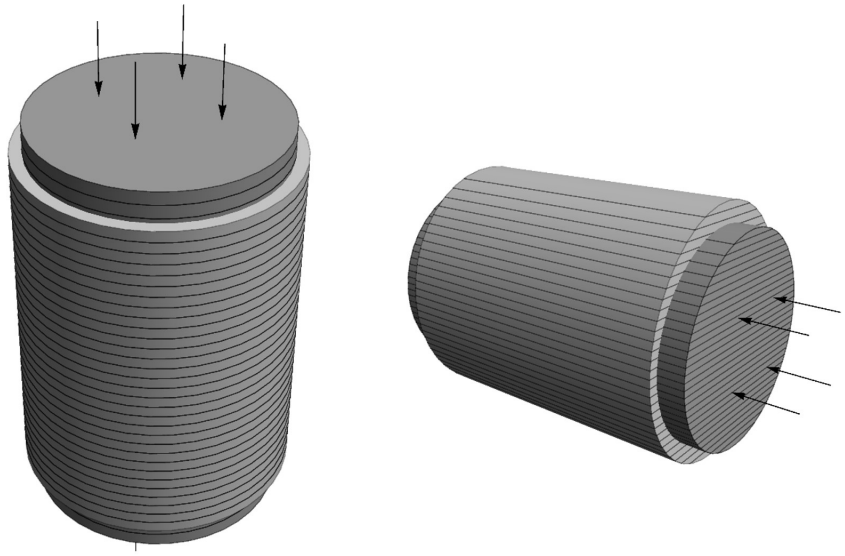

Figure 2.3 Schema of deformation of a vertical plug (left) and a horizontal plug (right) of organic shale under axial compression testing. Dark gray represents the plugs before deformation and light gray represents the plugs after deformation.

isotropic medium. If a TI medium is infinitely stronger in the horizontal direction compared to the vertical direction, then $\nu_{HV} \rightarrow 1$. The two data points showing ν_{HH} slightly higher than ν_{HV} might be caused by measurement uncertainty, and it is possible that the material should not be classified as a TI medium. We have discussed with Hiroki Sone the measurement uncertainty associated with the data point having higher ν_{HH} than ν_{HV}. This data point is from Barnett-2 (Sone, 2012; Sone, 2013). It has a dry bulk density of about 2.65 g/cc and has weak anisotropy. It is the stiffest rock in his data set, which means there might be a larger error in the estimation of the strains and the Poisson's ratios. The difference between ν_{HH} and ν_{HV} is not significant and can be treated as a measurement error.

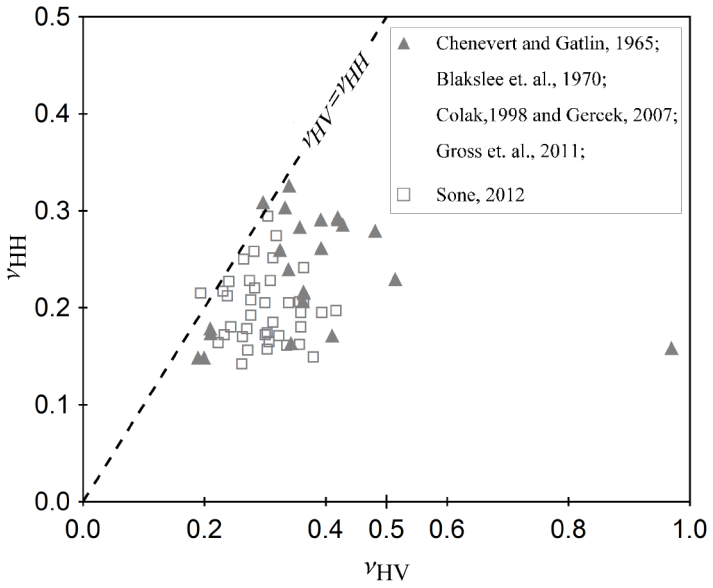

Figure 2.4 Static mechanic measurement of Poisson's ratios on organic shales and rock-like materials with TI anisotropy.

From equations (2.5) and (2.8) and $\nu_{HV} > 0$, we have

$$c_{11}c_{33} - {c_{13}}^2 > 0. \tag{2.10}$$

From equations (2.6) and (2.10) and $\nu_{HH} > 0$, if c_{13} is a real number and exists, we must have c_{11}-$2c_{66} > 0$, and we also have

$$c_{13} < \sqrt{c_{33}(c_{11} - 2c_{66})}. \tag{2.11}$$

From equations (2.5), (2.6), and (2.10) and $\nu_{HH} < \nu_{HV}$, we have

$$c_{13} > \sqrt{c_{33}(c_{11} - 2c_{66}) + {c_{66}}^2} - c_{66}. \tag{2.12}$$

Combining equations (2.11) and (2.12), we put the constraints on c_{13} for hydrocarbon-source rocks in a neat form:

$$\sqrt{c_{33}c_{12} + {c_{66}}^2} - c_{66} < c_{13} < \sqrt{c_{33}c_{12}}. \tag{2.13}$$

When transverse isotropy reduces to isotropy ($c_{11} \rightarrow c_{33}$ and $c_{66} \rightarrow c_{44}$), the low bound equals c_{33}-2c_{44} (for isotropic medium: c_{13}=c_{33}-2c_{44}), and the upper inequality reduces to

$$K - \frac{2}{3}\mu > 0 \text{ or } \lambda > 0\,, \tag{2.14}$$

which is consistent with the practical limits of Poisson's ratio for natural isotropic rocks we discussed earlier in this study.

δ is defined as (Thomsen, 1986):

$$\delta = \frac{(c_{13} + c_{44})^2 - (c_{33} - c_{44})^2}{2c_{33}(c_{33} - c_{44})}. \tag{2.15}$$

If δ is treated as a function of c_{13}, the general shape of the curve is a parabolic curve concaving upward, as shown in Figure 2.5. Here we assume c_{33}>c_{44}, which means that the P-wave velocity is greater than the S-wave velocity in the TI symmetry direction. It can be seen that δ monotonically increases with c_{13} when c_{13}>-c_{44}; thus, substituting the inequalities (2.13) into equation (2.15) and using Thomsen's (1986) notation, we can get the constraints for δ

$$\delta^- < \delta < \delta^+, \tag{2.16}$$

where

$$\delta^{-} = \frac{\varepsilon - 2r_0{}^2\gamma\left(1 - r_0{}^2(1+2\gamma) + \sqrt{\left(1 - r_0{}^2(1+2\gamma)\right)^2 + 2\varepsilon}\right)}{1 - r_0{}^2},$$

$$\delta^{+} = \frac{\varepsilon - 2r_0{}^2\gamma + r_0{}^2\sqrt{1 - 2r_0{}^2(1+2\gamma) + 2\varepsilon}}{1 - r_0{}^2},$$

where $r_0=\beta_0/\alpha_0$, β_0 and α_0 are the shear velocity and P-wave velocity along the TI symmetry axis, respectively. ε and γ are defined by (Thomsen, 1986)

$$\varepsilon = \frac{c_{11} - c_{33}}{2c_{33}}, \qquad \gamma = \frac{c_{66} - c_{44}}{2c_{44}}. \tag{2.17}$$

One sees that δ is constrained by the other Thomsen parameters, which are all properties in the directions perpendicular and parallel to the TI symmetry axis.

Alkhalifah and Tsvankin (1995) defined an "anellipticity" parameter (η) that describes the degree of deviation from elliptic anisotropy:

$$\eta = \frac{\varepsilon - \delta}{1 + 2\delta}. \tag{2.18}$$

The anellipticity parameter η is important for anisotropic-seismic-data processing because it determines the relation between the normal-moveout velocity and the horizontal velocity (Tsvankin 2012). In terms of elastic constants, it is equal to

$$\eta = \frac{1}{2}\left(\frac{c_{11}(c_{33} - c_{44})}{(c_{13} + c_{44})^2 + c_{44}(c_{33} - c_{44})} - 1\right). \tag{2.19}$$

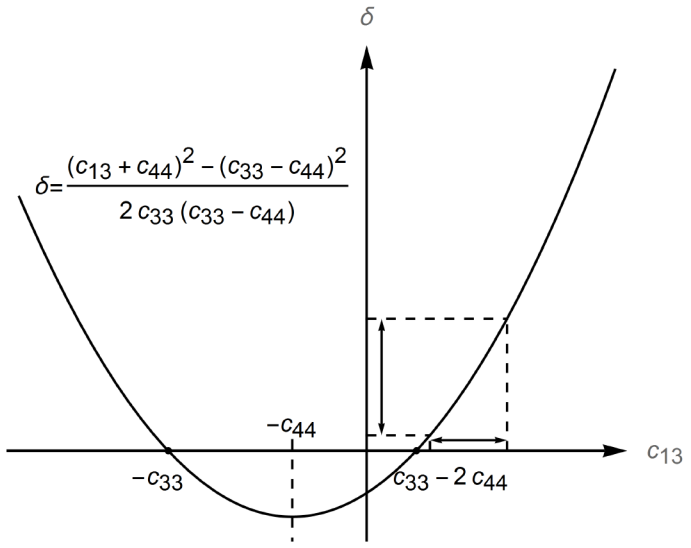

Figure 2.5 Relationship between the constraints on c_{13} and the constraints on δ. (Parameters used for illustration: c_{11}=70GPa, c_{33}=40GPa, c_{44}=15GPa, and c_{66}=25GPa).

Similarly, as shown in Figure 2.6, if we know the constraints on c_{13}, constraints on the anellipticity parameter η can also be determined by substituting the inequalities (13) into equation (2.19):

$$\eta^- < \eta < \eta^+. \tag{2.20}$$

where

$$\eta^- = \frac{r_0{}^2((\varepsilon - 2\gamma) + \sqrt{1 - r_0{}^2(1 + 2\gamma) + 2\varepsilon}))}{r_0{}^2(1 + 4\gamma) - (1 + 2\varepsilon) - 2r_0{}^2\sqrt{1 - 2r_0{}^2(1 + 2\gamma) + 2\varepsilon}},$$

$$\eta^+ = \frac{r_0{}^2((\varepsilon - 2\gamma) + 2\gamma(r_0{}^2(1 + 2\gamma) - \sqrt{(1 - r_0{}^2(1 + 2\gamma))^2 + 2\varepsilon}))}{r_0{}^2(1 + 4\gamma) - (1 + 2\varepsilon) - 4r_0{}^2\gamma(r_0{}^2(1 + 2\gamma) - \sqrt{(1 - r_0{}^2(1 + 2\gamma))^2 + 2\varepsilon})}.$$

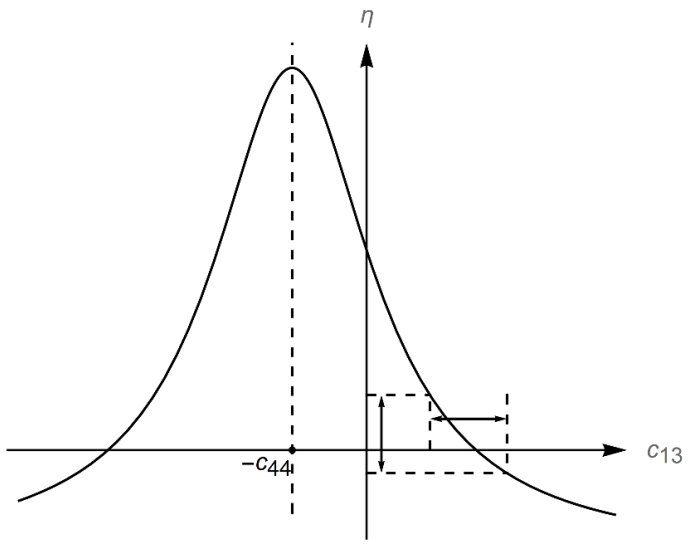

Figure 2.6 Relation between the constraints on c_{13} and the constraints on the anellipticity parameter η (Parameters used for illustration: c_{11}=70GPa, c_{33}=40GPa, c_{44}=15GPa, and c_{66}=25GPa).

It can also be derived by substituting the constraints on δ (equation (2.16)) directly into equation (2.18). Obviously, the high bound of δ corresponds to the low bound of η.

2.5 Laboratory Data and the Constraints

Figure 2.7 shows the crossplot between δ and v_{HH}/v_{HV} ratio from the dynamic velocity-anisotropy measurements. The data sources are from Thomsen (1986), Johnston and Christensen (1995), Vernik and Liu (1997), Jakobsen and Johansen (2000), Wang (2002b, shale and coal samples only), and Sone (2012, 2013). The data collected by Thomsen (1986) are from various sources; only data points with anisotropy stronger than the measurement uncertainty ($\varepsilon > 0.03$ and $\gamma > 0.03$) are

included. Wang's data are corrected for mistaking group velocity for phase velocity in the oblique direction. If there is a pressure-dependent measurement, no more than three data points are used for the same sample to prevent the overweighting effect of this sample. The crossplot is divided into three areas. In the left, several data points have negative v_{HH} values. The corresponding c_{13} are above the high bound and they tend to have higher values of δ. In the right area, there are quite a few points with $v_{HH} > v_{HV}$. The corresponding c_{13} values are lower than the low bound, and they tend to have lower values of δ. About 2/3 of the data points lie in the center area, where it is believed that all hydrocarbon-source rocks with TI anisotropy should lie within. Since there are more data points lying below the low bound than above the high bound, there might be a general tendency of underestimating δ. For clarity, we emphasize that the constraints for c_{13} or δ might be different for each data point. Since these constraints are derived from the relation between the Poisson's ratios, the ratio of Poisson's ratios can be directly used to check whether a data point lies within or outside of the bounds of c_{13} or δ. Next, we will analyze that most of the data points lying outside of the bounds might be due to uncertainty in laboratory velocity-anisotropy measurements.

2.6 Uncertainty in Laboratory Velocity-Anisotropy Measurement

Laboratory velocity-anisotropy measurement on a TI medium requires at least five velocity-component measurements, among which one velocity measurement must be made in an oblique direction. Traditionally this oblique-velocity measurement is made on a 45° plug (the angle between the axial direction of the cylindrical plug

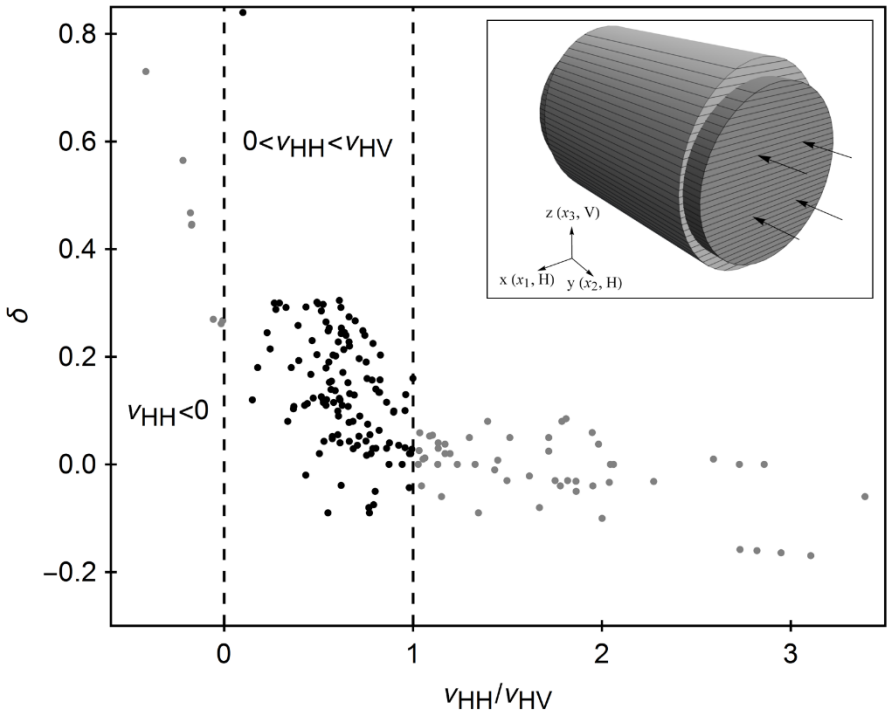

Figure 2.7 Crossplot between δ and v_{HH}/v_{HV} ratio from dynamic velocity-anisotropy measurements. Black points (137) are within the physical bounds and gray points (66) are outside of bounds (Data sources: Thomsen (1986), Johnston and Christensen (1995), Vernik and Liu (1997), Jakobsen and Johansen (2000), Wang (2002b), and Sone(2012; 2013)).

and the TI symmetry axis is 45°). Taking an exact 45° plug is difficult in practice, but people often ignore the angle error because the formula for calculating c_{13} is simple and handy. If the phase angle θ is not equal to 45°, c_{13} should be calculated by

$$c_{13} = 2\csc 2\theta \sqrt{(\rho V_{P\theta}^2 - c_{11}sin^2\theta - c_{44}cos^2\theta)(\rho V_{P\theta}^2 - c_{33}cos^2\theta - c_{44}sin^2\theta)} - c_{44}. \tag{2.21}$$

where $V_{P\theta}$ is the phase velocity. As Yan et al. (2012) pointed out, this small angle error can have a significant effect on the estimation of c_{13} and δ. In Figure 2.8, we take only data points satisfying $0 < v_{HH} < v_{HV}$, and assume that true TI elastic properties are measured. Then taking the phase velocity at phase angles 43°, 40°, and 50°, respectively, as the phase velocity at phase angle 45°, we recalculate c_{13} and check how much difference is made. For display convenience, c_{13} is normalized by

$$c_{13n} = \frac{c_{13} - c_{13}^{-}}{c_{13}^{+} - c_{13}^{-}}, \tag{2.22}$$

where

$$c_{13}^{-} = \sqrt{c_{33}(c_{11} - 2c_{66}) + {c_{66}}^2} - c_{66},$$

$$c_{13}^{+} = \sqrt{c_{33}(c_{11} - 2c_{66})}\ .$$

If $c_{13\mathrm{n}}$ does not lie between 0 and 1, it is outside of the bounds. As we can see in Figure 2.8, a negative 2° angle error makes about 20% of the data points lie below the low bound, a negative 5° angle error makes about 62% of the data points lie below the low bound, and a positive 5° angle error makes about less than 8% of the data points lie above the high bound. In the bottom two panels of Figure 2.8, we show the sensitivity of velocity measurement error on c_{13n}. If the phase velocity in 45° is underestimated by 1%, 22% percent of the data points move below the low bound. If the phase velocity in 45° is overestimate by 1%, only one data point moves

above the high bound. The above sensitivity analyses demonstrate why there are more data points lying below the low bound than above the high bound, as shown in Figure 2.7.

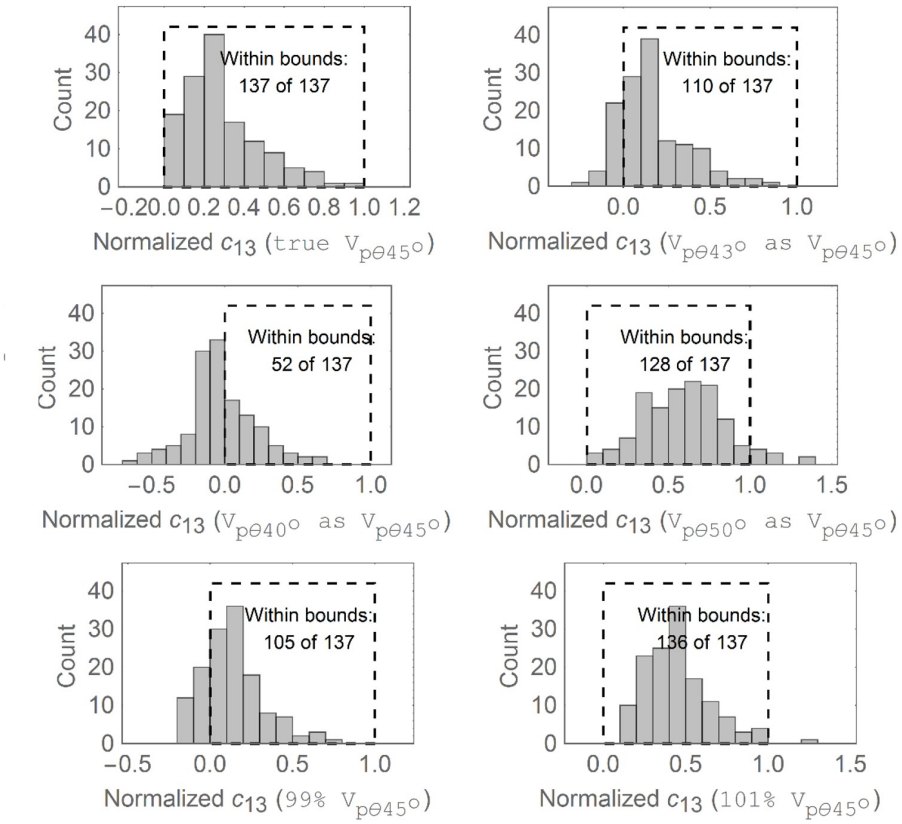

Figure 2.8 Sensitivity analysis: Effect of angle error and velocity error on the estimation of c_{13}.

Another important issue is the difference between the group and phase velocities. Dellinger and Vernik (1994) discussed related problems associated with traditional triple-plug velocity-anisotropy measurements. Using Snell's law for TI media (Slawinski et al., 2000), Figure 2.9 shows the ray tracing of ultrasonic-velocity

measurement on a 45° plug. In TI media, Snell's law is still consistent with Fermat's principle; that is to say that, between the emission transducer plane and receiver transducer plane, the ray with minimum travel time (the vertical incident ray) obeys Snell's law, and it does not necessarily have the shortest path. If the transducer is not wide enough (or the sample is too long), the first arriving energy might be missed. Thus the phase velocity tends to be underestimated. In practice, the transducers need to be at least 10% wider than the minimum width so that the first-arrival signal can be strong enough for reliable break-time picking. After c_{11}, c_{33}, and c_{44} are known, from the non-oblique-velocity measurement, c_{13} can be calculated by

$$c_{13} = \sqrt{(2\rho V_{P\theta 45}^2 - c_{11} - c_{44})(2\rho V_{P\theta 45}^2 - c_{33} - c_{44})} - c_{44}. \qquad 2.23)$$

where $V_{P\theta 45}$ is the 45° phase velocity. In practice, the second term under the square root signal should always be positive, which requires the first term must be positive as well (If not, c_{13} will be a complex number). Therefore, underestimation of the phase velocity $V_{P\theta 45}$ will cause underestimation of c_{13}, and sometimes, it even leads to a negative or even complex value of c_{13}. As shown in Figure 2.5, δ is positively correlated with c_{13}, so it will be underestimated as well. Most of the velocity-anisotropy data cited in this study are measured on cylindrical plugs of one-inch diameter. The lengths of the plugs are often around 4 cm, can be longer if the plugs are also needed for static measurements. Therefore, there might be a bias toward underestimation of c_{13} in the published velocity-anisotropy measurement data.

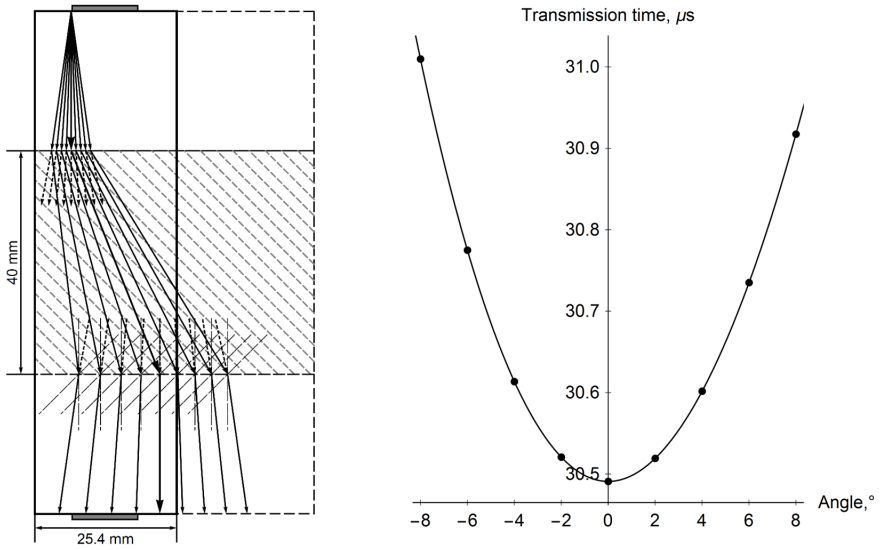

Figure 2.9 Use of Snell's law to simulate ultrasonic-velocity measurements on a 45° plug with one-inch diameter. The transducer dimension (diameter) is 12 mm. The left panel shows the ray tracing from the left corner of the top transducer and right panel shows the corresponding transmission travel times of different rays. In the TI medium, the dashed arrow denotes the phase direction and the solid arrow denotes the ray direction. The long dashed gray line denotes the TI symmetry or reflection symmetry plane. The TI elastic properties are taken as the first sample (at 8634 feet) from the dataset by Vernik and Liu (1997). The right panel shows the transmission travel time of rays in the left panel. The minimum travel time is for the vertical incident ray (with longest arrowhead).

To improve measurement efficiency, Wang (2002a) used a setup based on a single horizontal plug. An oblique-velocity must be measured, which is actually group velocity. To calculate c_{13} and δ, we need to convert the group velocity to phase velocity and find the corresponding phase angle, and then use equation (2.21) to calculate c_{13}. Figure 2.10 shows the group to phase correction effect on c_{13} and δ. It can be seen that if the group velocity is mistook for phase velocity, c_{13} and δ will be systematically underestimated.

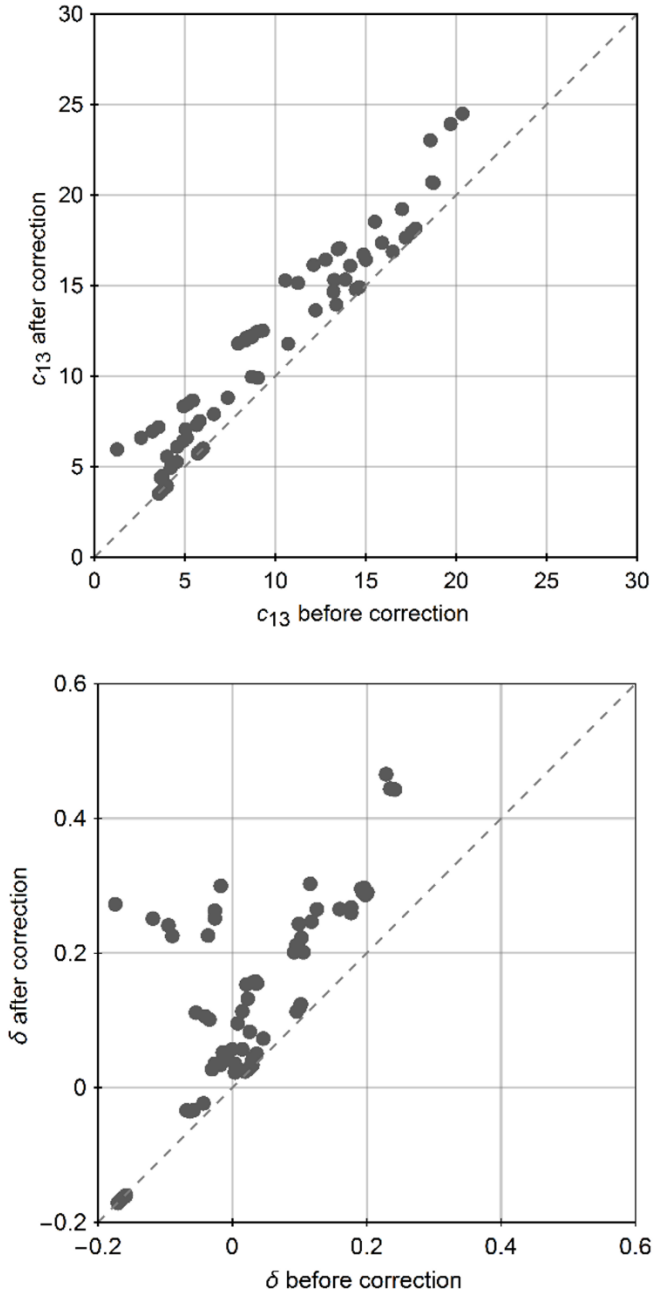

Figure 2.10 Phase to group correction effect on c_{13} (left) and δ (right) using Wang's data (shale and coal samples only, Wang(2002b)).

The above analyses explain that why there are more data points lying below the physical constraints of c_{13} and δ than above the constraints. The data points out of the bounds might be also due to some other factors. For example, the sample has fractures crossing the bedding, which might lead to $v_{HH}>v_{HV}$. Some samples might have significant heterogeneity on the core plug scale. We sometimes find that the "horizontal" plug is not horizontal: The angle between the bedding and the cylindrical plug axial might be more than 5°. In addition, identification of the bedding direction is not always straightforward by naked eyes. In these cases, either the samples do not really belong to a TI medium or the measured elastic properties are apparent properties.

2.7 Applications

The physical constraints can help us understand the effect of other Thomsen parameters on δ. In Figure 2.11, the δ constraints are plotted as a function of β_0/α_0. The range of β_0/α_0 is selected based on laboratory anisotropy-measurements. As can be seen from Figure 2.12(a), the β_0/α_0 ratios for shales are distributed around a narrow range of 0.5-0.7. The curves in different colors represent the δ bounds for different combinations of ε and γ. When ε is constant, δ will increase with decreasing γ; when γ is constant, δ will increase with ε. A small δ occurs when γ is much greater than ε. A high δ occurs when ε is much greater than γ. Although ε and γ are theoretically independent variables, there is often a fairly good correlation between them from laboratory observation (Sayers, 2004).

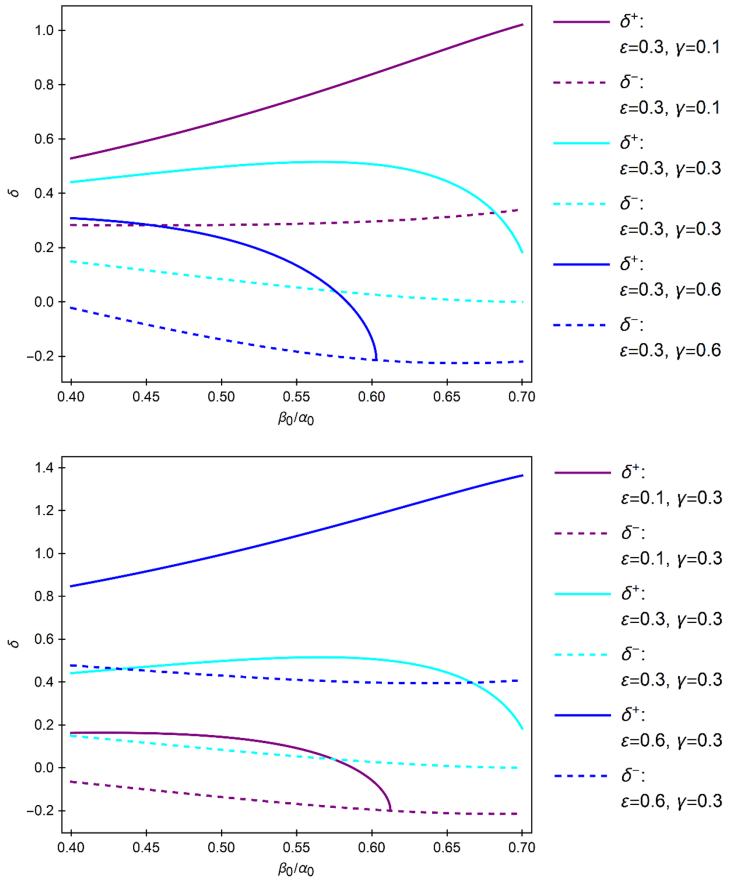

Figure 2.11 Relation between the bounds of δ and ε, γ and ratio of β_0/α_0. Two of the upper bounds terminating when crossing with the low bounds is due to $c_{11} - 2c_{66} < 0$, which might be non-physical.

The constraints are less sensitive to the ratio of β_0/α_0 than the other Thomsen parameters. For display convenience, we assume a constant β_0/α_0 ratio of 0.55, and then plot the measured data with bounds of δ. As shown in Figure 2.13, the trends of the approximated bounds comply well the laboratory-measured data if the data points lying outside of the δ bounds are not displayed. The geometry of the

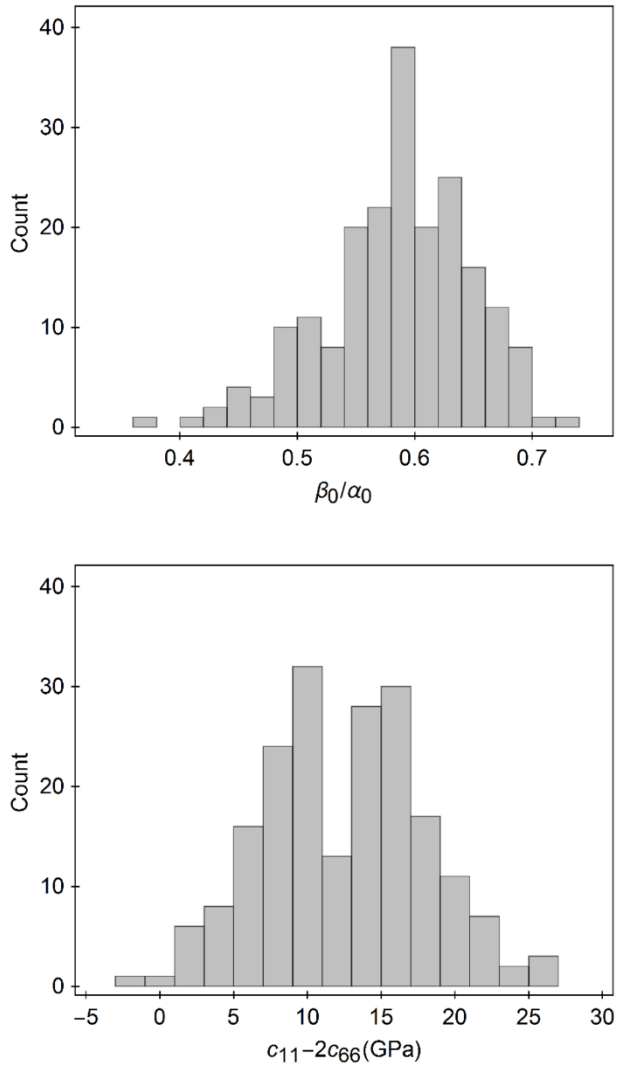

Figure 2.12 Distributions of β_0/α_0 ratio (top) and c_{11}-$2c_{66}$ (bottom) from laboratory anisotropy measurements. Data are from all the points in Figure 2.6.

bounding surfaces also clearly shows the influence of ε and γ on δ. When c_{11}-$2c_{66}$ < 0, the upper bound surface crosses the lower bound surface and disappears.

Figure 2.12 (bottom) shows the histogram of c_{11}-$2c_{66}$ from laboratory velocity-anisotropy measurements. Of total of 203 data points, there are only 2 data points with c_{11}-$2c_{66} < 0$, which are from Thomsen (1986). We trace the data points to the original report (Lin, 1985), and it turns out that one data point is due to data-entry error and the other data point is due to signals of substandard quality. Since c_{11}-$2c_{66} > 0$ is derived simultaneously with the upper constraints of c_{13} (equation (2.11)), the laboratory data validate that our assumption of $v_{HH}>0$ is rational.

Since δ is constrained by the non-oblique properties, it might be possible that we can approximately predict δ without oblique-velocity measurement. In the upper panel of Figure 2.14, using the data points within the bounds, we directly correlate δ with the other Thomsen parameters. Comparing the coefficients before ε, γ, and β_0/α_0 ratio, it is found that δ is more sensitive to ε and γ than the ratio of β_0/α_0; δ is positively correlated to ε and negatively correlated to γ. In the lower panel, we use the bounds of δ (equation (2.16)) to predict δ. Considering there are many data points lying out of the bounds, it is reasonable to believe the data points within the bounds should also have significant uncertainty; thus, the prediction results are encouraging. In addition, the samples come from all over the world and are in different saturation and pressure conditions.

In practical applications of anisotropic-seismic-data processing, the bounds on δ or η might be very useful in constraining estimation of TI parameters from seismic data. For a certain area under study, if a correlation between ε and γ is established,

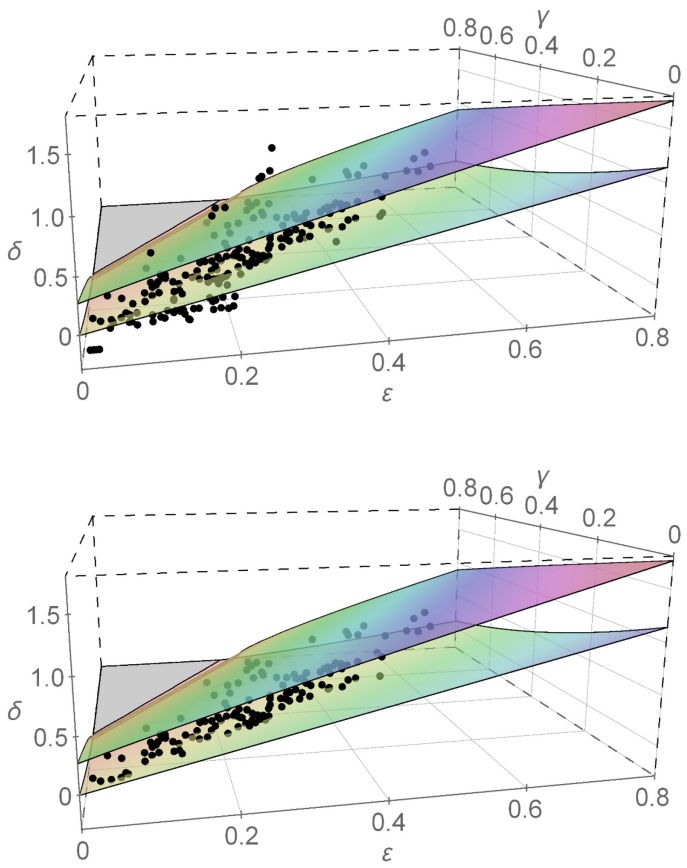

Figure 2.13 Comparison between measured δ and the δ bounds using a constant β_0/α_0 of 0.55. (above, all the data points in Figure 2.6; below, gray data points in Figure 2.6 are removed)

by assuming a certain β_0/α_0 ratio, δ can be estimated as the average of the high bound and low bound.

2.8 Discussion

The physical bounds are proposed with organic shales in mind. They should be applicable to transversely-isotropic sedimentary rocks caused by preferred

orientation of minerals and cracks and the layering effect. The intrinsic factor causing this type of TI anisotropy is the universal law of gravity. Although this type of rocks represent only a specific type of TI media, they are most common and important for oil and gas exploration. If systematic tectonic fractures cutting through the sedimentary rocks layers or beddings significantly affect the elastic properties, they should not be approximated as TI media and the bounds we brought up in this study should not apply. The physical constraints are not applicable to a TI medium with higher Young's modulus along the TI symmetry axis than in direction perpendicular to the symmetry axis. This type of TI medium, although rare, does exist in nature. The basalt rock with column joints (formed by thermal contraction) may be a good example of this type of TI medium. We do not suggest applying the physical constraints to an individual crystal, as special crystal lattice structure may lead to a negative Poisson's ratio in a certain direction.

Since this study is focused on hydrocarbon-source rocks with TI anisotropy, the assumptions about smaller Young's modulus along the TI symmetry axis than in direction perpendicular to the TI symmetrical axis and $c_{33} > c_{44}$ can be treated as well-known knowledge. The basic assumption for derivation of the physical bounds is $0 < \nu_{HH} < \nu_{HV}$, which is validated by reasoning and static laboratory measurements.

Rocks are usually not ideally elastic. The magnitudes of bulk modulus, shear modulus, and Young's modulus can vary depending on the magnitude and frequency of the stress applied. Poisson's ratio might also vary under dynamic and

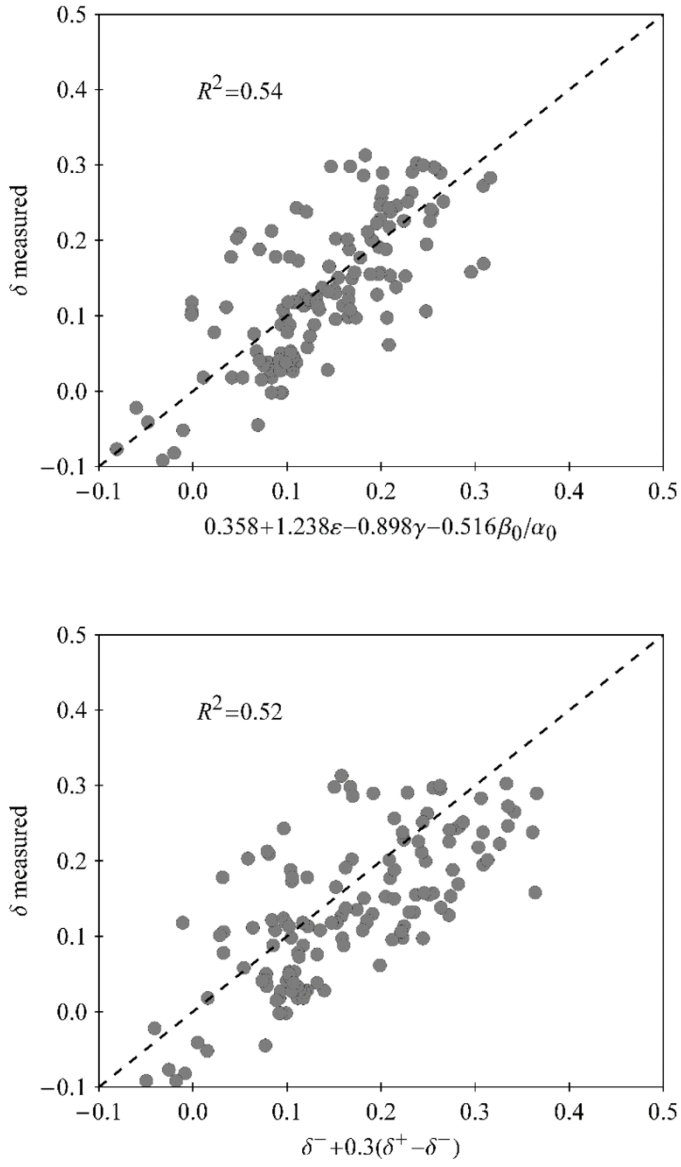

Figure 2.14 Prediction of δ: (a) from other Thomsen parameters and (b) from δ constraints.

static measurements. Nevertheless, the fundamental relations between these parameters once established should be same for both static and dynamic measurements. For example, static measurement shows $c_{11}>c_{66}$. For dynamic

measurement, c_{11} and c_{66} may both be different, but the relation $c_{11}>c_{66}$ should still hold. Figure 2.15 shows the crossplot between ν_{HH} and ν_{HV} for both static measurement and ultrasonic-dynamic measurement using Sone's data (2012, 2013). The organic shale samples come from Barnett, Haynesville, and Eagle Ford shales. The data points from the static measurement and the dynamic measurement are different. The static measurement is based on strain measurements on a single horizontal plug, whereas the dynamic measurement is based on velocity measurements on five cylindrical plugs with 0°, 30°, 45°, 60°, and 90° angles to the TI symmetry axis, respectively. In Figure 2.15, no matter static measurement or dynamic measurement, the overall pattern of $\nu_{HH} < \nu_{HV}$ is same.

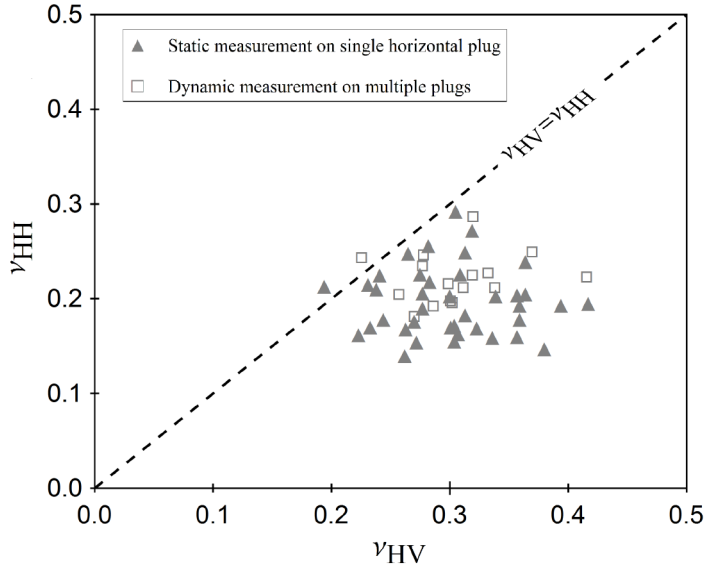

Figure 2.15 Relationship between ν_{HH} and ν_{HV} from static and dynamic measurements on organic shales (data from Sone (2012; 2013)).

The energy constraints on the TI elastic constants are summarized by Dellinger (1991) as:

$$c_{11} > c_{66} > 0, \quad c_{33} > 0, \quad c_{44} > 0, \tag{24}$$

$$c_{13}{}^2 < c_{33}(c_{11} - c_{66}). \tag{25}$$

These constraints are for a general TI medium, which does not specify $c_{11} > c_{33}$, $c_{66} > c_{44}$ and it does not require Young's modulus is lower along the TI symmetry axis than in the direction perpendicular to the TI symmetry axis. The physical constraints on c_{13} we brought up are for a specific type of TI medium which is stiffer along the bedding/layering than the TI symmetry axis and does not have a special network structure leading to negative Poisson's ratio; thus, they are much tighter than the constraints by equations (2.24) and (2.25).

2.9 Conclusions

For hydrocarbon-source rocks with TI anisotropy, the elastic constants c_{13} is constrained by c_{11}, c_{33}, and c_{66}. Therefore, δ and the anellipticity parameter η are constrained by the other anisotropy parameters that can be measured either along or perpendicular to the TI symmetry axis. Using these constraints, we find out that there exist significant uncertainties in laboratory velocity-anisotropy measurements. The physical constraints on δ can help us understand the relationship between δ and the other Thomsen parameters. Generally, δ increases with ε and decreases with increasing γ. Variation of β_0/α_0 of the hydrocarbon-source

rocks in a certain area is usually small, so that δ is less sensitive to β_0/α_0. We also show that δ can be approximated by the other Thomsen parameters. The physical constraints on δ and η should have potential applications on anisotropic-seismic-data processing.

2.10 Acknowledgements

We thank the Fluid and DHI consortium sponsors for supporting the consortium and this study. We also thank Hiroki Sone for sharing his dissertation data and answering our queries regarding the data.

2.11 Reference

Alkhalifah T. and Tsvankin I. 1995. Velocity analysis for transversely isotropic media. *Geophysics* **60**, 1550-1566.

Banik N. 2012. Effects of VTI anisotropy on shale reservoir characterization, *SPE Middle East Unconventional Gas Conference and Exhibition*, Abu Dhabi, UAE, SPE paper 150269.

Blakslee O.L., Proctor D.G., Seldin E.J., Spence G. B. and Weng T. 1970. Elastic constants of compression annealed pyrolytic graphite. *Journal of Applied Physics* **41**, 3373-3382.

Chenevert M.E. and Gatlin C. 1965. Mechanical anisotropies of laminated sedimentary rocks. SPE paper 890.

Carcione J.M. and Cavallini F. 2002. Poisson's ratio at high pore pressure. *Geophysical Prospecting* **50**, 97-106.

Colak K. 1998. *A Study on the Strength and Deformation Anisotropy of Coal Measure Rocks at Zonguldak Basin*. Ph.D. thesis, Zonguldak Karaelmas University, Turkey.

Dellinger J.A. 1991. *Anisotropic Seismic Wave Propagation*. Ph.D. thesis, Stanford University.

Dellinger J.A. and Vernik L. 1994. Do traveltimes in pulse-transmission experiments yield anisotropic group or phase velocities? *Geophysics* **59**, 1774-1779.

Dmitriev S.V., Shigenari T.S., and Abe k. 2001. Poisson ratio beyond the limits of the elastic theory. *Journal of the Physical Society of Japan* **70**, 1431-1432.

Evans K.E., Nkansah M.A., Hutchinson I.J. and Rogers S.C. 1991. Molecular network design. *Nature*, **35**3, 124.

Gercek H. 2007. Poisson's ratio values for rocks. *International Journal of Rock Mechanics & Mining Sciences* **44**, 1-13.

Greaves G.N., Greer A.L., Lakes R.S. and Rouxel T. 2011. Poisson's ratio and modern materials. *Nature Materials* **10,** 823-837.

Gross T.S., Nguyen K., Buck M., Timoshchuk N., Tsukrov I. I., Reznik B., Piat R. and Bohlke T. 2011. Tension-compression anisotropy of in-plane elastic modulus for pyrolytic carbon. *Carbon* **49**, 2141-2161.

Jakobsen M. and Johansen T.A. 2000. Anisotropic approximations for mudstones: A seismic laboratory study. *Geophysics* **65**, 1711-1725.

Johnston J.E., and Christensen N.I. 1995. Seismic anisotropy of shales. *Journal of Geophysical Research* **100**, 5591-6003.

King M.S. 1964. *Wave Velocities and Dynamic Elastic Moduli of Sedimentary Rocks*. Ph.D. thesis, University of California, Berkeley.

Lakes R. 1991. Deformation mechanisms in negative Poisson's ratio materials: Structural aspects. *Journal of Materials Sciences* **26**, 2287-2292.

Landau L.D. and Lifshitz E.M. 1970. *Theory of Elasticity*. Pergamon Press, 2nd Edition.

Lin W. 1985. Ultrasonic velocities and dynamic elastic moduli of Mesaverde rock. Lawrence Livermore National Laboratory. Rep. 20273, rev. 1.

Mavko G., Mukerji T. and Dvorkin J. 1998. *The Rock Physics Handbook*. Cambridge University Press.

Sayers C.M. 2004. Seismic anisotropy of shales: What determines the sign of Thomsen's delta parameter? *SEG Expanded Abstracts*.

Slawinski M.A., Slawinski R.A., Brown R.J. and Parkin J.M. 2000. A generalized form of Snell's law in anisotropic media. *Geophysics* **65**, 632-637.

Sone H. 2012. *Mechanical Properties of Shale Gas Reservoir Rocks and Its Relation to In-situ Stress Variation Observed in Shale Gas Reservoirs*. Ph.D. thesis, Stanford University.

Sone H. 2013. Mechanical properties of shale-gas reservoir rocks−Part 1: Static and dynamic elastic properties and anisotropy. *Geophysics* **78**, D381-D392.

Sondergeld C.H., Rai C.S., Margesson R.W. and Whidden K.J. 2000. Ultrasonic measurement of anisotropy on the Kimmeridge Shale. *SEG Expanded Abstracts*.

Sondergeld C.H. and Chandra S.R. 2011. Elastic anisotropy of shales. *The Leading Edge* **30**, 325-331.

Thomsen L. 1986. Weak elastic anisotropy. *Geophysics* **51**, 1954-1966.

Thomsen L. 1990. Poisson was not a geophysicist. *Geophysics: The Leading Edge of Exploration*, December 1990.

Tsvankin I. 2012. *Seismic Signatures and Analysis of Reflection Data in Anisotropic Media.* 3rd edition, SEG.

Vernik L. and Nur A. 1992. Ultrasonic velocity and anisotropy of hydrocarbon source rocks. *Geophysics* **57**, 727-735.

Vernik L. and Liu X. 1997. Velocity anisotropy in shales: A petrophysical study: *Geophysics* **62**, 521-532.

Wang Z. 2002a. Seismic anisotropy in sedimentary rocks, part 1: A single-plug laboratory method. *Geophysics* **67**, 1415-1422.

Wang Z. 2002b. Seismic anisotropy in sedimentary rocks, part 2: Laboratory data: *Geophysics* **67**, 1423-1430.

Yan F., Han D.-h. and Yao Q. 2012. Oil shale anisotropy measurement and sensitivity analysis. *SEG Expanded Abstracts*.

Chapter 3

Correlations among the Anisotropic Parameters and Its Applications

3.1 Abstract

Estimation of the Thomsen parameters δ from laboratory anisotropy-measurement is challenging due to significant uncertainties in the estimation of the TI elastic constant c_{13}. The physical constraints on c_{13} are used to evaluate the quality control of the available laboratory anisotropy-measurement datasets from the literature. Although the five TI elastic constants are mathematically independent, there exist strong correlations among the TI elastic constants for hydrocarbon-source rocks. A strong correlation is found to exist between c_{13} and c_{11}-2c_{66}. Therefore, the elastic properties of the hydrocarbon-source rocks can be approximated by a special type of transverse isotropy defined by four independent elastic constants. This approximation is found to be more accurate than the elliptic anisotropy approximation. Using datasets of better quality control, a stronger correlation can be found to exist between c_{13} and its physical constraints. This correlation can be used to predict Young's moduli and Poisson's ratios for hydrocarbon-source rocks and may have important geomechanical applications. A

strong correlation is found to exist between δ and the other Thomsen parameters when datasets of good quality control are used. This correlation may have important applications in anisotropic-seismic-data processing and interpretation.

3.2 Introduction

Shales or mudstones account for most of the bulk volume of the sedimentary rocks and are the primary factor of seismic anisotropy in seismic exploration (Schoenberg et al., 1996). The elastic properties of shales are often described by transverse isotropy (Vernik and Nur, 1992; Johnston, 1995; Vernik and Liu, 1997; Jakobsen and Johansen, 2000; Sondergeld et al., 2000; Wang, 2002; Sondergeld and Rai, 2011; Sone, 2012). The challenges of including anisotropy in seismic-data processing and interpretation come from introduction of extra parameters. For isotropic rocks, although the elastic properties are defined by two independent parameters (V_P and V_S), there are often good correlations between them (Castagna et al., 1985). These correlations play an important role in seismic exploration. For the most simple and practical case of transverse isotropy, the elastic properties are defined by five independent elastic parameters. Similar to the isotropic case, if we could find connections among the five independent elastic parameters, it will greatly simplify the problems in anisotropic-seismic-data processing and interpretation.

With increasing importance of shales as reservoir rocks, there are many laboratory studies of the anisotropic properties of shales recently (Sondergeld and Rai, 2011; Sone, 2012; Yan et al. 2012; Blum et al, 2013; Yan et al. 2014; Sarout et al., 2015).

Using various velocity anisotropy data (primarily laboratory core data, and other data from cross-dipole sonic, cross well and walkaway VSP), Horne (2013) statistically studied the relationships among the anisotropic parameters. It is found that c_{11} and c_{66}, c_{33} and c_{44} have good correlations. The relations between c_{13} and the other elastic constants are not clear. The correlations among the Thomsen parameters are found to be fair to poor. The problem in Horne's statistical analysis is that it is not always beneficial to include indiscriminately as many data as possible. The true relationships may be covered by data of poor quality control. Yan et al. (2015) analyzed sensitivity of c_{13} to uncertainties in the oblique-velocity measurement, such as uncertainty in determination of the direction of the core plug or the TI symmetry axis, and underestimation of the phase velocities due to insufficient piezoelectric transducer size or over-long sample. Since there are significant uncertainties in the determination of c_{13} and δ in laboratory when the dimensions of the sample are known, it will be more challenging to acquire all the five independent elastic parameters from the logging data or seismic data. Therefore, finding the relation between c_{13} and other TI elastic constants is important for practical applications of seismic anisotropy in exploration geophysics.

Based on the laboratory-observed relationships between the principal Poisson's ratios of hydrocarbon-source rocks, whose elastic properties are approximated by transverse anisotropy, Yan et al. (2015) derived physical constraints on c_{13} by c_{11}, c_{33}, and c_{66}. The constraints can be utilized as a tool of quality control for laboratory velocity-anisotropy measurements, especially for the determination of c_{13} and the

Thomsen parameter δ. The primary goal of this study is to find the genuine relationships between c_{13} or δ with the other TI parameters for shales using the most reliable velocity-anisotropy measurement data.

3.3 Laboratory Velocity Anisotropy Measurement

The elastic properties of a TI medium are specified by five independent elastic constants. Using the Voigt notation, the elastic stiffness tensor of a TI medium is expressed by

$$\boldsymbol{C} = \begin{pmatrix} c_{11} & c_{11}-2c_{66} & c_{13} & 0 & 0 & 0 \\ c_{11}-2c_{66} & c_{11} & c_{13} & 0 & 0 & 0 \\ c_{13} & c_{13} & c_{33} & 0 & 0 & 0 \\ 0 & 0 & 0 & c_{44} & 0 & 0 \\ 0 & 0 & 0 & 0 & c_{44} & 0 \\ 0 & 0 & 0 & 0 & 0 & c_{66} \end{pmatrix}. \tag{3.1}$$

The five elastic constants defining a TI medium can be obtained from five velocity measurements:

$$c_{11} = \rho V_{\mathrm{P90}}^2, \tag{3.2}$$

$$c_{33} = \rho V_{\mathrm{P0}}^2, \tag{3.3}$$

$$c_{44} = \rho V_{\mathrm{SH0}}^2 = \rho V_{\mathrm{SV0}}^2 = \rho V_{\mathrm{SV90}}^2, \tag{3.4}$$

$$c_{66} = \rho V_{\mathrm{SH90}}^2, \tag{3.5}$$

$$c_{13} = \sqrt{(2\rho \mathrm{V}_{\mathrm{P}\theta 45}^2 - c_{11} - c_{44})(2\rho \mathrm{V}_{\mathrm{P}\theta 45}^2 - c_{33} - c_{44})} - c_{44}. \tag{3.6}$$

where the subscripts *P*, *SV* and *SH* denote the three wave modes in an anisotropic medium, respectively. The subscript θ denotes the phase velocity or phase angle. The angle is relative to the TI symmetry axis, so that $V_{P\theta 45}$ is the 45° P-wave phase velocity. The oblique velocity can be measured in an oblique direction other than 45°, in which case, c_{13} is computed by equation (2.21).

Determination of c_{11}, c_{33}, c_{44}, and c_{66} is straightforward from the traditional ultrasonic measurements. Determination of c_{13} from the oblique-velocity measurement is more complicated and requires careful quality control. Therefore, there are more uncertainties in the estimation of the Thomsen parameter δ than ε and γ. Figure 3.1 shows the crossplot between c_{13} and v_{HH}/v_{HV} ratio using data from dynamic velocity-anisotropy measurements. The data sources are from Thomsen (1986), Johnston and Christensen (1995), Vernik and Liu (1997), Jakobsen and Johansen (2000), Wang (2002b, shale and coal samples only), and Sone (2012, 2013). The data collected by Thomsen (1986) are from various sources, only data points with anisotropy stronger than the measurement uncertainty (ε>0.03 and γ>0.03) are included. Wang's data are corrected for mistaking group velocity for phase velocity in the oblique direction (Yan et al., 2015). If there is a pressure-dependent measurement, no more than three data points are used for the same sample to prevent the overweighting effect of this sample.

The crossplot is divided into three areas. In the left, several data points have negative v_{HH} values, which physically means that the horizontal plug under uniform axial compressional stress will shrink along the bedding direction. The corresponding c_{13} is above the high bound and it tends to have a higher value of δ. In the right area, there

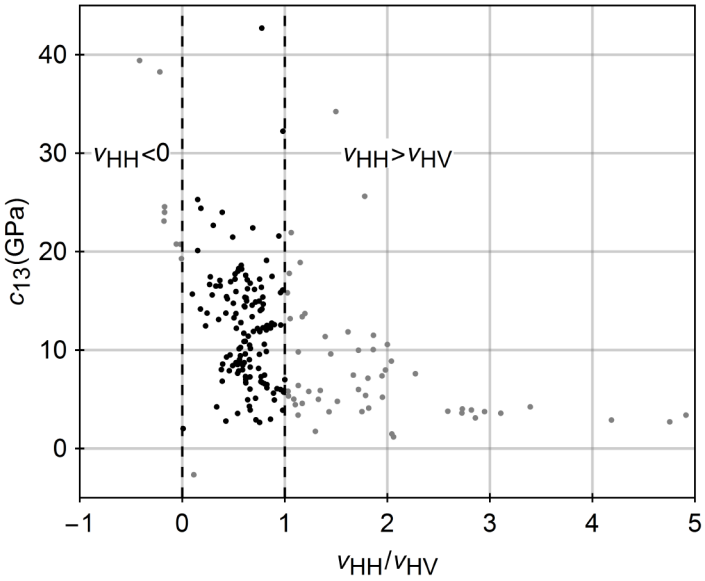

Figure 3.1 Uncertainty in the estimation of c_{13} from laboratory velocity-anisotropy measurements. Gray points are located outside of the physical bounds of c_{13}. Data sources: (1) Thomsen, 1986; (2) Johnston and Christensen, 1995; (3) Vernick and Liu, 1997; (4) Jakobsen and Johansen, 2000; (5) Wang, 2002b; and (6) Sone, 2012.

are quite a few points with $v_{HH} > v_{HV}$, which physically means that the horizontal plug under uniform axial compressional stress will expand more along the bedding than in the direction perpendicular to the bedding. The corresponding c_{13} value is lower than the low bound, and it tends to have a lower value of δ. The bounds of c_{13} for each data point may be different since the corresponding c_{11}, c_{33}, and c_{66} are different for each data point. About 2/3 of the data points lie in the center area, where it is believed that all hydrocarbon-source rocks that can be classified as an effective TI medium should lie within. Since there are more data points lying below the low bound than above the high bound, there might be a general tendency of underestimating of c_{13} and δ. Yan et

al. (2015) analyzed the reasons for c_{13} to be lying out of the bounds and the bias toward underestimation of c_{13} and δ. There is one data point having negative c_{13}, and it has negative v_V. This data point also has negative c_{11}-2c_{66} and a complex c_{13} upper bound. The data point originally comes from Lin (1985) and is collected in the dataset by Thomsen (1986). Very poor shear wave signals are reported in the measurement by Lin (1985). This exception may quite possibly be due to measurement errors.

3.4 Correlations among the TI Elastic Constants

When elastic anisotropic properties of shales are considered, at least five independent elastic parameters are involved, which leads to significant increase in the technical complexity compared to the isotropic case when only two elastic parameters are considered. Therefore, it is important to study the relations between the elastic parameters for simplification of the problem of seismic anisotropy. Using the same data sources as used in the last section, Figures 3.2 and 3.3 show the correlations between c_{11} and c_{66}, and c_{33} and c_{44}, respectively. Both of the correlations are strong, which means the P-wave and S-wave velocities have strong correlations both in the direction along the bedding and in the direction perpendicular to the bedding. The correlation along the bedding is stronger because the elastic properties are less sensitive to the stress effect due to soft inclusions of pore fluids or organic matter. The correlations are better than those shown by Horne (2013), because our data source includes less data coming from the wireline logging data or VSP data. The unfilled data points have c_{13} out of the physical constraints as described by equation (2.13). Since the non-oblique elastic constants should not be affected by the oblique-velocity measurement for the

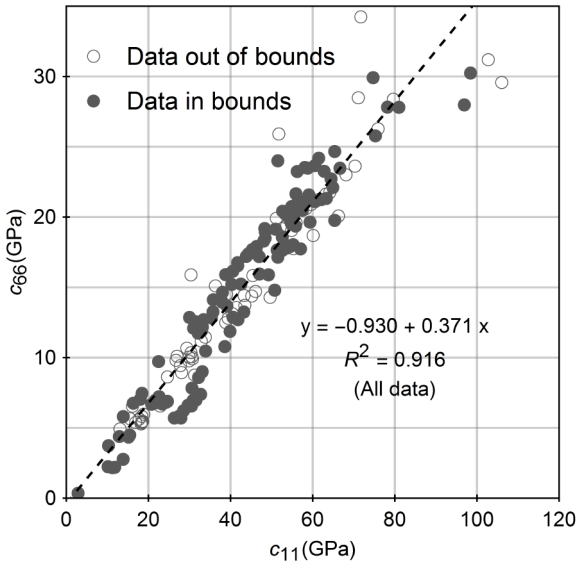

Figure 3.2 Correlation between c_{11} and c_{66}. Same data sources as Figure 3.1 are used.

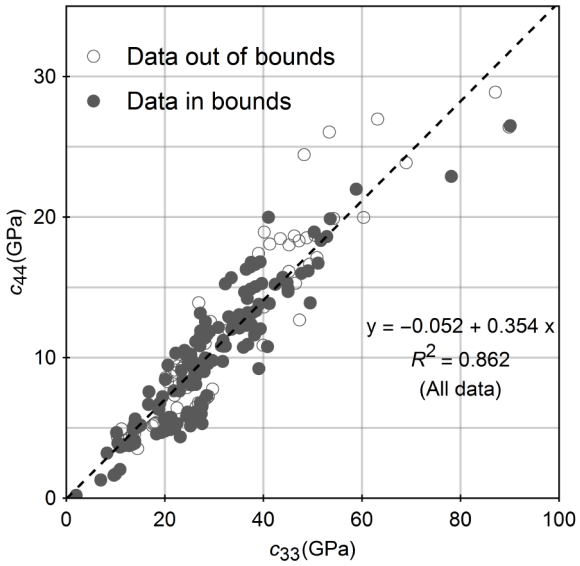

Figure 3.3 Correlation between c_{33} and c_{44}. Same data sources as Figure 3.1 are used.

determination of c_{13}, the filled and unfilled data points should have the same trend of correlation.

Horne (2013) shows that the correlations between c_{13} and the other individual TI elastic constants are from fair to poor. When TI anisotropy reduces to isotropy, c_{11} equals c_{33}, c_{66} equals c_{44}, and c_{13} equals c_{33}-2c_{44}. Therefore, it is natural to expect there may be some connection between c_{13} and c_{33}-2c_{44}, or c_{13} and c_{11}-2c_{66}. Figure 3.4 shows the strong correlations between c_{13} and c_{33} -2c_{44} and between c_{13} and c_{11} -2 c_{66}. If c_{33}-2c_{44} is used to approximate c_{13}, it will be generally underestimated significantly. If c_{11}-2c_{66} is used to approximate c_{13}, it will be generally overestimated slightly. Considering there may be a bias toward underestimation c_{13} in laboratory velocity-anisotropy measurements (Yan et al., 2015), c_{11} -2c_{66} is a much better approximation of c_{13} than c_{33}-2c_{44}. It is also observed that the data points lying outside of the bounds in Figure 3.1 mostly lie further away from the correlation trend, which manifests the rationality of the physical constraints of c_{13} by equation (2.13) from another point of view.

3.5 Approximation of TI Anisotropy

The approximation of c_{13} by c_{33}-2c_{44} is used by the ANNIE anisotropy model (Schoenberg et al., 1996). The ANNIE model is a three-parameter TI model. The elastic tensor can be written in the form of

$$\boldsymbol{C} = \begin{pmatrix} c_{33}+2(c_{66}-c_{44}) & c_{33}-2c_{44} & c_{33}-2c_{44} & 0 & 0 & 0 \\ c_{33}-2c_{44} & c_{33}+2(c_{66}-c_{44}) & c_{33}-2c_{44} & 0 & 0 & 0 \\ c_{33}-2c_{44} & c_{33}-2c_{44} & c_{33} & 0 & 0 & 0 \\ 0 & 0 & 0 & c_{44} & 0 & 0 \\ 0 & 0 & 0 & 0 & c_{44} & 0 \\ 0 & 0 & 0 & 0 & 0 & c_{66} \end{pmatrix}. \tag{3.7}$$

It can be seen that the ANNIE model uses c_{33}-2c_{44} to approximate c_{11}- 2c_{66} and c_{33}+2(c_{66}-c_{44}) to approximate c_{11}. We have shown that c_{33}-2c_{44} is generally not a good approximation of c_{13} for shales, the reader can find the other two approximations are quite gross.

When c_{11} -2 c_{66} is used to approximate c_{13}, the number of independent elastic constants for a TI medium is reduced to four from five, and the elastic stiffness matrix can be expressed by

$$\boldsymbol{C} = \begin{pmatrix} c_{11} & c_{12} & c_{12} & 0 & 0 & 0 \\ c_{12} & c_{11} & c_{12} & 0 & 0 & 0 \\ c_{12} & c_{12} & c_{33} & 0 & 0 & 0 \\ 0 & 0 & 0 & c_{44} & 0 & 0 \\ 0 & 0 & 0 & 0 & c_{44} & 0 \\ 0 & 0 & 0 & 0 & 0 & c_{66} \end{pmatrix}. \tag{3.8}$$

where $c_{12} = c_{11}$-2c_{66}. Because four independent elastic constants are used to define the elastic tensor, we temporarily call this approximation quartic TI anisotropy. Obviously, for most shales, the quartic TI anisotropy is a more proper approximation of transverse isotropy than the ANNIE model. The disadvantage of the quartic TI anisotropy is that one more parameter (c_{11}) is involved than the ANNIE model. However, the information

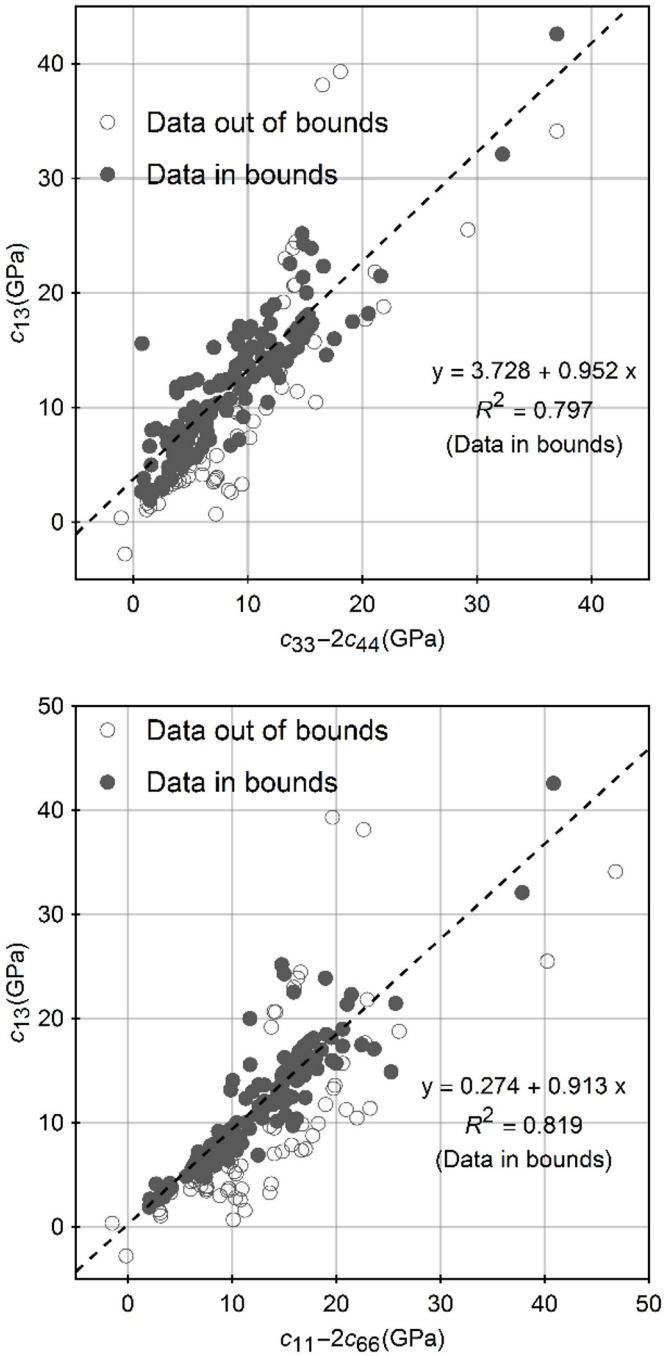

Figure 3.4 The correlation between c_{13} and c_{33}-2c_{44} (top) and the correlation between c_{13} and c_{11}-2c_{66} (bottom). Data sources are same as Figure 3.1.

of c_{11} can be obtained easier than c_{66}. The quartic TI approximation should be more useful for practical applications.

A more desirable approximation of TI anisotropy is the elliptic anisotropy brought up by Helbig (1983). For elliptic anisotropy, the Thomsen parameter ε equals δ, which means the P-wave normal-moveout velocity equals the horizontal velocity (Alkhalifah and Tsvankin, 1995; Tsvankin, 2012). This simplification will significantly simplify anisotropic-seismic-data processing. From equations (2.15) and (2.17), for elliptic anisotropy, c_{13} is equivalently approximated by

$$c_{13} = \sqrt{(c_{11} - c_{44})(c_{33} - c_{44})} - c_{44}. \tag{3.9}$$

Figure 3.5 shows the correlation between c_{13} and its elliptic approximation using all the data points within the bounds as shown in Figure 3.1. In Figure 3.5, the elliptic approximation generally overestimates c_{13}. For most shales, elliptic anisotropy is not a good approximation of the elastic properties. From the left panel in Figure 3.4, the approximation of c_{13} by c_{11} -2 c_{66} is generally acceptable, but the c_{13} values are slightly underestimated in general.

Since the c_{13} bounds by equation (2.13) contain terms of c_{11} -2 c_{66} and c_{33}, we could test the relation between c_{13} and its bounds. Figure 3.6 shows the correlation between c_{13} and its bounds using all the data points lying within the bounds. The correlation is between c_{13} and a combination of c_{11}, c_{33}, and c_{66}. It can be seen that the estimation of c_{13} is further improved since an additional parameter c_{33} is involved. The modified ANNIE (MANNIE) model by Suarez-Rivera et al. (2009) is used to find the relation

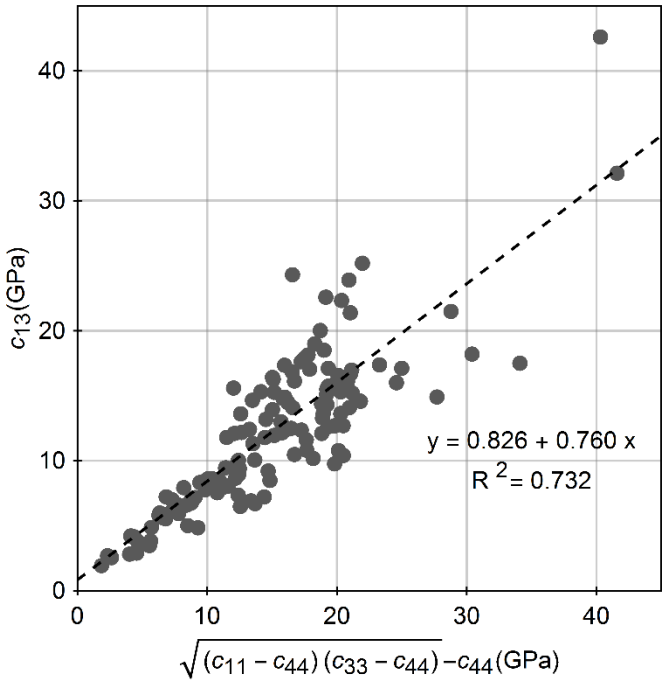

Figure 3.5 Correlation between c_{13} and its elliptic approximation using data points in the bounds.

between c_{13} and c_{11}-2c_{66} and c_{33}-2c_{44} by introducing two extra coefficients. It may be more straightforward to find the correlation between c_{13} and c_{11}, c_{33}, c_{44}, and c_{66} directly using multi-variable regression. There is no obvious improvement in approximation of c_{13} by involving all other TI elastic constants, so we temporarily stick to the approximation of c_{13} by its bounds. Next, we will try to find a better approximation of c_{13} using the data sources with better quality control.

3.6 Quality Control Evaluation of the Data Sources

In Figure 3.1, we have shown that there are significant uncertainties in the estimation of c_{13} from laboratory velocity-anisotropy measurements. These

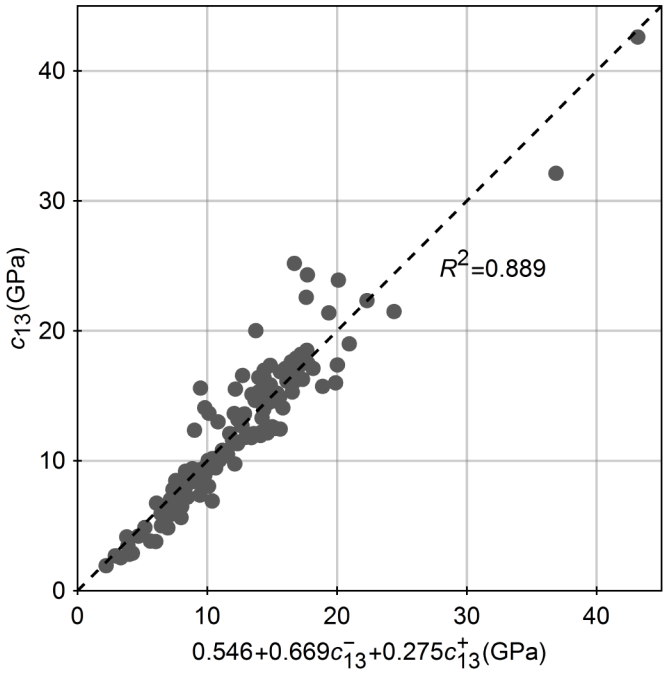

Figure 3.6 Correlation between c_{13} and its physical constraints approximation using data points in the bounds.

measurements are conducted by different people using different setups and the data quality control is different. Figure 3.7 shows evaluation of the quality control of the individual dataset using the constraints on c_{13}. Thomsen (1986) collected the data from various sources, the measurements were conducted before discussion of the phase and group velocity confusion in the oblique-velocity measurement by Dellinger and Vernik (1994). Some of the data come from the logging data. It is not a surprise the data quality control of dataset 1 is not very good. For dataset 2 and dataset 3, the measurements are both conducted on 1-inch core samples. Dataset 2 uses P-wave piezoelectric transducers with a diameter of 25.4 mm and Dataset 3 uses P-wave piezoelectric transducer with a diameter of 12 mm. The former

generally uses shorter core samples than the later. The former is based on 11 core plugs for one data point and the latter is based on 3 core plugs for one data point. These differences explain why dataset 2 has a better data quality control than dataset 3. Most of the data points in dataset 4 lie outside of the constraints. The measurement by Jakobsen and Johansen (1995) is based on a single vertical core plug with a diameter of 38 mm. In the oblique-velocity measurement, the diameters of the transmission and receiving transducers are 5 mm. They cannot be treated as a point source and a point receiver in the cross section passing the TI symmetrical axis, so there is difficulty in measuring the real group velocity, and the actual group angle is hard to determine. This explains why most of the data points in dataset 4 lie outside of the bounds. Wang's measurement setup (2002a) is based on a single horizontal plug and single oblique-velocity measurement. In Wang's data (2002b), the measured oblique velocity is directly used as phase velocity to calculate c_{13} and δ. If the contact between the sample and the buffer can be approximated as a point contact in the cross section, the oblique velocity measured should be group velocity. Under this assumption, corrections are made on Wang's data. There are still roughly one third of the data points lying outside of the bounds.

Two datasets have all the data points lying within the bounds: Dataset 2 by Johnston and Christensen (1995) and dataset 6 by Sone (2012). They have a common feature: Multiple oblique velocities are measured to estimate c_{13} by least square regression. Each data point in dataset 2 is based on measurements of 11 core plugs in different directions. Each data point in dataset 6 is based on measurements of 5 core plugs in

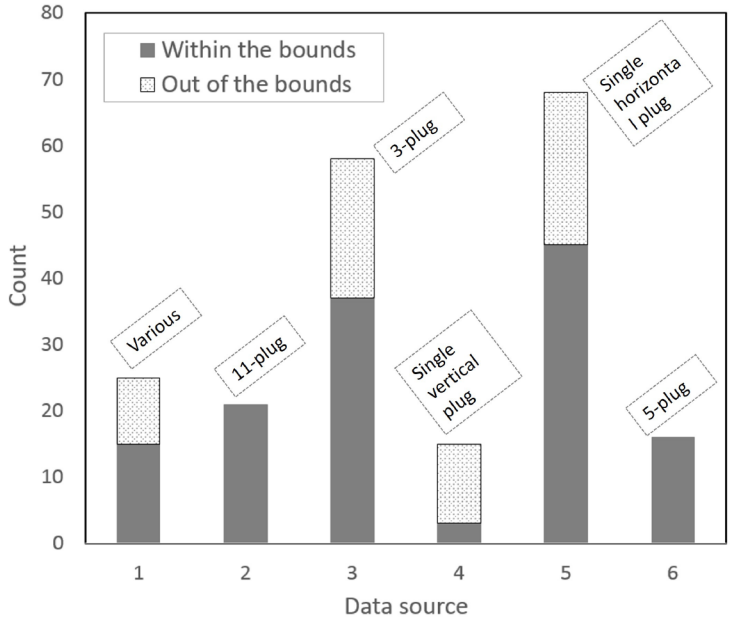

Figure 3.7 Evaluation of dataset quality control using the c_{13} bounds: 1. Thomsen, 1986; 2. Johnston and Christensen, 1995; 3. Vernik and Liu, 1997; 4. Jakobsen and Johansen, 2000; 5. Wang, 2002b; 6. Sone, 2012.

different directions (0°, 30°, 45°, 60°, 90°). From the above analysis, multiple oblique- velocity measurements are critical for reduction of the uncertainties in the estimation of c_{13}. Datasets 2 and 6 have better quality control than the other datasets in the determination of c_{13} and δ.

3.7 Correlation Using Datasets of Good Quality Control

As shown in Figure 3.7, if a dataset has many data points with c_{13} values lying out of the bounds, the data points with c_{13} values lying in the bounds may all also have significant uncertainties in the estimation of c_{13}. If we use only data points coming from the datasets with good quality control, the correlation should be further

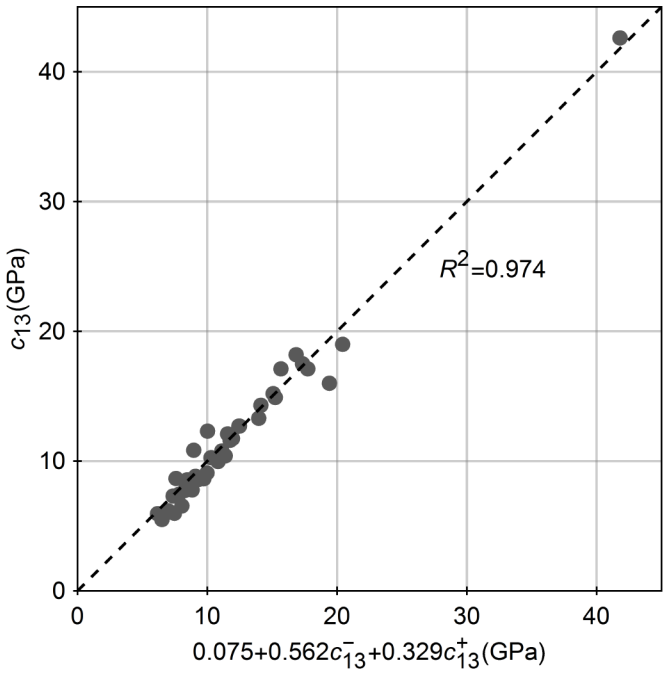

Figure 3.8 Correlation between c_{13} and its bounds using datasets 2 and 6.

improved if a strong correlation really exists between c_{13} and other TI elastic constants.

In the following analysis, we use only datasets 2 and 6. Figure 3.8 shows the correlation between c_{13} and its bounds using the data points from datasets 2 and 6. Compared to Figure 3.6, the correlation is significantly improved. This means that for hydrocarbon-source rocks, c_{13} is not "independent" and it is generally dependent on c_{11}, c_{33}, and c_{66}. Since c_{13} is usually more difficult to be obtained than c_{11}, c_{33}, and c_{66}, this correlation may be quite useful in practical applications:

$$c_{13} = 0.075 + 0.562\, c_{13}^{-} + 0.329\, c_{13}^{+}\,, \tag{3.10}$$

where the bounds are expressed by equation (2.22) and are a function of c_{11}, c_{33}, and c_{66}.

Although the data points in Datasets 2 and 6 are significantly reduced compared to the entire data sources used in this study, the organic shale samples in datasets 2 and 6 come from eight different areas and formations. This correlation is still representative in a certain degree. It would be desirable that more laboratory anisotropy measurements of high quality control could be made in the future.

Using the datasets of relatively high quality control, we again compare the approximation of c_{13} by the quartic TI anisotropy and elliptic anisotropy. As shown in Figure 3.9, for most of the data points the elliptic anisotropy significantly overestimates c_{13}, whereas the quartic TI anisotropy only slightly overestimate c_{13}. Compared to the quartic TI anisotropy, the elliptic anisotropy is usually a poor approximation of TI anisotropy for shales.

3.8 Application of the Correlation

From equations (2) to (6), only four TI elastic constants (c_{11}, c_{33}, c_{66}, and c_{13}) are needed to define the Young's moduli and Poisson's ratios for a TI medium. In practice, c_{13} is usually more difficult to be acquired than c_{11}, c_{33}, and c_{66}. If c_{11}, c_{33}, and c_{66} are available, for example, from the acoustic logging data, we can predict c_{13} using the empirical relation by equation (21), and then the Young's moduli and Poisson's ratios can be estimated.

In Figures 3.10 and 3.11, using datasets 2 and 6, the measured c_{11}, c_{33}, and c_{66} are

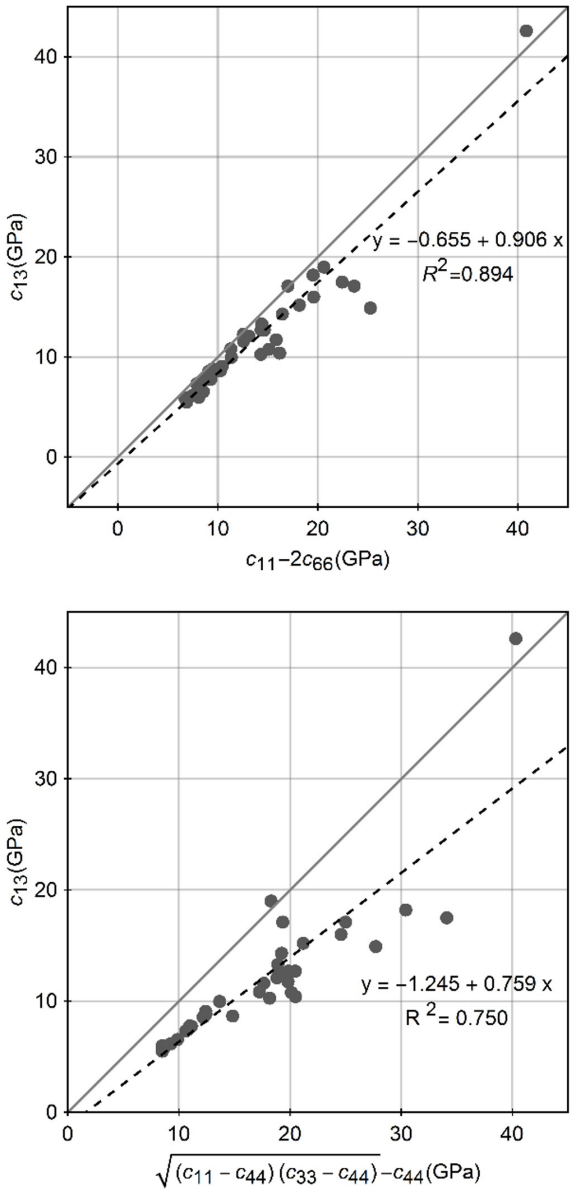

Figure 3.9 Comparison of approximations of c_{13} by c_{12} and the elliptic anisotropy assumption using datasets 2 and 6.

first used to predict c_{13} using equation (21). Then Young's moduli and Poisson's ratios are calculated using the predicted c_{13} and measured c_{11}, c_{33}, and c_{66}. Figure

3.10 shows the correlations between the predicted and measured Young's moduli. It can be seen that the Young's moduli can almost be perfectly predicted by the estimated c_{13}. Figure 3.11 shows a good correlation between predicted and measured Poisson's ratios. Comparing Figures 3.10 and 3.11, the degree of correlation between the predicted value and measured value indicates that the Poisson ratios are more sensitive to c_{13} than the Young's moduli. This partly explains why the relationship between the Poisson's ratios can be used to derive the physical constraints on c_{13}.

To develop the unconventional hydrocarbon resources the shales need to first be fractured. Effective fracturing of shales needs information of the in-situ stress. Higgins et al. (2008) introduces formulas to predict the in-situ stress in a TI medium:

$$\sigma_h - \alpha\sigma_{pp} = \frac{E_H}{E_V}\frac{\nu_V}{1-\nu_{HH}}\left(\sigma_v - \alpha(1-\xi)\sigma_{pp}\right) + \frac{E_H}{1-{\nu_{HH}}^2}\epsilon_h + \frac{E_H\nu_{HH}}{1-{\nu_{HH}}^2}\epsilon_H, \tag{3.11}$$

$$\sigma_H - \alpha\sigma_{pp} = \frac{E_H}{E_V}\frac{\nu_V}{1-\nu_{HH}}\left(\sigma_v - \alpha(1-\xi)\sigma_{pp}\right) + \frac{E_H}{1-{\nu_{HH}}^2}\epsilon_H + \frac{E_H\nu_{HH}}{1-{\nu_{HH}}^2}\epsilon_h, \tag{3.12}$$

where σ_h and σ_H are the minimum and maximum horizontal stresses, respectively. σ_{pp} refers to pore pressure, α is the Biot's constant, ξ is an anisotropy coefficient (0 for TI anisotropy), and ϵ_h and ϵ_H are the minimum and maximum horizontal strains, respectively. The formulation requires inputs of the Young's moduli and Poisson's

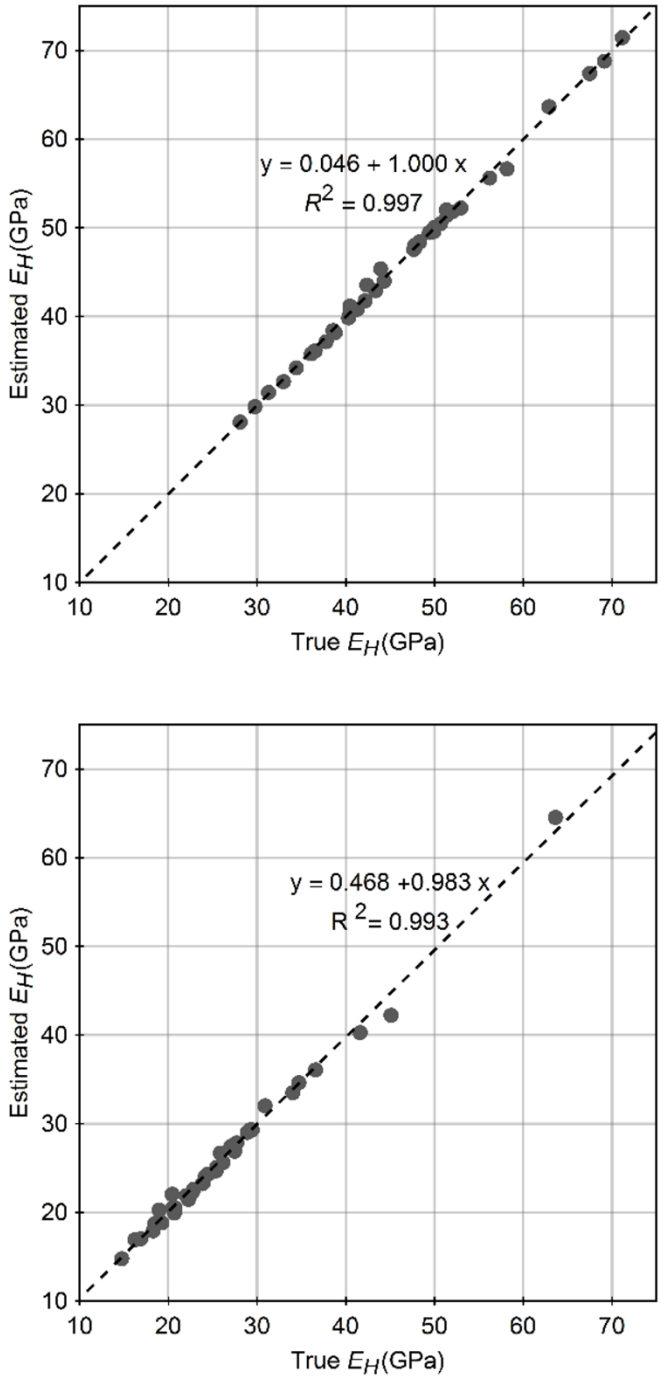

Figure 3.10 Prediction of the vertical Young's modulus (above) and the horizontal Young's modulus (below) using the correlation between c_{13} and its bounds as shown in Figure 3.8.

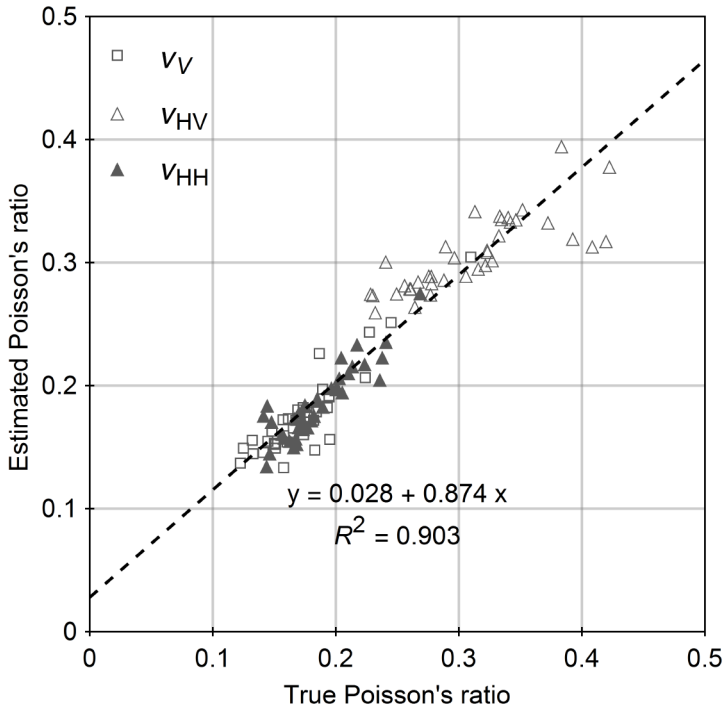

Figure 3.11 Prediction of Poisson's ratios using the correlation between c_{13} and its bounds as shown in Figure 3.7.

ratios of the TI medium. They suggest these information be acquired from the acoustic logging data. Since c_{13} is usually difficult to be acquired from the acoustic logging data, we can use the empirical correlation (equation (3.10)) to predict the Young's moduli and Poisson's ratio if information about c_{11}, c_{33}, and c_{66} are available. The correlation between c_{13} and its bounds may be very useful for the in-situ stress prediction.

3.9 Prediction of δ

The Thomsen parameters, instead of the TI elastic constants, are more convenient and commonly used for seismic-data processing and interpretation. Reliable estimation of the anisotropy parameters is the foundation for anisotropic-seismic-data processing and interpretation. If a good relationship between δ and the other anisotropy parameters can be found, we may mathematically simplify the problem or use the correlation as a constraint for anisotropic parameter estimation.

The correlation between δ and the other Thomsen parameter parameters can be obtained by substituting equation (3.10) into the definition of δ (equation (2.15)), but the expression will be complicated. Instead, we directly correlate δ with ε, γ, and the ratio of β_0^2/α_0^2 using datasets 2 and 6. Here the term β_0^2/α_0^2 is used because it equals the ratio of c_{44}/c_{33}. ε and γ are also in the form of the ratio of the TI elastic constants. The result is shown in Figure 3.12. Considering the difficulty in estimating δ from the laboratory measurements, the result is quite satisfactory. Yan et al. (2015) shows the correlation of c_{13} with the other Thomsen parameters using all the data points with c_{13} lying within the bounds, and the correlation coefficient is 0.54. As shown in Figure 3.13, if all the data points in all the datasets are used, we will have little confidence that δ can be predicted from the other Thomsen parameters. The steady improvement of the correlations when laboratory measurements data of better quality control are used shows the validity of the physical constraints of c_{13} as a tool of quality control for laboratory velocity-anisotropy measurements.

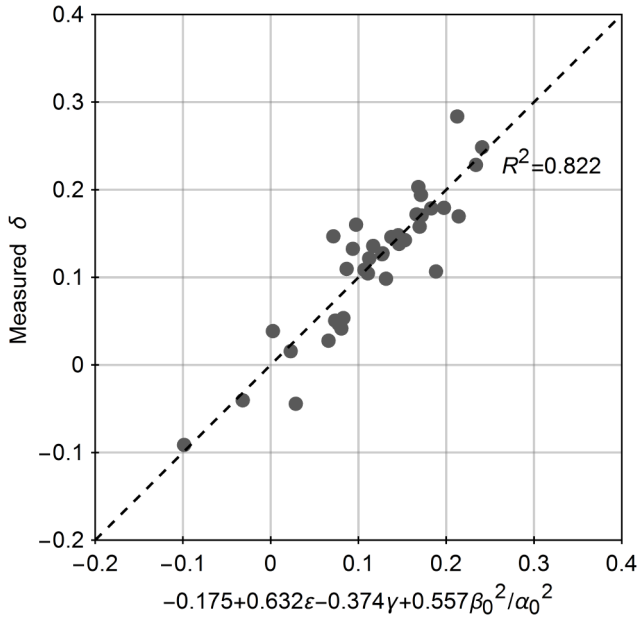

Figure 3.12 Prediction of δ from ε, γ and the ratio of vertical S-wave velocity to vertical P-wave velocity using datasets 2 and 6.

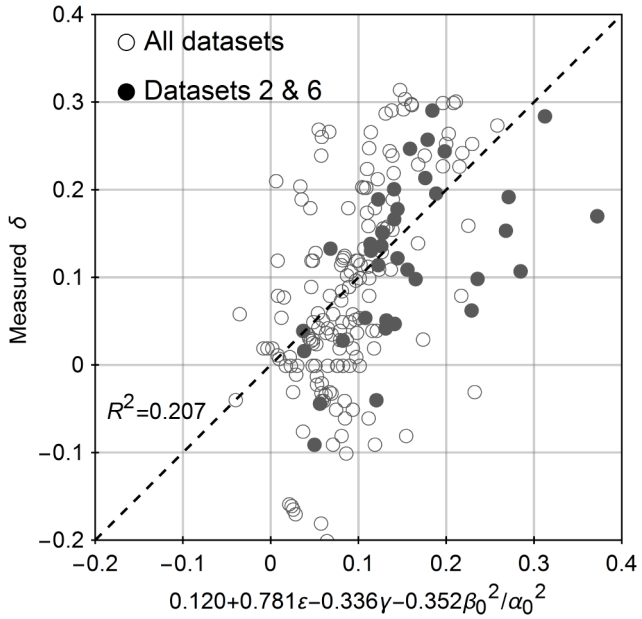

Figure 3.13 Prediction of δ from ε, γ and the ratio of vertical S-wave velocity to vertical P-wave velocity using all the datasets used in Figure 3.1.

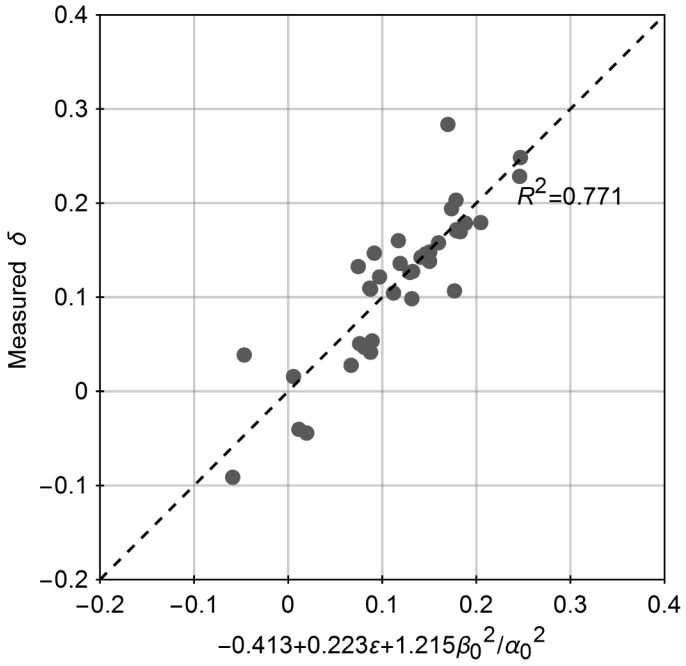

Figure 3.14 Prediction of δ from ε and the ratio of vertical S-wave velocity to vertical P-wave velocity using datasets 2 and 6.

In practical applications, the shear wave anisotropy information is usually not available from seismic data, and it may be more useful to find the correlation between δ and a combination of ε and the ratio of β_0^2/α_0^2. As shown in Figure 3.14, the correlation is acceptable without γ:

$$\delta = -0.413 + 0.223\varepsilon + 1.215\,\frac{\beta_0^2}{\alpha_0^2}\,. \tag{3.13}$$

When the anisotropy reduces to isotropy (δ=0 and ε=0), the ratio of the vertical P-wave velocity to S-wave velocity (α_0/β_0) is 1.715 from the above empirical formula. It is a reasonable value for some sedimentary rocks (Castagna et al. 1985).

3.10 Conclusion

In laboratory velocity-anisotropy measurements, there are significant uncertainties in the determination of c_{13} and δ. The physical constraints on c_{13} can be used to evaluate the data quality of the velocity-anisotropy measurements. Using the data sources with good quality control, it is found that a strong correlation exits between c_{13} and other TI elastic constants. Also a strong correlation exists between δ and the other Thomsen parameters. These correlations may have important applications in geomechanics and exploration geophysics when effect of anisotropy cannot be ignored. For hydrocarbon-source rocks, the approximations of TI anisotropy by ANNIE and elliptic anisotropy are usually less accurate than the approximation by the quartic TI anisotropy.

3.11 Acknowledgements

This study is sponsored by the Fluids and DHI consortium of the Colorado School of Mines and the University of Houston.

3.12 References

Alkhalifah T. and Tsvankin I. 1995. Velocity analysis for transversely isotropic media. *Geophysics* **60**, 1550-1566.

Blum T.E., Adam L. and van Wijk K. 2013. Noncontacting benchtop measurements of the elastic properties of shales. *Geophysics* **78**, C25-C31.

Castagna J.P., Batzle M.L. and Eastwood R.L. 1985. Relationships between compressional-wave and shear-wave velocities in clastic silicate rocks. *Geophysics* **50**, 571-581.

Dellinger J.A. and Vernik L. 1994. Do traveltimes in pulse-transmission experiments yield anisotropic group or phase velocities? *Geophysics* **59**, 1774- 1779.

Helbig K. 1983. Elliptic anisotropy – Its significance and meaning. *Geophysics* **48**, 825-832.

Higgins, S., Goodwin S., Donald A., Bratton T. and Gracy G. 2008. Anisotropic stress models improve completion design in the Baxter shale. *SPE Annual Technical Conference and Exhibition*, SPE 115736.

Horne S.A. 2013. A statistical review of mudstone elastic anisotropy. *Geophysical Prospecting* **61**, 817-826.

Jakobsen M. and Johansen T.A. 2000. Anisotropic approximations for mudstones: A seismic laboratory study. *Geophysics* **65**, 1711-1725.

Johnston J.E., and Christensen N.I. 1995. Seismic anisotropy of shales. *Journal of Geophysical Research* **100**, 5591-6003.

Lin W. 1985. Ultrasonic velocities and dynamic elastic moduli of Mesaverde rock. Lawrence Livermore National Laboratory. Rep. 20273, rev. 1.

King M.S. 1964. *Wave Velocities and Dynamic Elastic Moduli of Sedimentary Rocks*. Ph.D. thesis, University of California, Berkeley.

Schoenberg M., Muir F. and Sayers C. 1996. Introduction ANNIE: A simple three-parameter anisotropy velocity model for shales. *Journal of Seismic Exploration* **5**, 35-49

Sondergeld C.H., Rai C.S., Margesson R.W. and Whidden K.J. 2000. Ultra- sonic measurement of anisotropy on the Kimmeridge Shale. *SEG Expanded Abstracts*.

Sondergeld C.H. and Chandra S.R. 2011. Elastic anisotropy of shales. *The Leading Edge* **30**, 325-331.

Sone H. 2012. *Mechanical Properties of Shale Gas Reservoir Rocks and Its Relation to In-situ Stress Variation Observed in Shale Gas Reservoirs*. Ph.D. thesis, Stanford University.

Suarez-Rivera R. and Bratton T. 2009. Estimating Horizontal Stress from Three-Dimensional Anisotropy. US Patent application number 20090210160.

Thomsen L. 1986. Weak elastic anisotropy. *Geophysics* **51**, 1954-1966.

Thomsen L. 1990. Poisson was not a geophysicist, *Geophysics: The Leading Edge of Exploration*, December 1990.

Tsvankin I. 2012. *Seismic Signatures and Analysis of Reflection Data in Anisotropic Media*: 3rd edition, SEG.

Vernik L. and Nur A. 1992. Ultrasonic velocity and anisotropy of hydrocarbon source rocks. *Geophysics* **57**, 727-735.

Vernik L. and Liu X. 1997. Velocity anisotropy in shales: A petrophysical study. *Geophysics* **62**, 521-532.

Wang Z. 2002a. Seismic anisotropy in sedimentary rocks, part 1: A single-plug laboratory method. *Geophysics* **67**, 1415-1422.

Wang Z. 2002b. Seismic anisotropy in sedimentary rocks, part 2: Laboratory data: *Geophysics* **67**, 1423-1430.

Yan F., Han D.-h. and Yao Q. 2012. Oil shale anisotropy measurement and sensitivity analysis. *SEG Expanded Abstracts*.

Yan F., Han D.-h. and Yao Q. 2014. Benchtop rotational group-velocity measurement on shales. *SEG Expanded Abstracts*.

Yan F., Han D.-h. and Yao Q. 2015. Physical constraints on c_{13} and δ for transversely isotropic hydrocarbon source rocks. *Geophysical Prospecting*, doi: 10.1111/1365-2478.12265

Chapter 4

A Practical and Robust Method for Laboratory Determination of c_{13} and δ

4.1 Abstract

There exist significant uncertainties in the laboratory determination of c_{13} and δ. These uncertainties are primarily related to the velocity measurement in the oblique direction. An analysis of the measurement results from the literature found that these uncertainties could be greatly reduced if redundant oblique velocities are made. For the industrial applications, it is impractical to make multiple oblique velocities on multiple core plugs. The design of making multiple oblique group velocities on a single vertical core plug is seriously flawed. However, it is applicable to make multiple genuine oblique group-velocity measurements on a single horizontal core plug. The measurement results show that shales can be classified as a typical transversely isotropic medium. There is a coupling relation between c_{44} and c_{13} in determining the directional dependence of seismic velocities of shales. The quasi-P wave or quasi-S wave velocities can be approximated by three elastic parameters.

4.2 Introduction

Mudstones or shales make up about 75 percent of the sedimentary rocks in volume and are becoming important reservoir rocks for hydrocarbon resources. Shales are usually anisotropic in elastic properties. The anisotropic properties may have a significant effect on seismic imaging and seismic amplitude interpretation. Therefore, study of the physical properties of shales is very important for seismic exploration. Laboratory velocity-anisotropy measurements on shales are done routinely. Shales are often treated as transversely isotropic (TI) media. In addition to the five independent TI elastic constants, the measurement results are also reported in terms of Thomsen parameters (Vernik and Nur, 1992; Johnston, 1995; Vernik and Liu, 1997; Jakobsen and Johansen, 2000; Sondergeld et al., 2000; Wang, 2002; Sondergeld and Rai, 2011 and Sone, 2012). Of the three Thomsen parameters (ε, γ, and δ), δ is the most important parameter for exploration geophysicists since it describes the relation between the normal-moveout velocity and the vertical velocity (Thomsen, 1986 and Tsvankin, 2012). Thomsen (1986) pointed out that δ is an "awkward" combination of elastic parameters and its physical meaning is not straightforward. In spite of a large amount of laboratory measurements, our understanding of the parameter δ is not clear (Banik, 1987; Sayers, 2004). The laboratory measurement results show that δ has a poor correlation with the other Thomsen parameters, and even the rational data range of δ is not certain. For the five independent elastic constants (c_{11}, c_{33}, c_{44}, c_{66}, and c_{13}) of a TI medium, although theoretically, they are free independent variables, good to excellent mutual correlations exist between c_{11} and c_{66}, and between c_{33} and c_{44} from laboratory

velocity-anisotropy measurements. Nevertheless, the behavior of c_{13} is erratic and its relationships with the other elastic constants is not clear.

Yan et al. (2012, 2015) pointed out that our ambiguous understanding of c_{13} and δ may be caused by significant uncertainties in the laboratory velocity-anisotropy measurements, especially the velocity measurement in the oblique direction. Based on observation of the static mechanic measurement and physical intuition, Yan et al. (2015) argued that for hydrocarbon-source rocks, there exist certain relationships among the three principal Poisson's ratios of a TI medium. From these relations they derived tight constraints on c_{13} (equation (2.13)). It concludes that c_{13} is constrained by the other elastic constants that determine the elastic properties in the non-oblique directions and can be unambiguously determined by regular acoustic measurements. Based on the relationship between the estimated c_{13} with its constraints, Figure 3.7 shows the data quality evaluation of several velocity-anisotropy measurement datasets available from the literature. It is found that there are quite a few data points with c_{13} outside of its bounds.

It is observed that data sources 2 and 6 have all data points lying within the bounds. Compared to other data sources, data sources 2 and 6 have a common feature that c_{13} is estimated by least square regression of multiple oblique- velocity measurements. For data source 2, the measurements are based on 5 plugs of different directions for each data point. For data source 6, the measurements are based on 11 plugs of different directions. Yan et al. (2015) pointed out that c_{13} and δ are very sensitive to various errors associated with the oblique-velocity

measurement. Multiple oblique-velocity measurements in different directions are critical for reliable determination of c_{13} and δ.

In practice, preparation of multiple core samples with accurate direction control from the same depth interval is a very time-consuming and consequently expensive process. In actual velocity measurement, most of the time is spent preparing the sample, putting the sample in, and taking the sample out from the pressure vessel. These processes are the most error-prone. Therefore, it is more reliable if velocity-anisotropy measurements can be conducted on a single core plug. Blum et al. (2012; 2013) used laser technology to measure the elastic anisotropy based on a single horizontal core plug. In their measurement, no stress is applied to the horizontal core sample. The sample can be rotated freely for group-velocity measurements at different angles. Although this technique is innovative, the first arrival signal is not clear and it is very challenging to build it into a pressure vessel. The measurements lack consistency and the estimated δ for the two samples under study are quite unusual (-0.27 for one shale sample and 6.62 for the other). Sarout et al. (2015) tried to perform multiple oblique "group" velocity measurements on a vertical shale sample (the bedding direction is perpendicular to the axial direction of the cylindrical sample). The principle of group-velocity measurement is that the signal is emitted from a "point" source and received by a "point" receiver. Sarout et al. (2015) applied piezoelectric transducers of 5 mm diameter on a vertical core sample with a diameter of 38 mm. This is analogous to explore a target at 250 m depth using seismic sources and geophones of 50 m width in seismic data acquisition.

Obviously, it is improper to assume that group velocities are measured in these scenarios. Jakobsen and Johansen (2000) also claimed the oblique-velocity made on a single vertical sample is group velocity and this may explain why the their dataset has most of the data points lying outside of the c_{13} constraints， as shown in Figure 3.7. The configuration by Sarout et al. (2015) is deficient for genuine group-velocity measurements and the reliability of the estimated δ by inversion is in question.

In spite of a large amount of efforts made on velocity-anisotropy measurements of shales, the estimation of the critical anisotropic parameter δ still needs significant improvement. The primary goal of this study is to demonstrate that reliable and efficient estimation of c_{13} and δ can be made on a single horizontal core plug.

4.3 Group Velocity and Phase Velocity Measurement

In an anisotropic medium, there exist differences in both the magnitude and the direction between the group velocity and the phase velocity. The group velocity, also called ray velocity, is the speed by which the energy travels. The phase velocity is the instantaneous wave travel speed directly related to the particle motion. It is always normal to the wavefront. The coupling relations between the group velocity and phase velocity and the group angle and phase angle are given by (Byun, 1984; Yan et al., 2015):

$$\mathrm{Tan}(\varphi - \theta) = \frac{1}{V_\theta}\frac{\mathrm{dV}_\theta}{\mathrm{d}\theta}, \tag{4.1}$$

$$V_{P\theta} = V_{P\varphi} \cos(\varphi - \theta). \tag{4.2}$$

Here the velocity can be for either of the three wave modes. Using laboratory-measured parameters of a shale sample by Vernik and Liu (1997), Figure 4.1 illustrates the coupling relation between the group velocity and phase velocity, the group angle and phase angle. It can be seen that the relative difference between the group angle and phase angle may be greater than the scalar difference between the group velocity and phase velocity. Deviation of the group velocity from the phase velocity is controlled by the anisotropic properties and the direction of wave propagation. The deviation patterns are different for the quasi-P wave and SV wave. The direction difference can be over 20° for some strongly anisotropic shales. Obviously, confusion of the group-phase concepts may introduce significant error in velocity-anisotropy measurements.

The five elastic constants defining a TI medium can be obtained from five velocity measurements. The estimations of c_{11}, c_{33}, c_{44}, and c_{66} are straightforward. They can be determined from the traditional ultrasonic-velocity measurements in the non-oblique directions and usually there should be no extra uncertainty introduced. For a TI medium, the group velocity is identical to the phase velocity in the non-oblique directions. After c_{11}, c_{33}, and c_{44} are determined, a velocity must be measured in an oblique direction to estimate c_{13}. The oblique P-wave instead of SV wave is usually utilized to estimate c_{13} because there may be converted P-wave signals before the SV wave signal. Possible triplication around 45° will make the first-break-time picking of the SV wave signal more difficult. The oblique P wave velocity is usually

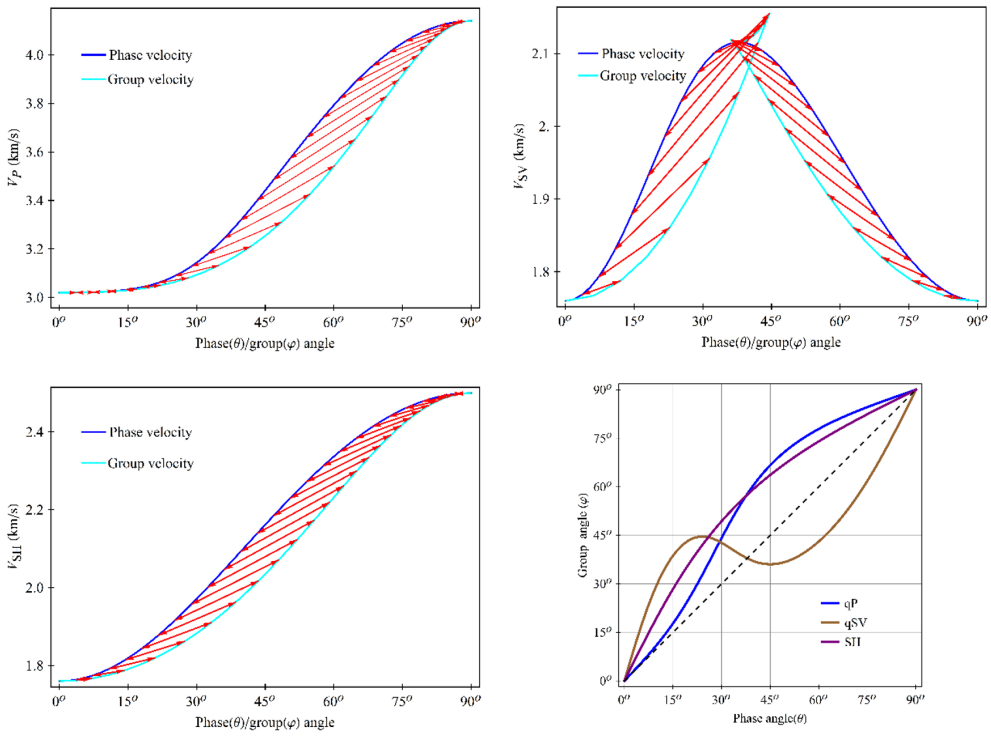

Figure 4.1 Coupling relations between the phase velocity and group velocity, the phase angle and group angle. The double arrow connects phase velocity at a certain phase angle and its corresponding group velocity in a certain group angle. The plot is based on Bakken shale sample at 8364 ft (Vernik, 1997), using parameters: c_{11}=35.31 GPa, c_{33}=18.79 GPa, c_{44}=6.38 GPa, c_{66}=12.87 GPa, c_{13}=6.58 GPa, ρ=2.06 g/cc.

made on a 45° plug (Vernik and Nur, 1992). It can be seen from equation (2.23) that c_{13} is most sensitive to the measurement error of this oblique velocity. The phase angle does not necessarily have to be 45°. If the phase angle is not 45°, c_{13} can be estimated by equation (2.21).

Compared to the measurement error in the numerical value, a more important issue associated with the oblique-velocity measurement is: what type of velocity is actually estimated? Yan et al. (2015) discussed that the oblique velocity measured

on a horizontal plug (Wang, 2002a) is not a phase velocity and Wang's data (2002b) needs correction for mistaking group velocity as phase velocity. If we are not sure whether group velocity or phase velocity is measured, errors may be made in both the scalar magnitude of the velocity and the propagation direction. Figure 4.2 shows the wavefront-propagation simulations of the oblique-velocity measurement for two commonly used laboratory anisotropy-measurement setups. The upper panel shows the quasi-P wave velocity measurement on a 45° core plug. The dashed rectangle denotes the cross section of the sample passing the cylindrical axis. The gray dashed lines denote the bedding direction of the TI medium. The diameter of the sample is 25.4 mm and the sample length is 30 mm. The gray bars represent the disc-shaped piezoelectric P-wave transducers and the diameter is 12 mm. The cyan curves are the wavefronts at different times issued from the center of the transmission transducer. The solid arrows denote the ray direction and the dashed arrows denote the phase direction. When the wavefront reaches the interface between the receiver transducer and the end surface of the sample, the wavefront is tangential to this interface. The phase velocity direction is normal to the wavefront. It is parallel to the axial direction of the sample. Although the wave signal emitted from center of the transmission transducer cannot be received by the receive transducer at time T_4, the wave signal emitted from the right corner can be caught by the left corner of the receiver transducer at time T_4, as denoted by the dashed arrow in red. The phase velocity is parallel to the axial direction of the sample and the travel distance is the length of the sample. If the travel time (T_4) can be properly picked from the break time of the first arrival signal, then the sample length divided by the travel time (T_4)

is the phase velocity. Before we know the TI properties of the sample, we do not know the group angle φ and the length of the hypotenuse of the right triangle in red, i.e., the travel distance in the group direction. Therefore, we cannot measure the group velocity directly. On a 45° plug, we are actually trying to measure the travel speed of a deviated plane wave. The deviation of the plane wave off the radial direction of the sample is determined by:

$$\Delta x = L \tan(\varphi - \theta), \tag{4.3}$$

where L is the sample length. The angle difference $\varphi - \theta$ is determined by the TI elastic properties of the measured sample and direction of the sample. The deviation Δx is proportional to the sample length. In practice, for reliable first-break-time picking, the transducer should be wide enough so that at least 10% of the wavefront of the deviated plane wave can arrive simultaneously to the receiver transducer (Dellinger and Vernik, 1994). Obviously, the longer samples require a transducer of greater dimension, but the size of transducer is limited by the measurement setup. If the wavefront of the deviated plane wave is missed by the receiver transducer, the first arrival time related to the phase velocity will be underestimated. Traditionally, a greater sample length is thought to be beneficial for accurate velocity measurement. Therefore, there may be a bias toward underestimation of the phase velocity made on a 45° plug. From equation (2.23), underestimation of the oblique phase velocity leads to underestimation of c_{13}.

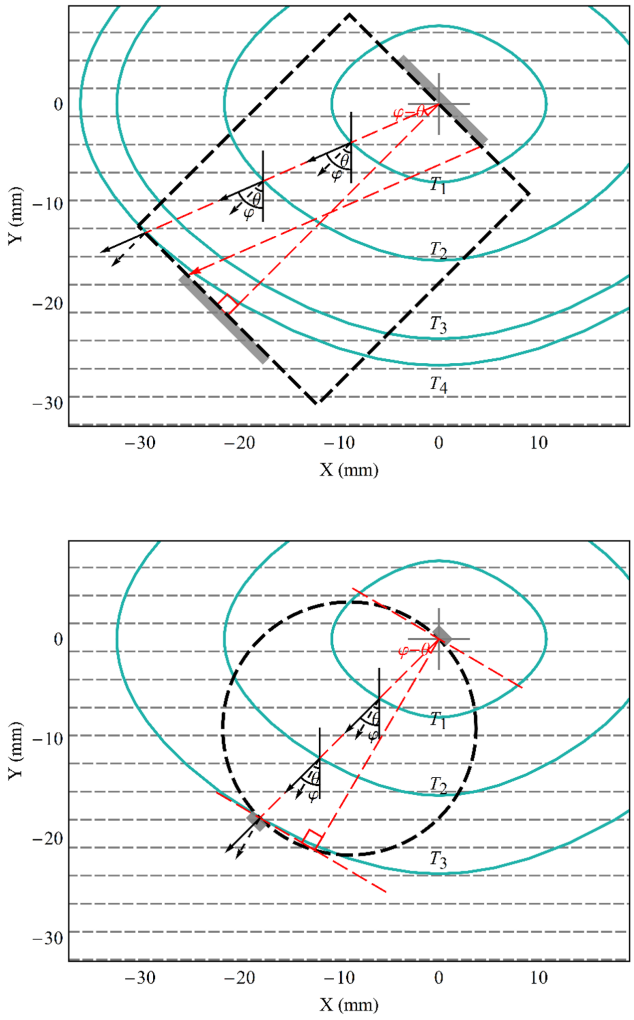

Figure 4.2 Wavefront propagation modeling for quasi-P wave velocity measurement on a 45° plug (above) and a horizontal plug (below). The gray bars represent the piezoelectric transducers. The cyan curves are the wavefronts at different times issued from the center of the transmission transducer. The grey dash lines shows the bedding direction and the black dashed rectangle or circle denote cross-section of the cylindrical sample. The TI medium has same properties as the medium used in Figure 4.1.

The bottom panel of Figure 4.2 shows wavefront-propagation modeling for the oblique-velocity measurement on a horizontal core plug. The dashed disk represents the radial cross section of a horizontal-shale sample with a diameter of 25.4

mm. The gray bars represent the P-wave piezoelectric transducers. The cyan curves are the wavefronts at different times issued from the center of the transmission transducer. The basic principle for group-velocity measurement is "a point source to a point receiver" in the sagittal plane passing the TI symmetrical axis. The transducer has a point contact with the cylindrical surface of the horizontal plug and a line contact in a 3D sense. Since the group velocity direction is in the radial direction, we use the diameter of the sample to divide the travel time allowing the group velocity to be estimated. The distance traveled by the acoustic wave in the corresponding phase direction is represented by the longer leg of the right triangle in red. This distance is not known before the TI elastic properties of the shale sample are estimated. If a buffer is used, its end surface should be flat, so that in the cross section the wave signal is emitted from one point and received by another point. The effect of "a point source to a point receiver" is difficult to achieve on a vertical core plug. If piezoelectric transducers with flat surfaces are used for the oblique-velocity measurement on a horizontal plug, the first arrival signals on different positions of the receiver transducer contacting with sample are synchronized. On a vertical core plug, the first arrival signals at different positions of the receiver transducer contacting with the sample are not synchronized. The overall arrival signal is extended in time and it is difficult to measure the genuine group velocity.

4.4 Experimental Setup and Method

As we analyzed earlier, there are significant uncertainties in the estimation of c_{13} and δ. These uncertainties are primarily related to the oblique-velocity measurement

and can be greatly reduced if multiple oblique velocities are measured. One feasible way to obtain a large amount of reliable laboratory velocity-anisotropy measurement data for the industrial applications is to make multiple oblique-velocity measurements on a single horizontal core plug. The oblique velocities made on the radial directions of a horizontal core plug are group velocities.

Figures 4.3 and 4.4 show the laboratory setup for rotational group-velocity measurement. A uniaxial stress of about 300 psi is applied to the shale sample for good coupling between the transducer buffers and the shale sample. The stress can be easily applied and released by letting the compressed air in or out of the gas chamber located below the beam of the benchtop. After releasing the stress, the core samples can be rotated to the next direction for the next oblique-velocity measurement. In order to acquire the true group velocity, the end surfaces of the transducer buffers should be flat, so that rays are forced to go diametrically across the sample from one point to the other point in the cross section. In a 3D sense, the horizontal core plug has a line contact with the transducer buffers; therefore, the first break signal can be strong enough for accurate travel-time picking. The central frequency of P-wave piezoelectric transducer we used is about 1 MHz.

The multiple P-wave oblique-velocity measurements cannot acquire all the TI elastic constants. The sample is first measured for velocity anisotropy on our 5-component (V_{P0}, V_{P90}, V_{SV90}, V_{SH90}, and $V_{P\varphi 45}$), single-horizontal-plug velocity-anisotropy measurement system (Wang, 2002a; Yan et al. 2012).

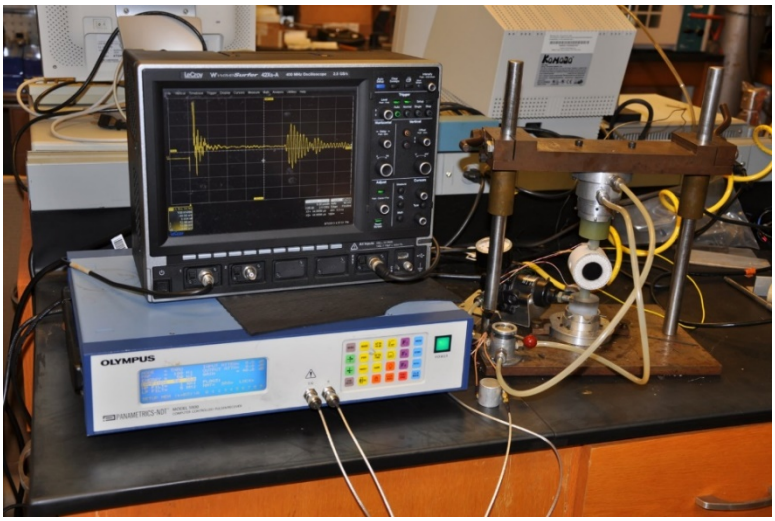

Figure 4.3 Benchtop rotational group-velocity measurement setup.

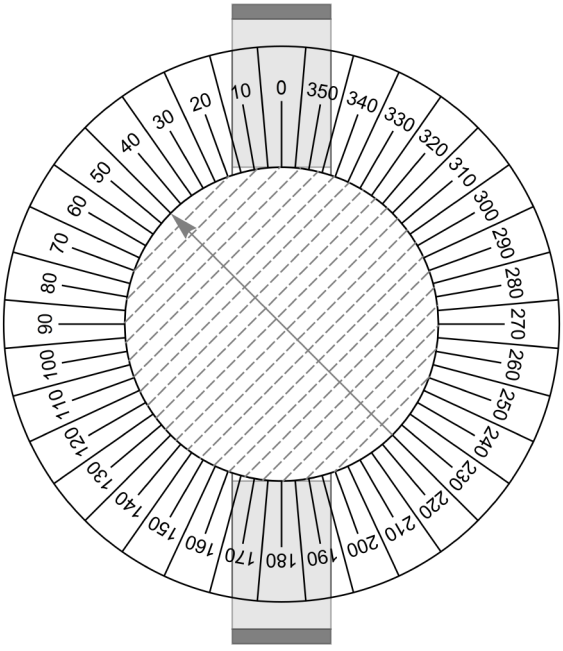

Figure 4.4 Diagram of rotational group-velocity measurements. Inside the phenolite tube marked with an angle panel is the horizontal plug with the dashed lines denoting the bedding direction. The TI symmetry axis is marked on the sample, and the arrow points to the group angle. The dark gray rectangles represent the piezoelectric transducers and the light gray rectangles represent the buffers.

4.5 Measurement Results

The rotational group-velocity measurements are made on two Haynesville shale samples: Sample A and sample B. Figure 4.5 shows the P-wave signal traces at directions from 0° to 180° with respect to the TI symmetrical axis, increasing with 10° interval, for shale sample A. The P-wave signal at 90° (parallel to the bedding) is usually the strongest and clearest compared to the P-wave signals at the other directions. For comparison, the maximum amplitude of the each trace is normalized to one. Due to the limited contact area between the buffers and the sample, the first break signal is very weak relative to the later coming signals. The sequential time variation of the received signals due to direction change is obvious and in a clear trend, as shown in Figure 4.5. The signal around the first-break time marked by the dashed rectangle on the trace at 90° is shown in Figure 4.6. It can be seen that the first arrival P-wave signal are strong enough for confident first-break-time picking. The buffer time has been deducted from the time axis. The error in first-break-time picking is less than 0.05 μs. The absolute velocity error caused by time picking can be controlled by less than 1%. By comparing and matching of the first arrival waveforms between different traces, the relative velocity error between different directions should be much smaller than the absolute velocity error. The short bar on each trace shows the first-break-time we picked. Figure 4.7 shows the estimated P-wave group velocities from two independent velocity-anisotropy measurement systems for sample A. The data points marked by triangles are estimated from the 5-component single-horizontal-plug velocity-anisotropy measurement system, the different data points at the same angle are from different pressure conditions (at

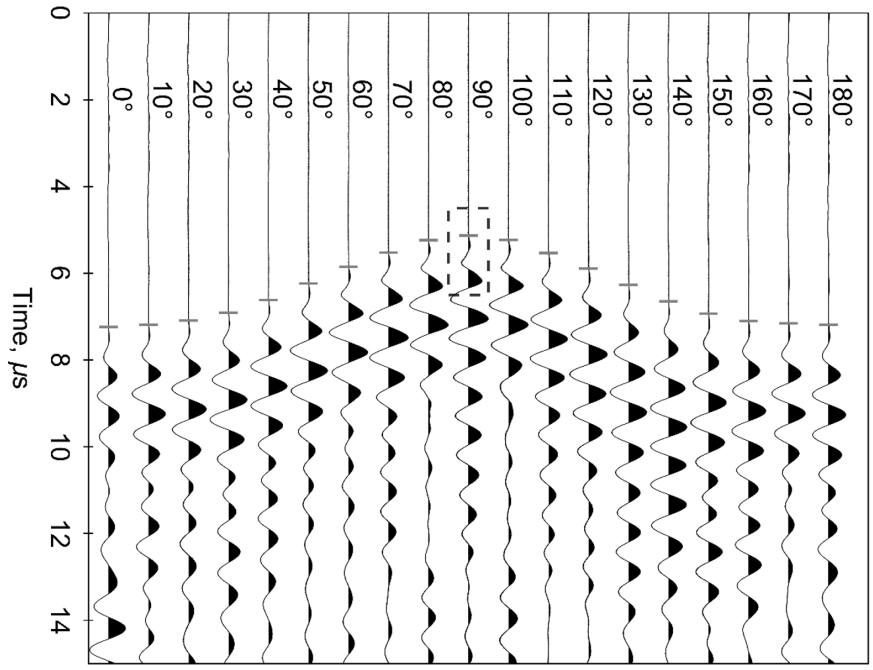

Figure 4.5 P-wave signal traces at different directions with respect to the TI symmetry axis. The first arrival signal in the dashed rectangle on the trace measured at 90° is magnified and shown in Figure 4.6.

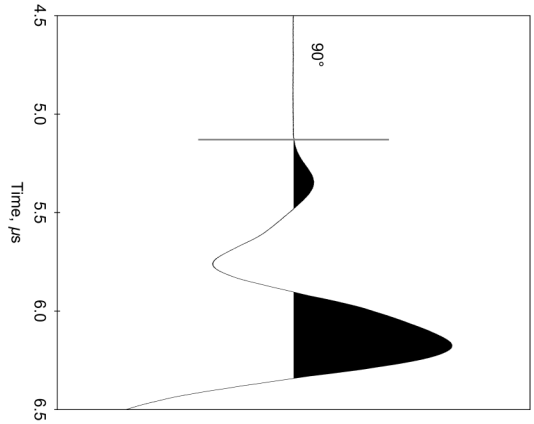

Figure 4.6 Magnification of the P-wave first arrival signal measured at 90°. The first-break time may be not clear in Figure 4.5. It can be picked with confidence after magnification.

differential pressures from 1000 to 5000 psi). The squares with error bars are from the benchtop rotational group-velocity measurements. In spite of the different stress conditions, the two independent measurements are generally consistent. For this sample, the stress effect on velocity is much smaller than the directional dependency.

4.6 TI Elastic Constant Inversion and Sensitivity Analysis

For a TI medium, the quasi-P wave phase velocity is a function of the phase angle and four elastic constants (c_{11}, c_{33}, c_{44}, and c_{13}),

$$V_{\mathrm{P}\theta} = \sqrt{\frac{(c_{11}\sin^2\theta + c_{33}\cos^2\theta + c_{44} + \sqrt{M})}{2\rho}}, \tag{4.4}$$

where

$$M = [(c_{11} - c_{44})\sin^2\theta - (c_{33} - c_{44})\cos^2\theta]^2 + (c_{13} + c_{44})^2\sin^2(2\theta).$$

From equations (4.1-4.2) and equation (4.4), the group velocity is an implicit function of group angle and four elastic constants:

$$V_{P\varphi} = F(\phi, c_{11},, c_{33}, c_{44}, c_{13}). \tag{4.5}$$

From the above implicit relation, the least square regression technique is utilized to find the four elastic constants that can minimize the summation of the squared error:

$$S = \sum_{i=1}^{N}\left(V_{P\varphi data} - V_{P\varphi}\right)^2. \tag{4.6}$$

where N is the number of oblique velocities made in different radial directions. Since group velocities at 19 different group angles were acquired, we should be able

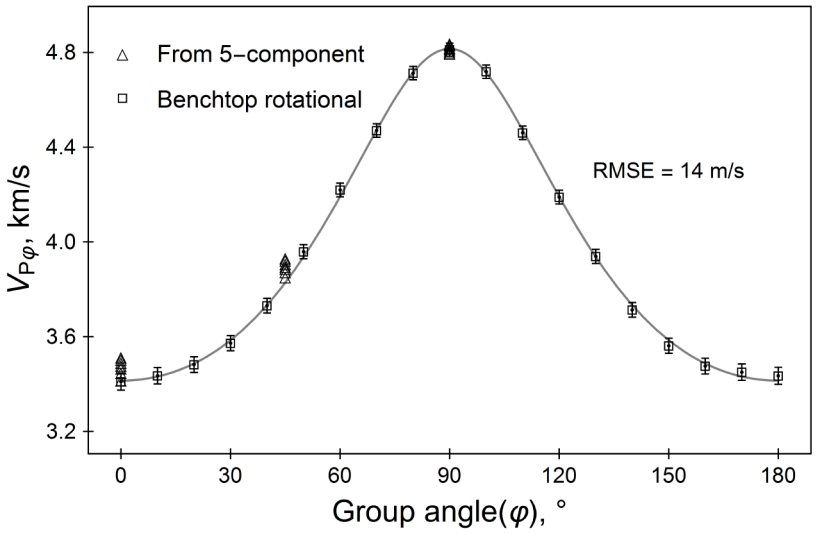

Figure 4.7 Measured group velocities at different directions with respect to the TI symmetry axis for sample A. The curve shows the least square fitting of the measured data using the TI theory.

to invert the four elastic constants by least square fitting. In practice, we found that the inversion results for c_{44} and c_{13} are very dependent on the initial input values. From the sensitivity analysis, we found that there is a coupling relation between c_{44} and c_{13}. In Figure 4.8, c_{11} and c_{33} are kept constant (58.38 GPa and 29.52 GPa, respectively) for all the curves. For each value of c_{44} that is sequentially changed from 3, 6, 9, 12, 15 to 18 GPa, a value of c_{13} can always be found to match the measured group velocity variation trend visually. Considering the measurement uncertainties, no matter how many oblique quasi-P wave velocities are made, it is impossible to simultaneously determine the four elastic constants.

Since the relationship between the group velocity and the four TI elastic constants are not explicit, we will try to use the phase velocity by equation (4.4) to

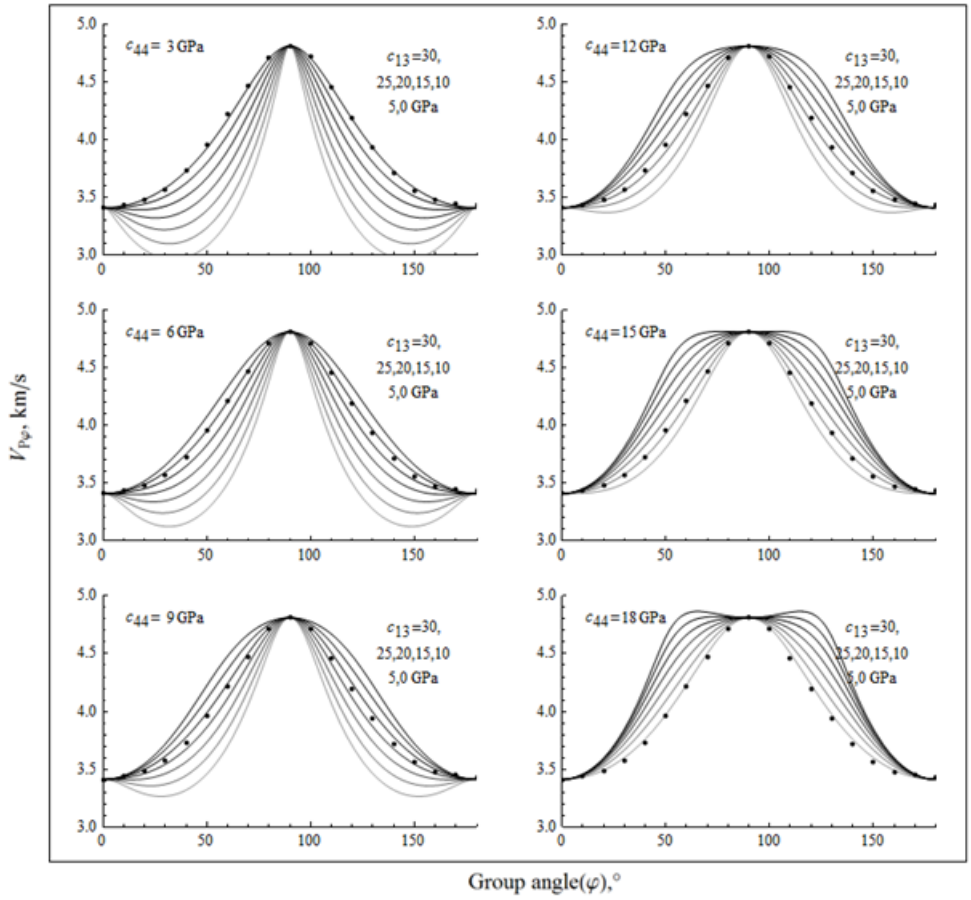

Figure 4.8 Coupling relation between c_{44} and c_{13} in matching the measured group-velocity trend. Let c_{11} and c_{33} be constants, c_{44} and c_{13} are sequentially changed to find possible combinations of c_{44} and c_{13} matching the measured group-velocity trend.

demonstrate the coupling relation between c_{44} and c_{13}. In Figure 4.9, we made similar sensitivity analysis based on velocity-anisotropy measurement data of a Bakken shale sample from Vernik and Liu (1997). The black curve shows the phase velocity based on the laboratory measurement. c_{11} and c_{33} are kept constant and c_{44} is varied sequentially from 5, 7, 9, 11, 13 to 15 GPa. For each c_{44} value, using the hit-and-miss method, we can always find a value for c_{13} that can approximately

match the phase velocity curve based on the laboratory measurements. It can be seen that although the c_{44}-c_{13} pairs are drastically different, the phase velocity curves are almost overlaid with each other. The curves can only be differentiated with each other after significant magnification, as displayed in the inserted plot. The velocity difference is beyond resolution of common laboratory ultrasonic-velocity measurement on core samples. Therefore, c_{44} and c_{13} are practically impossible to be estimated from multiple oblique-velocity measurements. Although the selected c_{44} and c_{13} may have different values from the measured values, the estimated values of δ are close to the true value as long as the phase velocity curve fit with that based on the laboratory measurements.

From the above analysis, for practical applications, the directional dependence of quasi-P wave in a TI medium can be sufficiently described by 3 elastic parameters (V_{P0}, V_{P90}, δ), instead of 4 elastic parameters as shown in equation (4.4). Our observations comply with the theoretical foundation of velocity analysis in TI media (Alkhalifah and Tsvankin, 1995; Tsvankin, 2012). For a layer of TI medium with arbitrary anisotropy, the P-wave reflection travel time can be approximated by:

$$t^2 = {t_0}^2 + \frac{x^2}{V_{\mathrm{Pnmo}}^2} - \frac{(V_{\mathrm{P90}}^2 - V_{\mathrm{Pnmo}}^2)x^4}{V_{\mathrm{Pnmo}}^2({t_0}^2 V_{\mathrm{Pnmo}}^4 + V_{\mathrm{P90}}^2 x^2)}, \tag{4.7}$$

where t_0 is the two-way travel time in the vertical direction and

$$V_{\mathrm{Pnmo}} = V_{\mathrm{P0}}\sqrt{1+2\delta}\,. \tag{4.8}$$

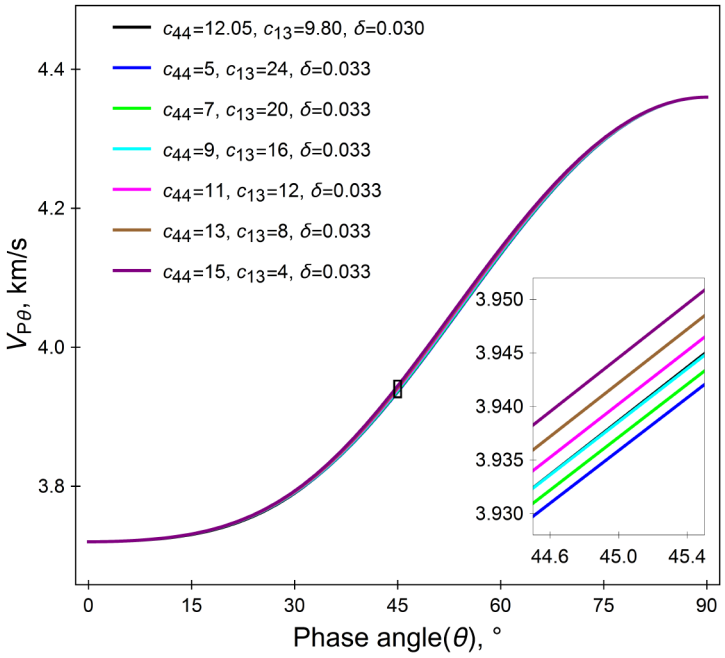

Figure 4.9 Effect of the coupling relation between c_{44} and c_{13} on estimating δ from phase velocity matching (The black curve has properties: c_{11}=45.24 GPa; c_{33}=92.94 GPa, c_{44}=12.05 GPa, c_{13}=9.80 GPa, ρ=2.38 g/cc (Vernik and Liu, 1997. This sample comes from a depth of 11246 feet.), the other curves have same c_{11} and c_{33} values and different c_{44} and c_{13} values.)

The normal moveout behavior of the reflection traveltimes is actually controlled by three elastic parameters: V_{P0}, V_{P90}, and δ.

Although we cannot estimate c_{44} and c_{13} simultaneously from multiple oblique-velocity measurements, c_{44} can be estimated independently from the slow shear wave velocity measurement in the axial direction (i.e., from V_{SV90}). For this study, c_{44} is known from the previous measurements (at a differential pressure of 1000 psi) on the 5-component single-horizontal-plug velocity-anisotropy measurement system. We can estimate c_{11}, c_{33}, and c_{13} simultaneously by fitting the measured

group-velocity data using equations (4.5) and (4.6). As shown in Figure 4.7, the theoretical curve fits the group-velocity data almost perfectly. The estimated ε is 0.50 and δ is 0.25 from the rotational group- velocity measurements, which are close to the results from the previous measurement on the 5-component single-horizontal-plug velocity-anisotropy measurement system (ε=0.49, δ=0.30 at P_d=1000 psi). From the above sensitivity analysis, if we arbitrarily give c_{44} a value, using the least square fitting, we may not get the correct value for c_{13}, but the estimated ε and δ should almost be same as the case when the true value of c_{44} is given. The high-degree of fitting demonstrates that shales can be classified as a typical TI medium.

4.7 Angle Error Detection

In practical laboratory measurement, it is not always straightforward to identify the bedding direction of the shale sample. If the bedding direction is not correctly marked, all the subsequent velocity measurements are wrong. Sometimes we can discover this error because the measured data may be inconsistent. We may have to do the measurement again with corrected reference direction. Sometimes the angle error might not be noticed. In Figure 4.10, we plot the rotational group-velocity measurement data together with the measurement results from the 5-component single-horizontal-plug velocity-anisotropy measurement system for shale sample B. From the rotational group-velocity measurements we noticed that the group velocity at 80° is slightly higher than the group velocity at 90°, and the group velocity at 170° is slightly lower than the group velocity at 180°. This is a good indication that

there may be significant error in identifying the bedding direction. As a result, the TI theory cannot fit the measured group-velocity trend with satisfaction.

The assumed TI symmetric direction marked on the end surface of sample B was re-checked. As shown in Figure 4.11, it is indeed very difficult to tell the bedding direction by visual check and the double arrowed black line was originally identified direction perpendicular to the bedding. The visible crack only cuts through the edge of the sample and does not extend to the section where the oblique velocities are actually made. It should have little effect on the measured oblique velocities. By careful observation from different viewpoints, we realized that quite possibly we made an error in identifying the bedding direction. The red line may be a better judgment of the bedding direction. Considering the angle error, we added a variable $\Delta\varphi$, the group angle correction in the least square fitting. As shown in Figure 4.12, after angle correction, the measured group-velocity data can be fitted with the TI theory much better, and the root mean square error decreases from 122 m/s to 16 m/s. The estimated $\Delta\varphi$ is 6.3°. The velocity data from the 5-component single-horizontal-plug velocity anisotropy system are also based on the wrong bedding direction, but only V_{P0} and $V_{P\phi 45}$ are shifted by the angle correction. V_{P90} is not shifted because it is measured on the axial direction of the horizontal plug. The δ value, estimated from the 5-component single-horizontal-plug velocity anisotropy system, is 0.44; it is 0.36 from the rotational group-velocity measurements and 0.33 after angle correction. The angle error does not cause significant difference in the estimation of δ for this sample, but as shown by Yan et al. (2012), an angle error

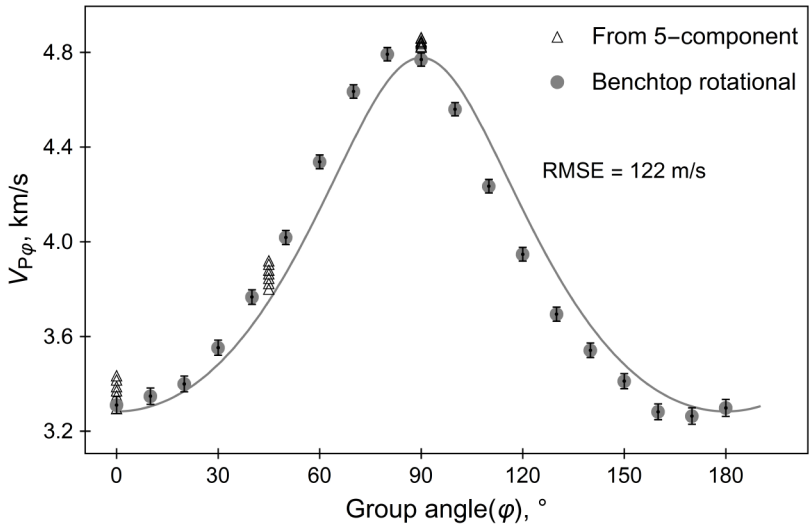

Figure 4.10 Estimation of c_{11}, c_{33} and c_{13} by least square fitting of the group-velocity trend for shale sample B (c_{44} is taken from the 5-component horizontal plug velocity measurement at a differential pressure of 1000 psi).

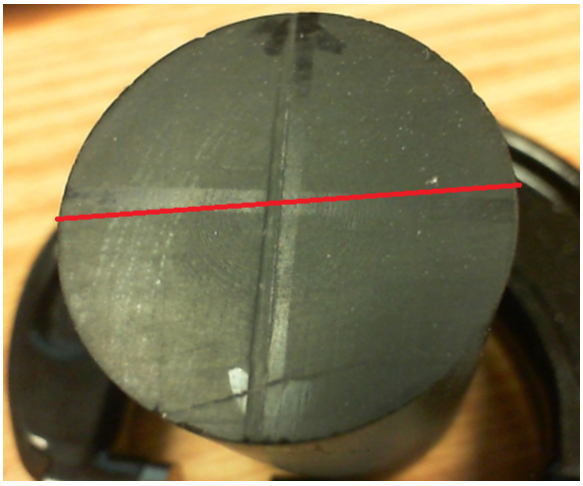

Figure 4.11 Uncertainty in identification of the bedding direction on sample B (1-inch diameter). The double arrow marks the originally determined direction perpendicular to the bedding.

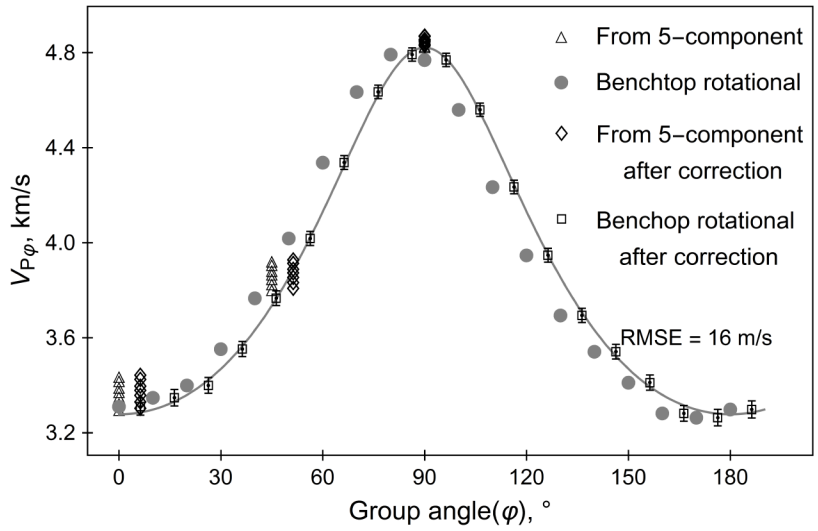

Figure 4.12 Estimation of c_{11}, c_{33}, c_{13} and $\Delta\varphi$ by least square fitting of the group-velocity trend for shale sample B (c_{44} is taken from the 5-component single-horizontal-plug velocity measurement at differential pressure of 1000 psi). Except the velocities measured at the axial direction, all other velocities measured at radial directions are shifted by 6.3°, which is determined by least square fitting using the TI theory.

of 5° can cause large error in c_{13} and δ in some cases. Identification and correction of possible angle error is another important reason that justifies the necessity for multiple oblique-velocity measurements.

4.8 Discussion

The first arrival signals of the rotational group-velocity measurement are not ideally in good shape with relatively strong first arrival signal and short time duration. The P-wave transducers are made of economical piezoelectric ceramic disks with central frequency of 1 MHz. They are attached to PEEK buffers without any damping material or design to improve the quality of the first arrival signal. If the transducers

are commercially made, the quality of the first arrival signal can be significantly improved. The stress condition of the rotational group-velocity measurement on the benchtop are far from that in-situ. If the shale sample has visible cracks along bedding, the wave signal in direction perpendicular to the bedding may be too weak for first-break-time picking, and the sample can easily be broken under uniaxial stress of hundreds of psi. It is preferred that the multiple oblique-velocity measurement unit be built into a pressure vessel. It is too expensive and technically challenging to build a rotating mechanism into the pressure vessel. A practical way is to add more P-wave transmission-receiver pairs on the jacket in radial directions based on the 5-component single-horizontal-plug velocity-anisotropy measurement setup (Wang, 2002a). Limited by the circumference of the core plug or the jacket, the P-wave transmission-receiver pairs can be separated into three groups located on different positions along the axial direction of the sample or jacket. Each group can have 3 or 4 pairs of P-wave transmission-receiver pairs in the radial cross section; and therefore, 9 or 12 P-wave velocities can be measured in different directions with respect to the TI symmetry axis.

4.9 Conclusions

The rotational group-velocity measurements show that shales can be classified as a typical transversely isotropic medium in terms of elastic properties. It is feasible and necessary to make multiple oblique P-wave velocity measurements on a single horizontal core plug to reduce the uncertainties in estimating c_{13} and the Thomsen parameter δ. There is a coupling relation between c_{44} and c_{13} on the directional

dependence of seismic velocities in a TI medium. The coupling relation confirms the theoretical soundness of estimating the anisotropy parameters from seismic data using the velocity-analysis technique.

4.10 Acknowledgements

This study is sponsored by the Fluids and DHI consortium of the Colorado School of Mines and the University of Houston.

4.11 References

Alkhalifah T. and Tsvankin I. 1995. Velocity analysis for transversely isotropic media. *Geophysics* **60**, 1550-1566.

Banik N.C. 1987. An effective anisotropy parameter in transversely isotropic media. *Geophysics* **52**, 1654-1664.

Blum T.E., Adam L. and van Wijk K. 2012. Laboratory measurement of P- wave anisotropy in shales with laser ultrasonics. *SEG Expanded Abstracts*.

Blum T.E., Adam L. and van Wijk K. 2013. Noncontacting benchtop measurements of the elastic properties of shales. *Geophysics* **78**, C25-C31.

Dellinger J.A. and Vernik L. 1994. Do traveltimes in pulse-transmission experiments yield anisotropic group or phase velocities? *Geophysics* **59**, 1774- 1779.

Jakobsen M. and Johansen T.A. 2000. Anisotropic approximations for mudstones: A seismic laboratory study. *Geophysics* **65**, 1711-1725.

Johnston J.E., and Christensen N.I. 1995. Seismic anisotropy of shales. *Journal of Geophysical Research* **100**, 5591-6003.

Sarout J., Piane C.D., Nadri D., Esteban L. and Dewhurst D.N., 2015. A robust experimental determination of Thomsen's δ parameter. *Geophysics* **80**, A19-A24.

Sayers C.M. 2004. Seismic anisotropy of shales: What determines the sign of Thomsen's delta parameter*? SEG Expanded Abstracts*.

Sondergeld C.H., Rai C.S., Margesson R.W. and Whidden K.J. 2000. Ultra- sonic measurement of anisotropy on the Kimmeridge Shale*. SEG Expanded Abstracts*.

Sondergeld C.H. and Chandra S.R. 2011. Elastic anisotropy of shales. *The Leading Edge* **30**, 325-331.

Sone H. 2012. *Mechanical Properties of Shale Gas Reservoir Rocks and Its Relation to In-situ Stress Variation Observed in Shale Gas Reservoirs.* Ph.D. thesis, Stanford University.

Thomsen L. 1986. Weak elastic anisotropy. *Geophysics* **51**, 1954-1966.

Thomsen L. 1990. Poisson was not a geophysicist, *Geophysics: The Leading Edge of Exploration*, December 1990.

Tsvankin I., 2012. *Seismic Signatures and Analysis of Reflection Data in Anisotropic Media*. 3rd edition, SEG.

Vernik L. and Nur A. 1992. Ultrasonic velocity and anisotropy of hydrocarbon source rocks. *Geophysics* **57**, 727-735.

Vernik L. and Liu X. 1997. Velocity anisotropy in shales: A petrophysical study: *Geophysics* **62**, 521-532.

Wang Z. 2002a. Seismic anisotropy in sedimentary rocks, part 1: A single- plug laboratory method. *Geophysics* **67**, 1415-1422.

Wang Z. 2002b. Seismic anisotropy in sedimentary rocks, part 2: Laboratory data: *Geophysics* **67**, 1423-1430.

Yan F., Han D.-h. and Yao Q. 2012. Oil shale anisotropy measurement and sensitivity analysis. *SEG Expanded Abstracts*.

Yan F., Han D.-h. and Yao Q. 2015. Physical constraints on c_{13} and δ for transversely isotropic hydrocarbon source rocks. *Geophysical Prospecting*, doi: 10.1111/1365-2478.12265.

Chapter 5

Sensitivity Analysis of Seismic Anisotropy Parameter Estimation

5.1 Abstract

There are significant uncertainties in estimating δ from the laboratory measurement when the dimensions and orientations of the rock samples are known. It is natural to believe that more challenges will be encountered in the estimation of the seismic anisotropy parameters from field-seismic data. Based on transversely isotropic (TI) layer-cake model randomly parameterized by the laboratory anisotropy-measurement data, we apply the commonly used quartic non-hyperbolic moveout velocity-analysis method to estimate the seismic anisotropy parameters. The methodology is tested on its sensitivity to the layering effect, the source-receiver offset, the vertical interval velocity error, and the time-picking error. The results show this methodology is theoretically well-established and it works better for deeper layers and shorter offset data. However, in presence of normal-level noises, this method is sensitive to the time-picking error and requires the offset be greater than the depth of the reflection event. The uncertainties in seismic anisotropy parameter estimating increase rapidly for

deeper layers. Generally, δ is more reliably determined than ε and ε is more reliably determined than the anellipticity parameter η.

5.2 Introduction

The importance of seismic anisotropy in petroleum exploration is well-accepted (Alkhalifah and Tsvankin, 1995; Helbig and Thomsen, 2005). Due to the layering structure and intrinsic anisotropic properties of the mudstones, sedimentary basins are usually anisotropic in seismic properties in the field scale. However, accounting effects of seismic anisotropy is still not a common practice in seismic-data processing and interpretation. The difficulties primarily lie in the estimation of the anisotropy parameters.

There are different methods recently developed for the estimation of the anisotropy parameters (White et al., 1983, Gaiser, 1990; Alkhalifah et al. 1995; Baan, et al, 2002; Isaac and Lawton, 2004). Xiao (2006) made a comparative study of different methods of anisotropy-parameter estimation. She found the quartic non-hyperbolic moveout equation formulated by Alkhalifah and Tsvankin (1995) can be applicable to VTI media of arbitrary anisotropy and has the best performance among the methods of anisotropy-parameter estimation using velocity-analysis approach. Many applications of VTI anisotropy-parameter estimation are based on this formulation (Alkalifah, 1997; Grechka and Tsvankin, 1998; Toldi et al., 1999; Wang and Tsvankin, 2009). Tsvankin (2005, 2012) further improved and systematically documented this method.

Laboratory anisotropy-measurements are an important means to study the seismic anisotropic properties of subsurface rocks and calibrate the results of anisotropy-parameter estimation from seismic data. Sedimentary basins primarily consist of shales in terms of volume fraction. Shales are the primary hydrocarbon-source rocks and can be important reservoir rocks with advancing drilling and hydraulic fracturing techniques. There are a lot of experimental studies of the seismic anisotropic properties of shales (Jakobsen and Johansen, 2000; Wang, 2002; Sondergeld and Rai, 2011; Sone, 2012; Yan et al. 2012; Blum et al., 2013; Sarout et al., 2015). From the relationship between the principal Poisson's ratios of a TI (transversely isotropic) medium, Yan et al. (2015) derived physical constraints on c_{13} for shales. Using the physical constraints on c_{13} as a tool of quality control, Yan et al. (2015) found that there are significant uncertainties in the estimation of c_{13} and δ. For shales with TI anisotropy, it should be satisfied that $0<\nu_{HH}<\nu_{HV}$. As shown in Figure 2.7, this relation is not satisfied for a lot of data points, which means that δ is incorrectly estimated or the sample should not be classified as a TI medium. The physical meanings of the two principal Poisson's ratios (ν_{HH} and ν_{HV}) are self-evident from the inserted diagram that represents deformation of a horizontal plug under uniform axial compression testing.

In laboratory anisotropy measurement, the dimensions and orientation of the rock samples are known, and the measurement directions are controllable, but there are still significant uncertainties in the estimation of δ. The core measurement data are usually used to calibrate the logging data and the logging data are used to calibrate seismic data. For field-seismic data, we do not know the subsurface geometry and have limited

control on the measurement directions, it is expected that the estimation of the anisotropy parameters becomes more challenging. The goal of our study is to select one of the widely implemented anisotropy-parameter estimation methods and study its sensitivity to various factors that may be encountered in the practical applications. The sensitivity analysis results should supply useful guidance for effective implementation of the methodology.

5.3 Procedure of TI Parameter Estimation

In this study, we follow the procedure of TI parameter estimation proposed by Alkhalifah and Tsvankin (1995) and Tsvankin (2012). This procedure mimics the procedure of velocity-analysis for the isotropic media. First, we use equation (1) to compute the effective NMO (normal moveout) velocity ($V_{Pnmo}(i)$) and the effective horizontal velocity ($V_{Phor}(i)$) for each layer interface. Here the normal text (i) refers to the i-th layer. These velocities are "effective" because they include the wave propagation effect from the overburden layers.

$$t^2(x,i) = {t_0}^2(i) + \frac{x^2}{V^2_{\mathrm{Pnmo}}(i)} - \frac{\left(V^2_{\mathrm{Phor}}(i) - V^2_{\mathrm{Pnmo}}(i)\right)x^4}{V^2_{\mathrm{Pnmo}}(i)\left({t_0}^2(i)V^4_{\mathrm{Pnmo}}(i) + V^2_{\mathrm{Phor}}(i)x^2\right)}. \tag{5.1}$$

For the second step, equation (5.2) is used to compute the interval NMO velocities.

$$V^{(i)}_{\mathrm{Pnmo}} = \sqrt{\frac{V^2_{\mathrm{Pnmo}}(i)t_0(i) - V^2_{\mathrm{Pnmo}}(i-1)t_0(i-1)}{t_0(i) - t_0(i-1)}}. \tag{5.2}$$

Here the superscript (i) refers to the interval properties. For the third step, the intermediate parameter *g(i)* is computed for each layer:

$$g(i) = V_{\mathrm{Pnmo}}^2(i)(4V_{\mathrm{Phor}}^2(i) - 3V_{\mathrm{Pnmo}}^2(i)). \quad (5.3)$$

For the fourth step, equations (5.4) and (5.5) are used to compute the interval horizontal velocity ($V_{Phor}^{(i)}$) and the anelliptical parameter $\eta^{(i)}$.

$$V_{\mathrm{Phor}}^{(i)} = V_{\mathrm{Pnmo}}^{(i)} \sqrt{\frac{1}{4(V_{\mathrm{Pnmo}}^{(i)})^4} \frac{g(i)t_0(i) - g(i-1)t_0(i-1)}{t_0(i) - t_0(i-1)} + \frac{3}{4}}, \quad (5.4)$$

$$\eta^{(i)} = \frac{1}{8\left(V_{\mathrm{Pnmo}}^{(i)}\right)^4} \left(\frac{\mathrm{g}(i)\, t_0(i) - \mathrm{g}(i-1)\, t_0(i-1)}{t_0(i) - t_0(i-1)} - \left(V_{\mathrm{Pnmo}}^{(i)}\right)^4 \right), \quad (5.5)$$

where η is the anellipticity parameter introduced by Alkhalifah and Tsvankin (1995),

$$\eta = \frac{\varepsilon - \delta}{1 + 2\delta}, \quad (5.6)$$

where ε and δ are the Thomsen parameters (Thomsen, 1986).

If the vertical interval velocities are known from the well logging data or check shot survey, ε and δ can be calculated using the previously estimated parameters:

$$\varepsilon = ((\frac{V_{\mathrm{Phor}}}{V_{\mathrm{P0}}})^2 - 1)/2, \quad (5.7)$$

$$\delta = \frac{\varepsilon - \eta}{1 + 2\eta}, \quad (5.8)$$

In summary, by fitting equation (5.1) with the reflection traveltimes, we get the effective normal-moveout velocity (analog to the stacking velocity for the isotropic case) and the effective horizontal velocity. Using the Dix-type equation, the interval normal-moveout velocity and the horizontal velocity are computed. From the relationship between the interval normal-moveout velocity and the horizontal velocity, the anellipticity parameter η is calculated. Knowing the vertical interval velocity, ε can be calculated from the interval horizontal velocity. δ can be calculated from ε and η.

5.4 TI Model Parameterization and Ray Tracing

The sensitivity testing is based on a synthetic layered TI model. It consists of 15 layers with equal thickness of 50 meters. The elastic properties of each layer are parameterized based on the laboratory anisotropy-measurement data. To make the layered TI model physically rational, only data points with δ lying within the physical bounds as shown in Figure 2.7 can be a candidate for the model parameterization. In total there are 203 data points and 137 data points have δ lying within the bounds. For each simulation, 15 data points are randomly selected and the corresponding elastic properties are assigned to each of the 15 layers in the synthetic model. Without specification, 100 simulations are run for each type of sensitivity testing so that the test results are not specific to a certain type of rocks or a certain sequence of rocks.

The traveltimes are computed using the seismic ray theory. For TI media, the Snell's law is in the same form as for the isotropic media (Slawinski et al., 2000):

$$p = \frac{Sin\theta_i}{V_{P\theta i}}, \tag{5.9}$$

where p is the ray parameter. It is a constant for a certain ray. "i" refers to the i-th layer. It should be emphasized here that the angle is a phase angle and the velocity must be the phase velocity, not a group angle and the group velocity. In an isotropic medium, the phase angle and the group angle, and the phase velocity and group velocity are identical.

Since the actual traveltime is determined by the ray path and the ray (group) velocity, at each interface there is a need to convert the phase angle to the group angle and the phase velocity to the group velocity using the relationship (Byun, 1984):

$$\mathrm{Tan}(\varphi - \theta) = \frac{1}{V_\theta}\frac{\mathrm{dV}_\theta}{\mathrm{d\theta}}, \tag{5.10}$$

$$V_\theta = V_\varphi \cos(\varphi - \theta)\ . \tag{5.11}$$

Figure 5.1 shows an example of ray tracing on the synthetic TI model. From 0° to the maximum shooting phase angle, 20 rays are shot at the top of the top layer in equal phase angle intervals. For clarity, only rays that are reflected on the bottoms of layers 5, 10, and 15 are shown. The gray level of the layer represents the degree of P-wave anisotropy (Thomsen parameter ε), which lies around 0 to 0.5. It can be seen that anisotropy has a strong effect on the bending of the rays. Figure 5.2 shows the reflection traveltimes for each of the interfaces.

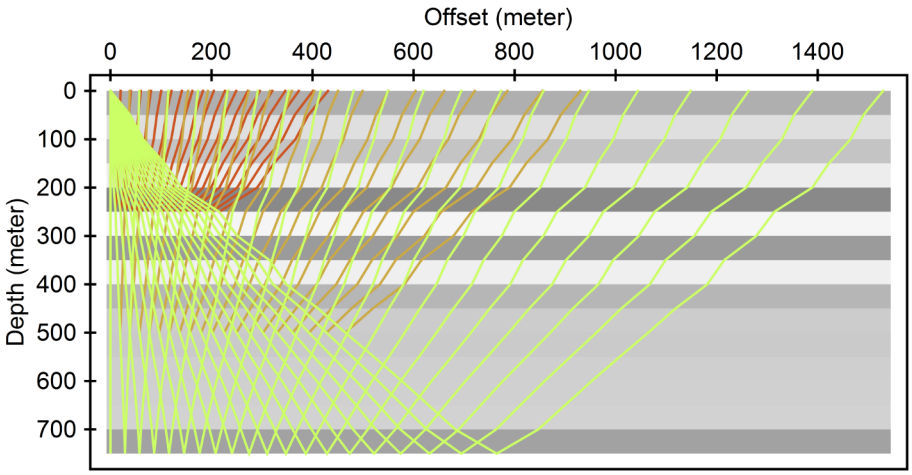

Figure 5.1 Seismic ray tracing on a synthetic TI model. The TI model consists of 15 layers with equal thickness of 50 meters. Only rays that are reflected on layers 5, 10, and 15 are shown. Parameterization of the synthetic TI model is based on the laboratory measurement results as shown in Figure 1. The gray level indicates the degree of P-wave anisotropy.

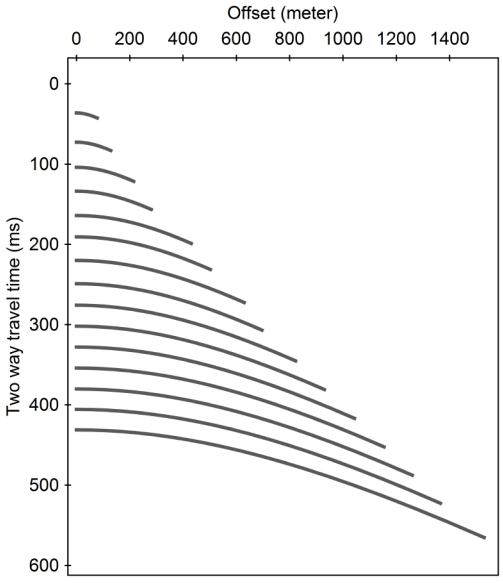

Figure 5.2 Two-wave traveltimes for the reflection events at the interfaces in the synthetic TI model shown in Figure 5.1.

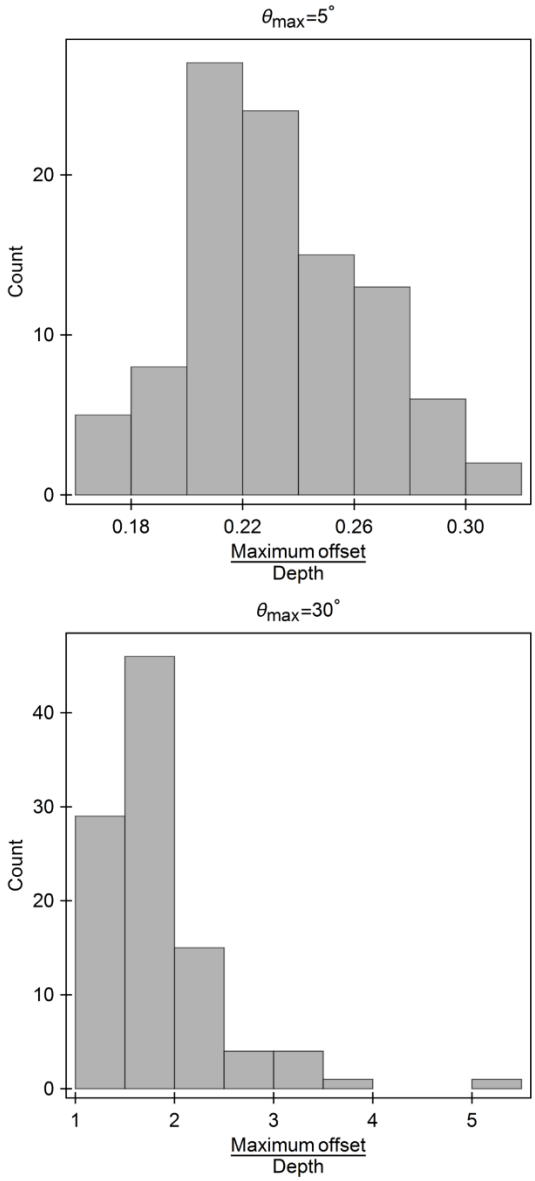

Figure 5.3 Distribution of the maximum offset to depth ratios when the maximum shooting phase angles are 5° and 30°, respectively. Here the count denotes times of simulations.

For each simulation, the model's parameters are randomly selected from the laboratory measurement database. For the same maximum incident angle, the actual maximum offsets are model dependent. They are different for each simulation. Figure 5.3 shows

the distribution of the ratios of the maximum offset to the depth for 100 simulations when the maximum shooting phase angles are 5° and 30°, respectively. For the maximum shooting phase angle of 5°, the maximum offset is around one fifth of the depth. For the maximum shooting phase angle of 30°, the maximum offsets are usually greater than the depth, which can be treated as a case of far offset acquisition. The offset is fully controllable using the two-point tray tracing technique. Over hundreds of simulations are conducted in this study, for computation efficiency, this technique is not utilized.

5.5 Sensitivity Testing of the Layering Effect

One of the important mechanisms causing seismic anisotropy is the layering effect. In a sedimentary basin, even if each of the formation layers of various thicknesses is isotropic, the effective properties of the formation are anisotropic (Backus, 1962). The layered structure causes non-hyperbolic reflection moveout. It would be good to know whether the anisotropy-parameter estimation can achieve similar accuracy for the top layers and bottom layers. In this test, no errors were introduced for the vertical interval velocities and the reflection traveltimes. The maximum shooting phase angle is 30°.

Figures 5.4 to 5.6 show the correlations between the actual model parameters and the estimated values for ε, δ, and η, respectively. Since there is no time-picking error, the estimation of the anisotropy parameters is generally excellent. Therefore, equation (5.1) is a very good approximation of the non-hyperbolic reflection time curve for TI media with arbitrary anisotropy and the anisotropy-parameter estimation procedure introduced is theoretically valid. It can be seen that the estimation of the anisotropy

parameters for layer 15 is slightly more accurate than for layer 5. The anisotropy induced by the layering effect should have no adverse effect on the anisotropy-parameter estimation. It is observed that the estimation of δ has less uncertainty than the estimation of ε. From the anisotropy-parameter estimating procedure introduced early, the Thomsen parameters are actually estimated from the normal-moveout velocity V_{nmo} and the horizontal velocity V_{hor}. The following exact relations stand for a TI medium with arbitrary anisotropy (Tsvankin, 2012):

$$V_{nmo} = V_{P0}\sqrt{1+2\delta}, \tag{5.12}$$

$$V_{hor} = V_{nmo}\sqrt{1+2\eta} = V_{P0}\sqrt{1+2\varepsilon}\,. \tag{5.13}$$

Since the vertical velocity V_{P0} is given, the estimation of δ is dependent on the estimation of V_{Pnmo}, and the estimation of ε is dependent on the estimation of V_{Phor}. Therefore, the estimation of V_{Pnmo}, is more accurate than the estimation of V_{Phor}, which is reasonable because the estimation of V_{Phor} may need a large offset. The estimation of η is the worst because it is affected by both V_{Pnmo} and V_{Phor}. .

5.6 Sensitivity Testing of the Offset

In order to have reliable estimation of the horizontal velocities, it is often believed that seismic data with much longer offset than usual are required. In the last testing, the

maximum shooting angle is 30°, which corresponds to an offset-depth ratio of about 2.0. To observe the effect of offset on anisotropy-parameter estimation, we conducted similar testing using maximum shooting angle of 5°. As shown in Figure 5.3, the ratios

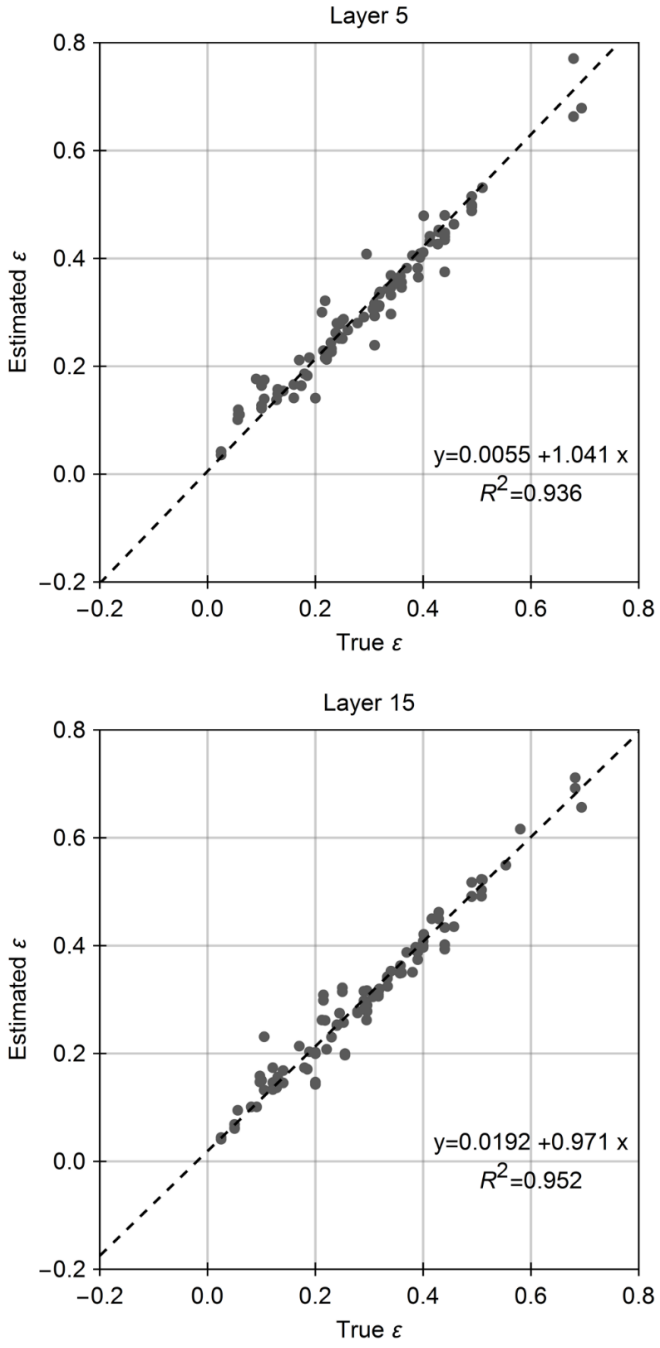

Figure 5.4 Uncertainty in the estimation of ε when there is no error in vertical velocity determination and traveltime picking. The maximum shoot phase angle is 30°.

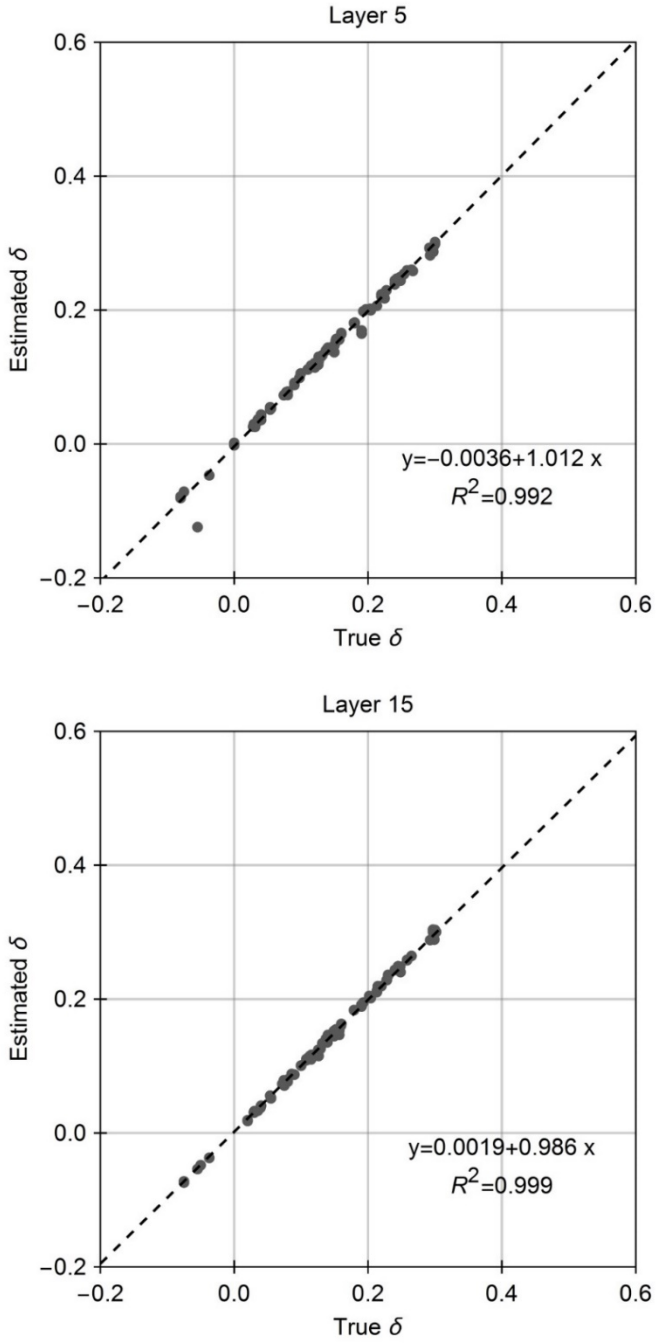

Figure 5.5 Uncertainty in the estimation of δ when there is no error in vertical velocity determination and traveltime picking. The maximum shoot phase angle is 30°.

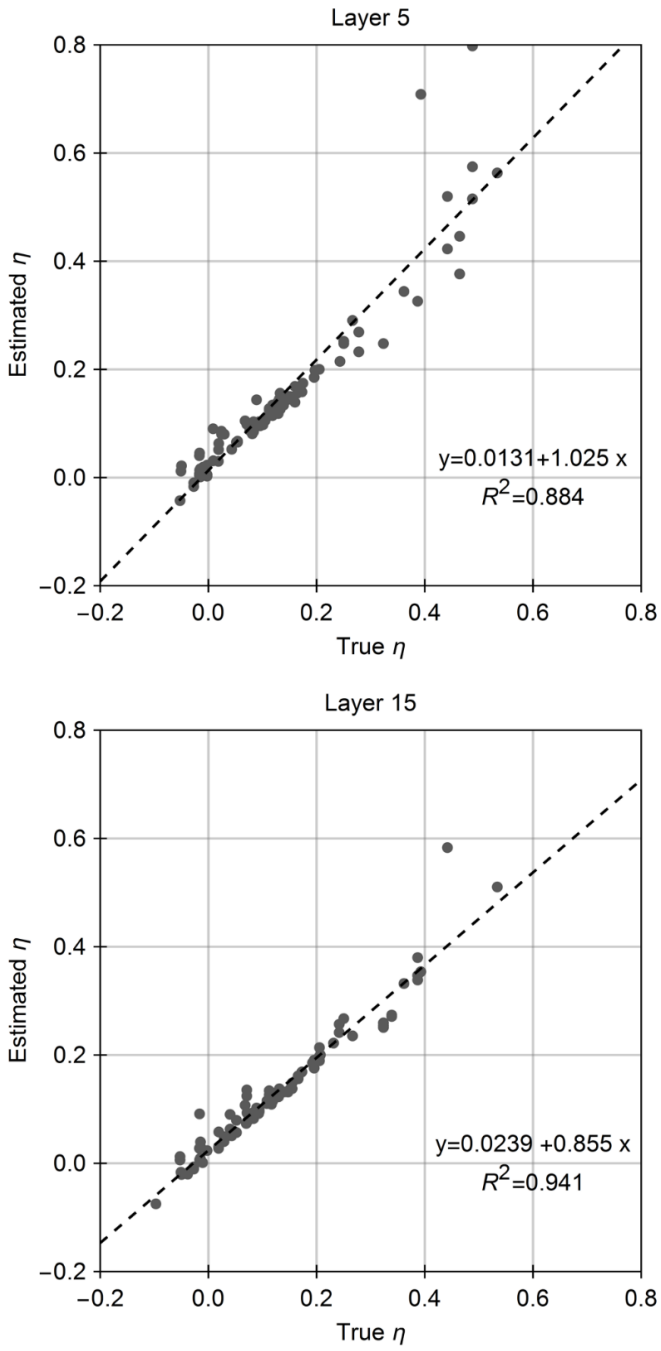

Figure 5.6 Uncertainty in the estimation of η when there is no error in vertical velocity determination and traveltime picking. The maximum shoot phase angle is 30°.

of offset to depth are distributed around 0.25 and the shooting-receiver offsets are generally very short. It is assumed that there is no error in V_{P0} determination and traveltime picking. From the sensitivity testing in the last section, the layering effect has little effect on the anisotropy-parameter estimation; therefore, only the simulation results for layer 15 are shown in this section. Figure 5.7 shows the uncertainties in the estimation of ε and δ for layer 15. Comparing Figure 5.7 with Figures 5.4 and 5.5, we can see that the estimation of the anisotropy parameters is more accurate by using the short-offset synthetic data than the long-offset synthetic data. Figure 5.8 shows a comparison of the horizontal velocity estimation by using the long-offset and short-offset synthetic data, respectively. It can be seen that the horizontal velocity is more accurately estimated using the shorter offset data.

The above modeling results appear to be contradictory to our common sense, but it is theoretically explainable. Equation (5.1) is a quartic Taylor series approximation of the non-hyperbolic normal-moveout curve. The Taylor series approximation is more accurate for smaller offset. Therefore, if there is no noise, a better estimation of the anisotropy parameters can be achieved using the shorter offset data. The normal-moveout velocity is defined as the slope of the normal-moveout curve when the offset goes to zero (Thomsen, 1986). Therefore, theoretically the normal-moveout velocity can be more reliably estimated using the shorter offset data.

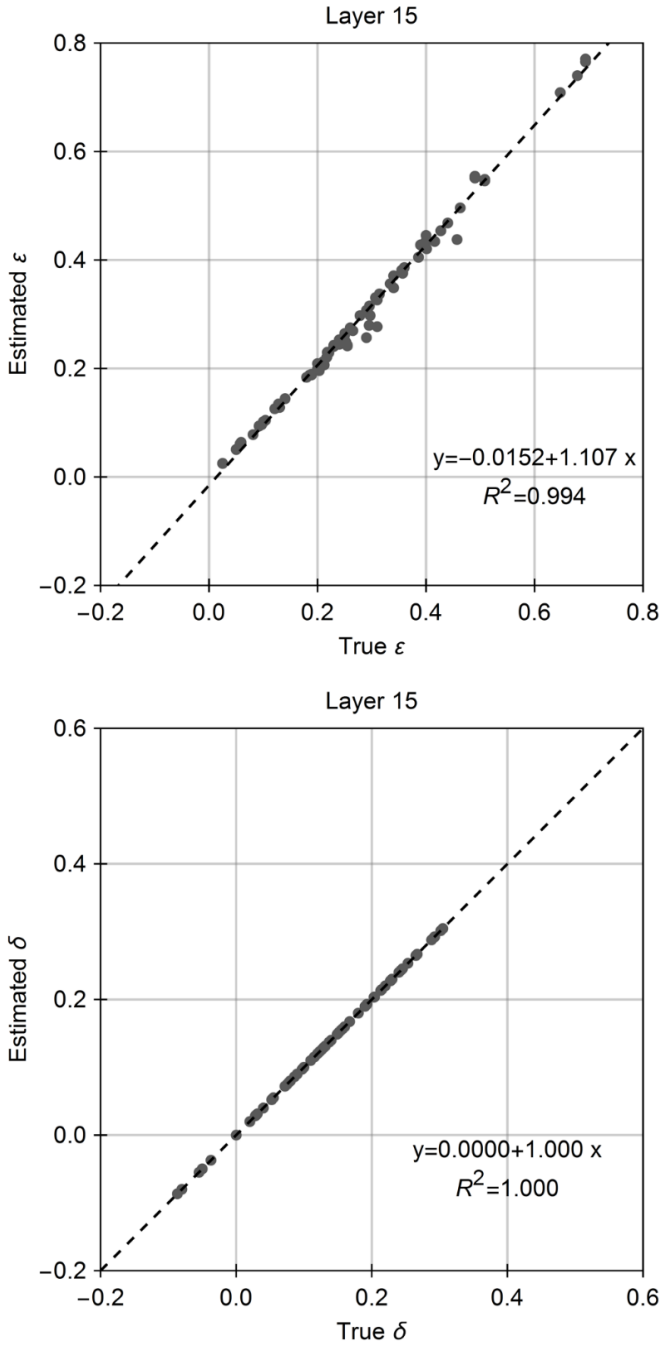

Figure 5.7 Uncertainties in the estimation of ε and δ when there is no error in vertical velocity determination and traveltime picking. The maximum shoot phase angle is 5°.

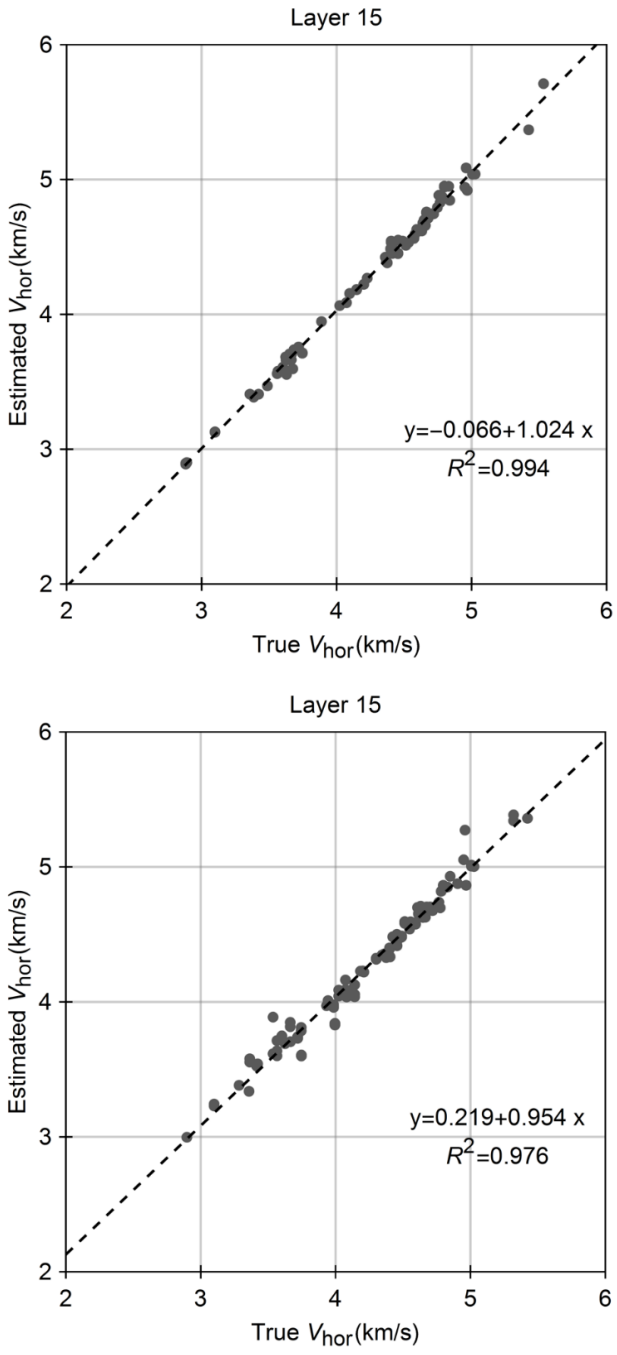

Figure 5.8 Uncertainty in the estimation of the horizontal velocity when there is no error in vertical velocity determination and traveltime picking. The maximum shoot phase angles are 5° for the top panel and 30° for the bottom panel.

5.7 Sensitivity testing of the V_{P0} error

In traditional seismic-data processing, the estimation of the vertical interval velocities is challenging under assumption of isotropy. To estimate the extra anisotropic parameters, it is often necessary to assume the vertical interval velocities are known from the other data sources, such as the sonic logging data and VSP data. From the anisotropy parameter estimating procedure introduced in the earlier section, the vertical interval velocity is used after the normal-moveout velocity and horizontal velocity are determined to estimate the Thomsen parameter ε and δ. Therefore, the error in the vertical interval velocities does not affect the estimation of the normal-moveout velocity, the horizontal velocity, and the anellipticity parameter η. In this testing, it is assumed that there is no error in traveltime picking. The maximum shooting phase angle is 30°.

In Figures 5.9 and 5.10, we tested the effect of the random velocity error of [-2%, +2%] and [-5%, +5%] on the estimation of ε and δ. The maximum random error of 2% may correspond to the vertical interval velocity data with good to excellent quality. The maximum random error of 5% may correspond to the vertical interval velocity data with fair quality. In Figure 5.10, the estimation of ε is generally acceptable if the error in the vertical interval velocity does not excess the P-wave anisotropy. Since the estimation of the normal-moveout velocity is more accurate than the horizontal velocity, the estimation of δ is more accurate than the estimation of ε, as seen from equations (5.12) and (5.13).

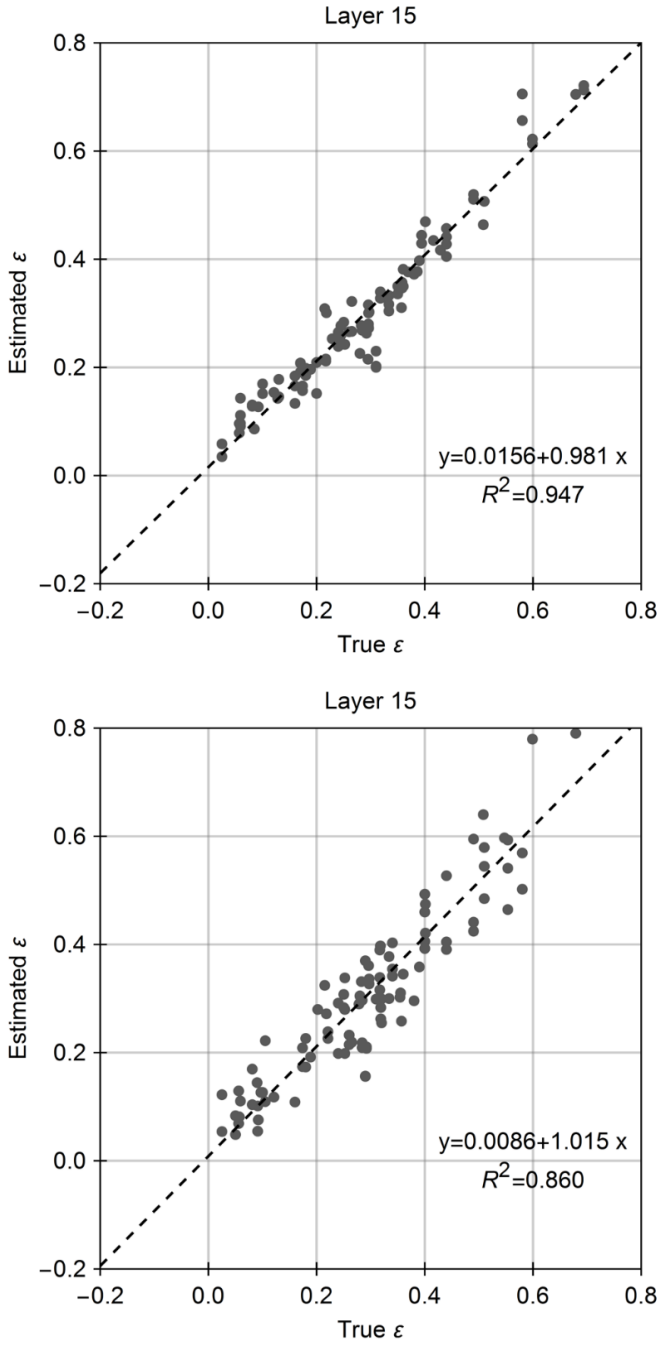

Figure 5.9 Uncertainty in the estimation of ε when there is an error in vertical velocity determination but no error in traveltime picking. The maximum random error in determining V_{P0} is ±2% for the top panel and ±5% for the bottom panel.

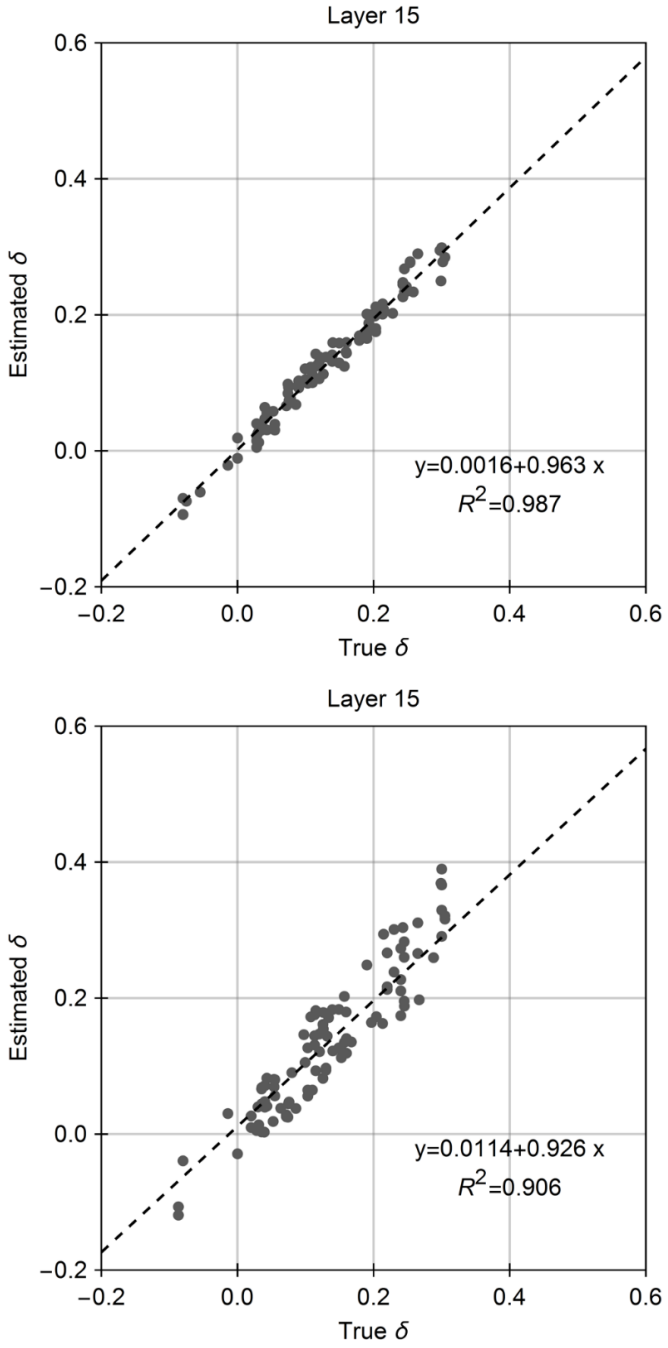

Figure 5.10 Uncertainty in the estimation of δ when there is an error in vertical velocity determination but no error in traveltime picking. The maximum random error in determining V_{P0} is ±2% for the top panel and ±5% for the bottom panel.

From the above testing, if the horizontal lithology variation is not significant, the estimation of the anisotropy parameters can be extended to areas away from the wells.

5.8 Sensitivity Testing of Time-Picking-Error

There are always some noises affecting the traveltime picking along the reflection events in field-seismic data. For example, the noises can come from the multiples, the converted wave, the tuning effect of thin layers, and field noises. In this experiment, we will test the effect of random noise on the estimation of the anisotropy parameters. The random noise lies in between -0.1% and +0.1% of the theoretical two-way traveltimes. This error corresponds to a time error of about 1 ms for a reflection event lying around 1000 ms. Obviously, this noise level is much lower than the common noise level of field- seismic data. For this experiment, a random error between -2% to +2% is also added to the interval vertical velocities. The maximum shooting phase angle is 30°.

Figures 5.11 to 5.12 show the effect of the time-picking- error and the vertical velocity error on the estimation of ε, δ for layers 1, 5, 10, and 15, respectively. It can be seen that the accuracy of the parameter estimation deteriorates rapidly the deeper the layers. Below layer 5, the estimation is too poor to be acceptable for ε and δ. The estimation of δ is comparatively better than ε. As demonstrated in the previous sensitivity testing, theoretically, the shorter the offset, the better is the fitting of equation (5.1) with the non-hyperbolic traveltime curve; and therefore, the more accurate is the estimation of the anisotropy parameters. In practice, the traveltime variation is usually very small at the short offset. If the offset is too short, a tiny traveltime-picking-error will make the

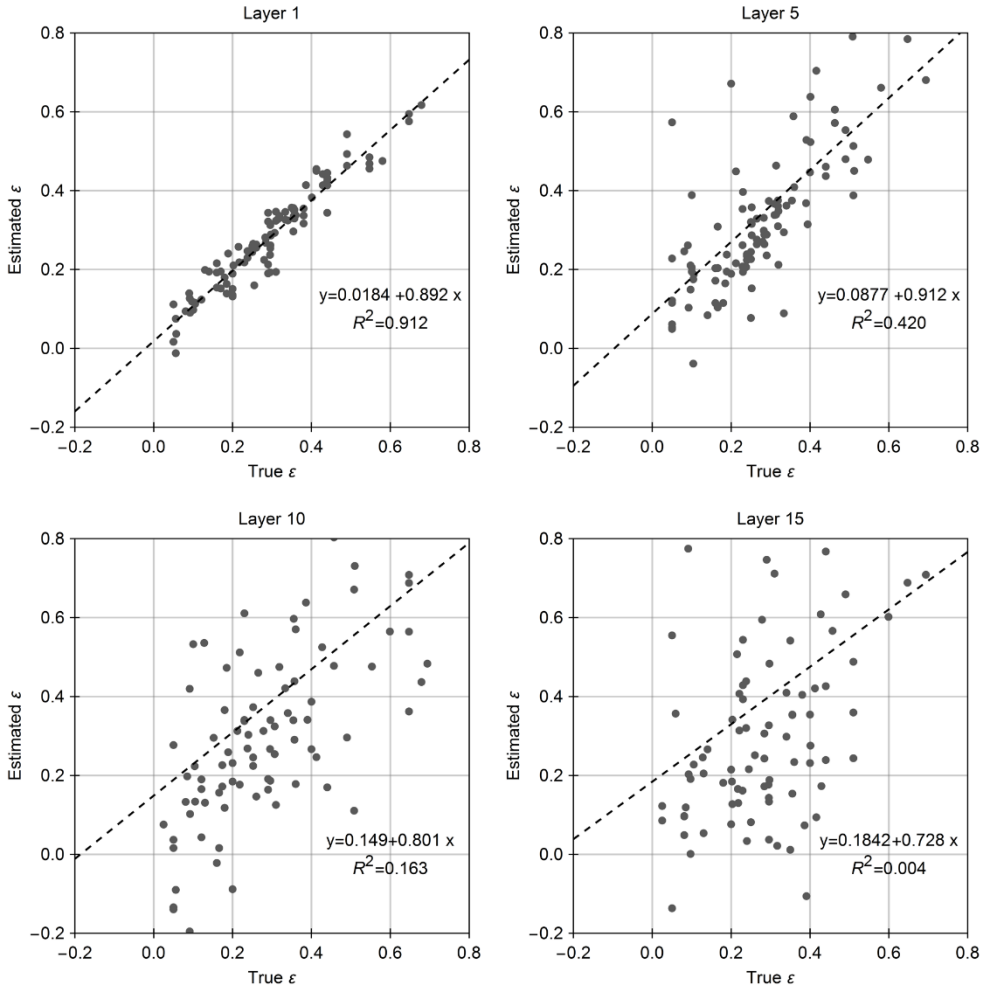

Figure 5.11 Uncertainty in the estimation of ε when there are errors in vertical velocity determination and traveltime picking. The maximum random error in determining V_{P0} is ±2% and the maximum random error in time picking is ±0.1%.

anisotropy-parameter estimation infeasible. Figure 5.13 shows the effect of offset on the estimation of Thomsen parameter ε for the top layer when the maximum shooting phase angle is 15°, 20°, 25°, and 30°, respectively. The accuracy in estimating ε decreases remarkably around the maximum shooting phase angle of 15°. Referring to the relation between the maximum shooting phase angle and the offset, as shown in

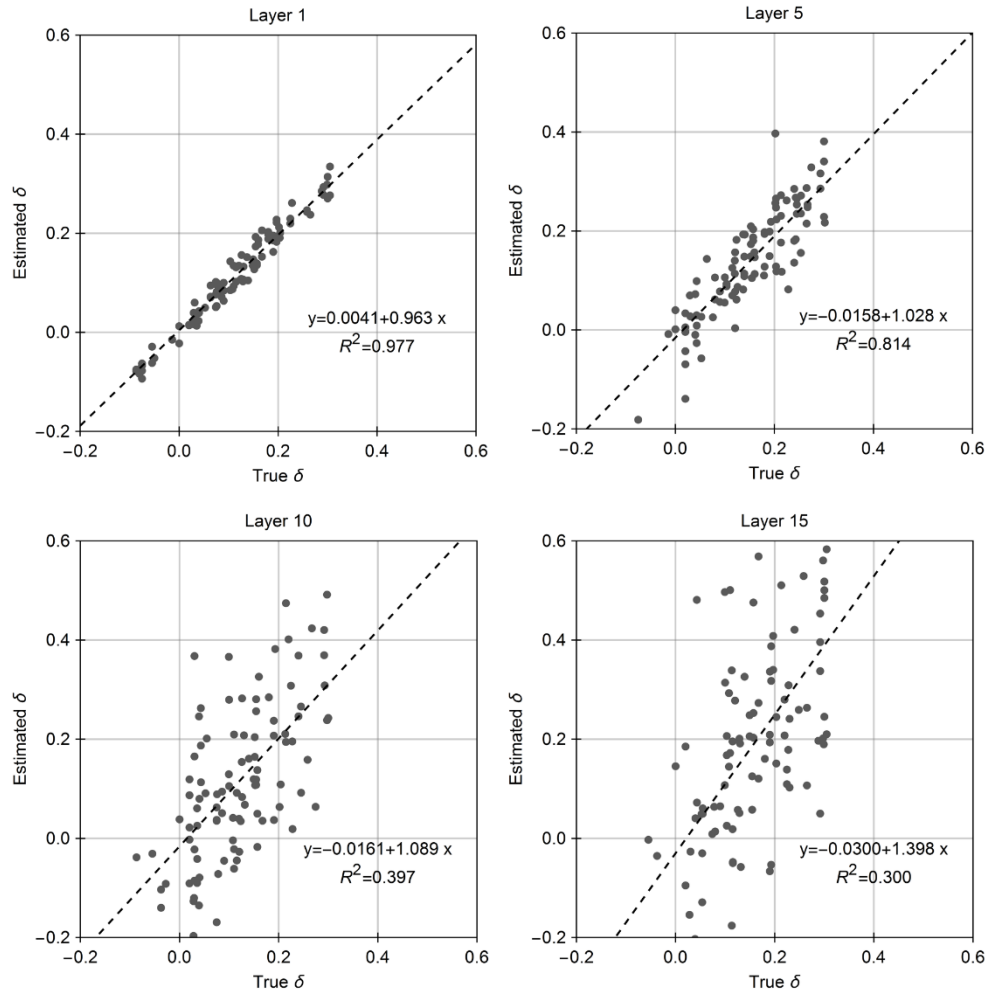

Figure 5.12 Uncertainty in the estimation of δ when there is an error in vertical velocity determination but no error in traveltime picking. The maximum random error in determining V_{P0} is ±2% for the top panel and ±5% for the bottom panel.

Figure 5.13, we suggest that the offset should be greater than the depth of the reflection event in practical applications.

5.9 Testing on a More Realistic Model

The previous experiments are all based on a layered TI model of shales with different strength of anisotropy. Sedimentary basins usually consist of formations of different

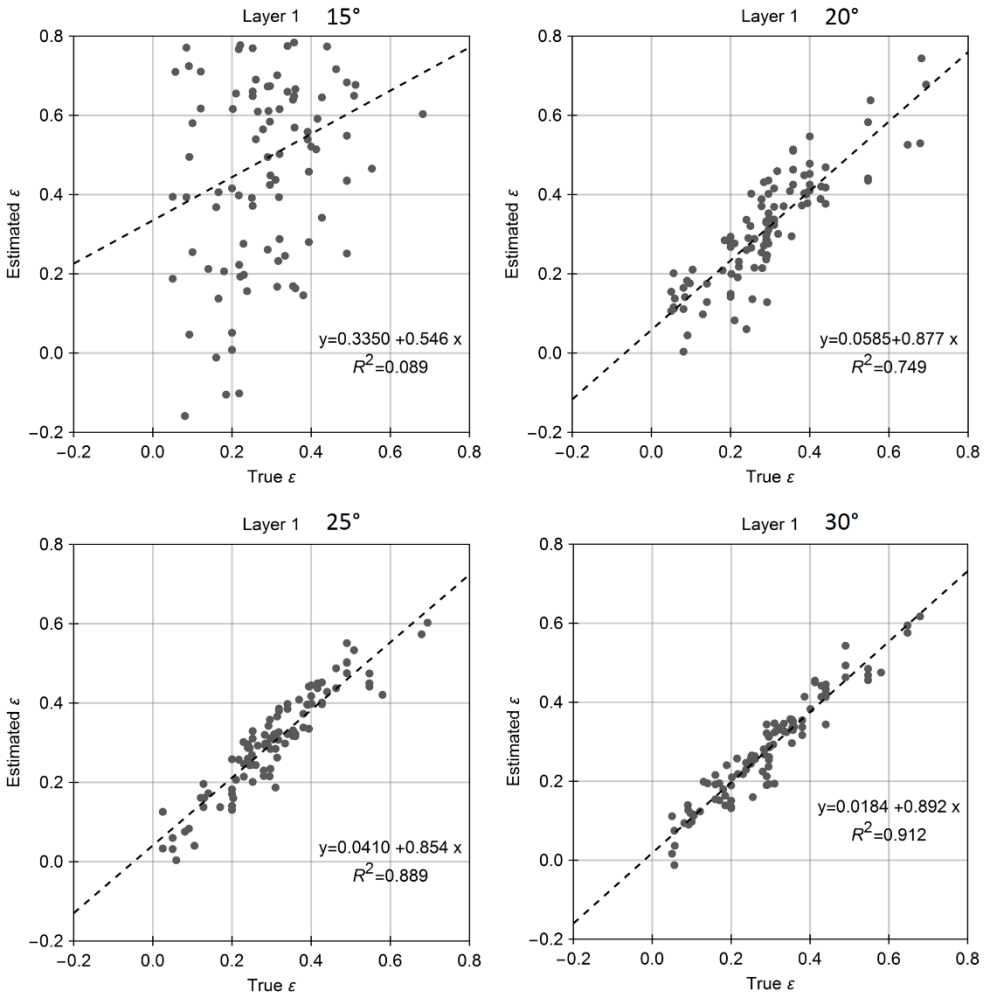

Figure 5.13 Effect of offset on estimation of ε when there are errors in vertical velocity determination and traveltime picking. The maximum random error in determining V_{P0} is ±2% and the maximum random error in traveltime picking is ±0.1%.

lithology due to variations of the depositional environment. Generally, seismic velocities of rocks increase with depth due to compaction and diagenesis.

To make the layered synthetic model geologically more realistic, we include a certain amount of laboratory ultrasonic-measurement data of sandstones from Gulf of Mexico

(Han, 1986). In total there are 144 data points (24 sandstone samples measured at different differential pressures). Figure 5.16 show the distribution of the vertical velocities of both the shales and the Gulf of Mexico sandstones. To parameterize the layered model, 15 data points are randomly selected from the dataset mixture of the shales and sandstones. Then the selected data points are sorted by the vertical P-wave velocity and assigned to 15 layers. For each testing, 200 simulations are run.

The synthetic model is now a mixture of isotropic sandstone layers and anisotropic shale layers. We first want to test the applicability of the anisotropy-parameter estimating procedure to this mixture model. In this experiment, no noises are added and

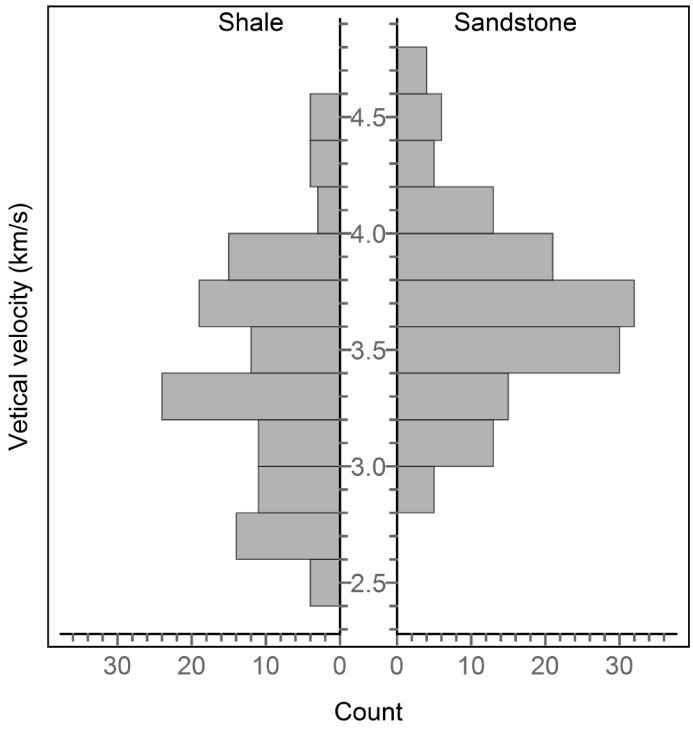

Figure 5.14 Distribution of vertical interval velocities for the shale and sandstone samples used for the synthetic layer-cake model. The sandstones samples are from Gulf of Mexico (Han, 1986).

the maximum shooting phase angle is 30°. Figure 5.15 shows the uncertainties in the estimation of ε and δ. It can be seen that the estimation of ε is excellent and the estimation of δ is perfect. Because isotropy can be treated as a special case of TI anisotropy with ε=0 and δ=0, the anisotropy-parameter estimating procedure works for both the isotropic sandstone layers and the anisotropic shale layers.

Next, we will test how the noises affect the estimation of the anisotropy parameters. The introduced noises are a random error between -2% to +2% for the vertical interval velocities and a random error between -0.1% to +0.1% for the two-way traveltime. The maximum shooting angle is 30°. Figures 5.16 and 5.17 show the estimation of the Thomsen parameter ε and δ, respectively. It can be seen the estimation accuracy deteriorates rapidly the deeper the layers. Below layer 5, the estimation is unacceptable. A tendency of over-estimation with the deeper layers is observed for Thomsen parameter ε. For the isotropic layers, the true values for both ε and δ are zero, but the distribution of the estimated values becomes wider for deeper layers. Therefore, in practical applications, it is quite possible that an isotropic formation can be misinterpreted as a strongly anisotropic formation. Since the randomly selected l5 layers are sorted by the vertical P-wave velocity, there is a selection preference of the rock samples for different layers. The estimation of δ is generally more reliable than the estimation of ε.

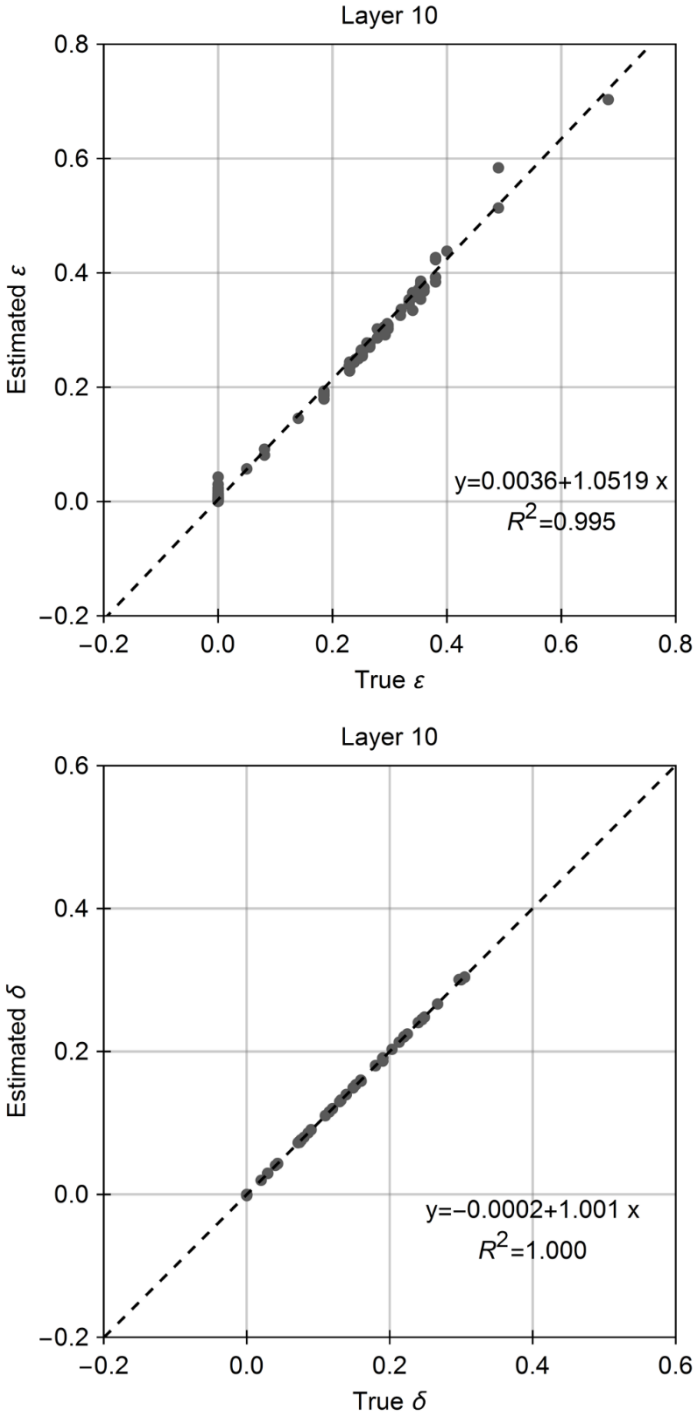

Figure 5.15 Uncertainties in the estimation of ε and δ based on a sand-shale layer-cake model. There are no error in vertical velocity determination and traveltime picking. The maximum shooting phase angle is 30°.

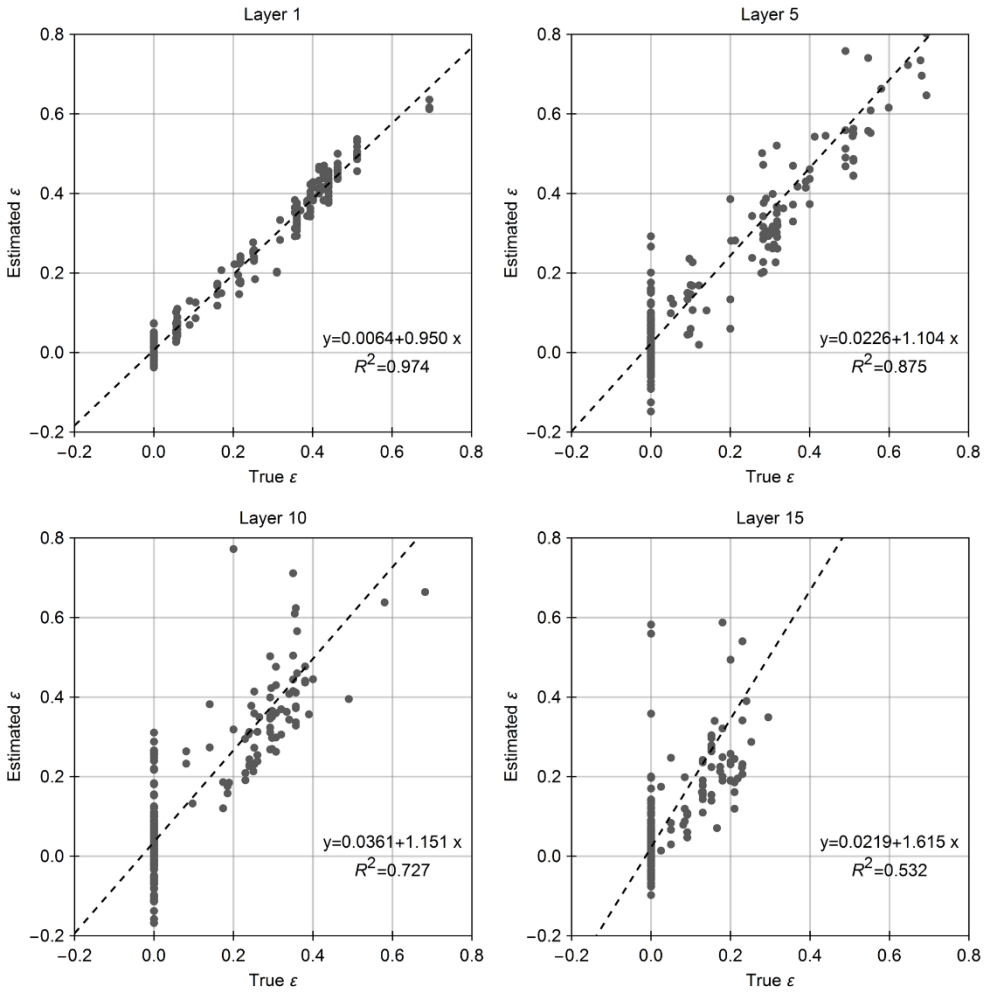

Figure 5.16 Uncertainty in the estimation of ε based on a sand-shale layer-cake model. The maximum random error in determining V_{P0} is ±2% and the maximum random error in time picking is ±0.1%. The maximum shooting phase angle is 30°.

5.10 Conclusions

The methodology for seismic anisotropy-parameter estimation developed by Alikahlifah and Tsvankin (1995) and Tsvankin (2012) is theoretically well-established. In general, δ can be more reliably estimated than ε and ε is more reliably estimated

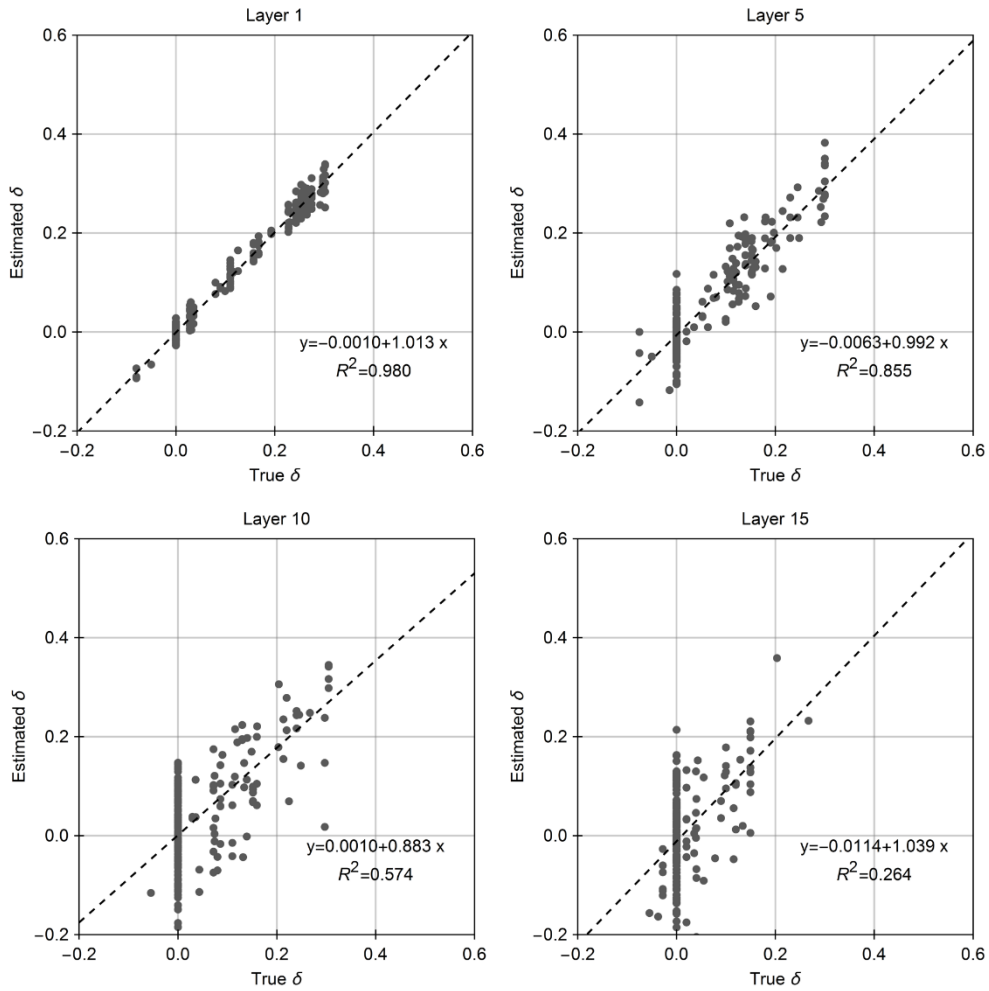

Figure 5.17 Uncertainty in the estimation of δ based on a sand-shale layer-cake model. The maximum random error in determining V_{P0} is ±2% and the maximum random error in time picking is ±0.1%. The maximum shooting phase angle is 30°.

than the anellipticity parameter η. Theoretically, the anisotropy parameters are more reliably estimated on the seismic data with shorter offset, but in practical applications the offset should be greater than the depth of the reflection event. This methodology is not sensitive to reasonable errors in vertical interval velocities, but it is extremely sensitive to the time-picking error. The uncertainty in anisotropy-parameter estimation

increases rapidly the deeper the layers, which may make this methodology infeasible for practical applications.

5.11 Acknowledgements

This study is supported by the Fluids and DHI consortium of the University of Houston and the Colorado School of Mine.

5.12 References

Alkhalifah T. and Tsvankin I. 1995. Velocity analysis for transversely isotropic media. *Geophysics* **60**, 1550-1566.

Alkhalifah T. 1997. Velocity analysis using nonhyperbolic moveout in transversely isotropic media. *Geophysics* **62**, 1839-1854.

Backus G.E. 1962. Long-wave elastic anisotropy produced by horizontal layering. *Journal of Geophysical Research* **67**, 4427-4440.

Baan M.V.D. and Kendall J.M. 2002. Estimating anisotropy parameters and traveltimes in the tau-p domain. *Geophysics* **67**, 1076–1086.

Blum T.E., Adam L. and van Wijk K. 2013. Noncontacting benchtop measurements of the elastic properties of shales. *Geophysics* **78**, C25-C31.

Byun B.S. 1984. Seismic parameters for transversely isotropic media. *Geophysics* **49**, 1908-1984.

Grechka V. and Tsvankin I. 1998. Feasibility of nonhyperbolic moveout inversion in transversely isotropic media. *Geophysics* **63**, 957-969.

Han D.-h. 1986. *Effects of Porosity and Clay Content on Acoustic Properties of Sandstones and Consolidated Sediments.* Ph.D. thesis, Stanford University.

Helbig K. and Thomsen L. 2005. 75-plus years of anisotropy in exploration and reservoir seismic: A historical review of concepts and methods. *Geophysics* **70**, 9ND-23ND.

Isaac J.H. and Lawton D.C. 2004. A practical method for estimating effective parameters of anisotropy from reflection seismic data. *Geophysics* **69**, 681–689.

Jakobsen M. and Johansen T.A. 2000. Anisotropic approximation for mudstones. A seismic laboratory study. *Geophysics* **65**, 1711-1725.

Johnston J.E. and Christensen N. I. 1995. Seismic anisotropy of shales. *Journal of Geophysical Research* **100**, 5591-6003.

Sarout J., Piane C.D., Nadri D., Esteban L. and Dewhurst D.N. 2015. A robust experimental determination of Thomsen's δ parameter. *Geophysics* **80**, A19-A24.

Slawinski M.A., Slawinski R.A., Brown R.J. and Parkin J.M., 2000. A general form of Snell's law in anisotropic media. *Geophysics* **65**, 632-637.

Sone H. 2012. *Mechanical Properties of Shale Gas Reservoir Rocks and Its Relation to In-situ Stress Variation Observed in Shale Gas Reservoirs*. Ph.D. thesis, Stanford University.

Sondergeld C.H. and Chandra S.R. 2011. Elastic anisotropy of shales. *The Leading Edge* **30**, 325-331.

Thomsen L. 1986. Weak elastic anisotropy. *Geophysics* **51**, 1954-1966.

Toldi J., Alkhalifah T., Berthet P., Arnaud J., Williamson P. and Conche B. 1999. Case study of estimation of anisotropy. *The Leading Edge* **18**, 588-594.

Tsvankin I. 2005. *Seismic Signatures and Analysis of Reflection Data in Anisotropic Media*, 2nd ed. Elsevier.

Tsvankin I. 2012. *Seismic Signatures and Analysis of Reflection Data in Anisotropic Media*, 3rd ed. SEG.

Vernik L. and Liu X. 1997. Velocity anisotropy in shales: A petrophysical study. *Geophysics* **62**, 521-532.

Wang X. and Tsvankin I. 2009. Estimation of interval anisotropy parameters using velocity-independent layer stripping. *Geophysics* **74**, WB117-WB127.

Wang Z. 2002. Seismic anisotropy in sedimentary rocks, part 2: Laboratory data. *Geophysics* **67**, 1423-1430.

White J.E., Martineau-Nicoletis L. and Monash C. 1983. Measured anisotropy in Pierre shale. *Geophysical Prospecting* **31**, 709–723.

Xiao C. 2006. *A Comparison of Different Methods for Estimating Thomsen's Anisotropy Parameters*. Ph.D thesis, University of Calgary.

Yan F., Han D.-h. and Yao Q. 2012. Oil shale anisotropy measurement and sensitivity analysis. *SEG Expanded Abstracts.*

Yan F., Han D.-h. and Yao Q. 2015. Physical constraints on c_{13} and δ for transversely isotropic hydrocarbon source rocks. *Geophysical Prospecting*, doi: 10.1111/1365-2478.12265

Chapter 6

Analysis of Seismic Anisotropy Parameters for Sedimentary Strata

6.1 Abstract

Based on a large quantity of laboratory ultrasonic-measurement data of sedimentary rocks and using Monte Carlo simulation and Backus averaging, the layering effect on seismic anisotropy is more realistically analyzed than in previous studies. The layering effect is studied for different types of rocks under different saturation conditions. If the sedimentary strata consist of only isotropic sedimentary layers and are brine saturated, the δ value for the effective TI medium is usually negative. However, the δ value will increase in gas bearing thin beds. Based on simulation results, c_{13} can be determined by other TI elastic constants for a layered medium consisting of isotropic layers. Therefore, δ can be predicted from the other Thomsen parameters with confidence. The theoretical expression of δ for an effective TI medium consisting of isotropic sedimentary rocks can be simplified with excellent accuracy into a neat form with a clear physical meaning.

6.2 Introduction

At various scales, the earth and the subsurface are often modeled as layered sequence of different constituents. Sedimentary strata are layered sedimentary rocks. Observed from the outcrops and seismic profiles, the most prominent feature of sedimentary basins is often its layered structure. The elastic properties of a layered medium can be described by transverse anisotropy and the properties are frequency dependent (Postma, 1955; Anderson, 1961; Backus, 1962; Helbig, 1984).

At the low-frequency limit, the effective anisotropic properties of two periodically alternating isotropic layers are described by Postma (1955). Backus (1962) extended the model to any combination of layers with either isotropic or transversely isotropic properties. Schoenberg and Muir (1989) further extended the Backus model to more general cases in which the constituent layers can be any type of anisotropic media. From the wireline logging data, the lithology or acoustic property variations of the sedimentary layers are often in the scale of decimeters, whereas the wavelength of the seismic wave are usually around 100 meters. Therefore, the effective media through which the seismic waves propagate are usually, more or less, anisotropic. Study of the effective anisotropic properties of the layered media is important for seismic exploration.

The importance of seismic anisotropy on seismic imaging and seismic data interpretation is well-understood (Alkhalifah and Tsvankin, 1995; Helbig and Thomsen, 2005), but consideration of seismic anisotropy also puts great challenges in seismic-data processing because extra parameters are introduced. In exploration geophysics,

the seismic anisotropic properties are conveniently defined by the Thomson parameters (Thomsen, 1986). Based on Backus averaging and Monte Carlo simulation of the layer-cake models for two and three layers, Berryman (1999) analyzed the relationships among the Thomsen parameters. Berryman's (1999) study showed little indication of correlations between the anisotropy parameters except for the possible range and sign of the parameters. The simulation results were not very helpful for understanding the seismic anisotropic properties of sedimentary rocks.

In Berryman's (1999) study, the elastic parameters for the layered model are assumed to have uniform distributions in certain ranges. This assumption may be far from true for the sedimentary rocks. In the first part of this study, a more realistic study will be performed using similar approaches by Berryman (1999), but the Monte Carlo simulation will be based on a large quantity of laboratory measurement data of sedimentary rocks. More constituent layers with either isotropic or transversely anisotropic properties are included to simulate the complexity of sedimentary strata.

6.3 Monte Carlo Simulation of Sedimentary Strata

In terms of volume fraction and lithology, the sedimentary formations primarily consist of mudstone, carbonate, and sandstone (Grotzinger and Jordan, 2010). The mudstone refers to clastic rocks with fine particles. The terms mudstone and shale are used in mixture and no distinction is made between them in this study. Carbonate and sandstone usually are very weak in elastic anisotropy and are assumed isotropic in this study. Shales are assumed intrinsically anisotropic by default. From observation of the wireline logging data, the noticeable acoustic velocity changes are often in the order of

tens of centimeters or less, whereas the velocities of seismic waves are determined by the effective properties of the formation unit with thickness of tens of meters. Therefore, to model the effective properties of the sedimentary layers, it would be more realistic to use multiple layers instead of two or three layers. For the wireline logging data, the S-wave velocity is often less reliable than the P-wave velocity information. It is very rare that the anisotropic parameters can be fully acquired from the wireline logging survey. Therefore, the logging data are usually not suitable for the up-scale study.

Instead, this study is based on a large amount of laboratory ultrasonic-measurement data of various sedimentary rocks. The sandstone data come from Han (1986). The sandstone samples in Han's dataset includes typical sandstones coming from various places all over the world. The samples have various clay content. They are measured at both dry and fully brine-saturated states and various pressure conditions. The carbonate rocks come from Rafavich et al. (1984), Kenter et al. (1997), Woodside et al. (1998), Assefa et al. (2003), and Fabricius et al. (2008). The carbonate samples in datasets by Rafavich et al.(1984), Assefa et al. (2003) and Fabricious et al. (2008) are measured in both dry and full brine saturated conditions. The shale data come from Thomsen (1986), Johnston and Christensen (1995), Vernik and Liu (1997), Jakobsen and Johansen (2000), Wang (2002, shale and coal samples only), and Sone (2012, 2013). Only data points with c_{13} lying within its physical bounds are included. The saturation conditions of shales are complicated and not classified for analysis. The data points for the dry sandstone are 420, for wet sandstones are 420, for dry carbonates are

144, for wet carbonates are 298 and for shales are 137. Figure 6.1 shows the probability density functions of α_0 and the ratio of α_0^2/β_0^2 of the experimental data of different types of rocks. Here α_0 and β_0 are the vertical P-wave velocity and S-wave velocity, respectively. The dry sandstone and wet sandstone are treated as different classifications of rocks because the effect of saturation on seismic anisotropy parameters is to be studied. It can be seen that the different classifications of rocks have different distributions of α_0 and ratios of α_0^2/β_0^2. Most of the distributions are close to normal with different central values. The carbonate rocks, dry or wet, have wider distribution of α_0. The shales have wider distribution of α_0^2/β_0^2 compared to other classifications of rocks. In Berryman's (1999) study only isotropic layers are considered. The Monte Carlo simulations are based on a uniform distribution of α_0 between 2.5 and 5.5 km/s and a uniform distribution of α_0^2/β_0^2 between 0.12 and 0.42. From Figure 6.1, it can be seen that the layer property parameterization in Berryman's (1999) study is not optimal for the sedimentary rocks.

In our study, sedimentary strata are simulated by first randomly selecting a certain number of samples from a classification of rocks or a combination of classifications of rocks, and then the experimental data of the selected samples are used to parameterize the layer-cake model. The elastic properties of each layer in the layer-cake model is based on laboratory measurement, not on random sampling in certain ranges, which may lose the physical relations between the elastic parameters for the sedimentary rocks. This is the basic difference between our study and the study by Berryman (1999). Considering the size of the database and the number of simulations, a 15-layer-cake

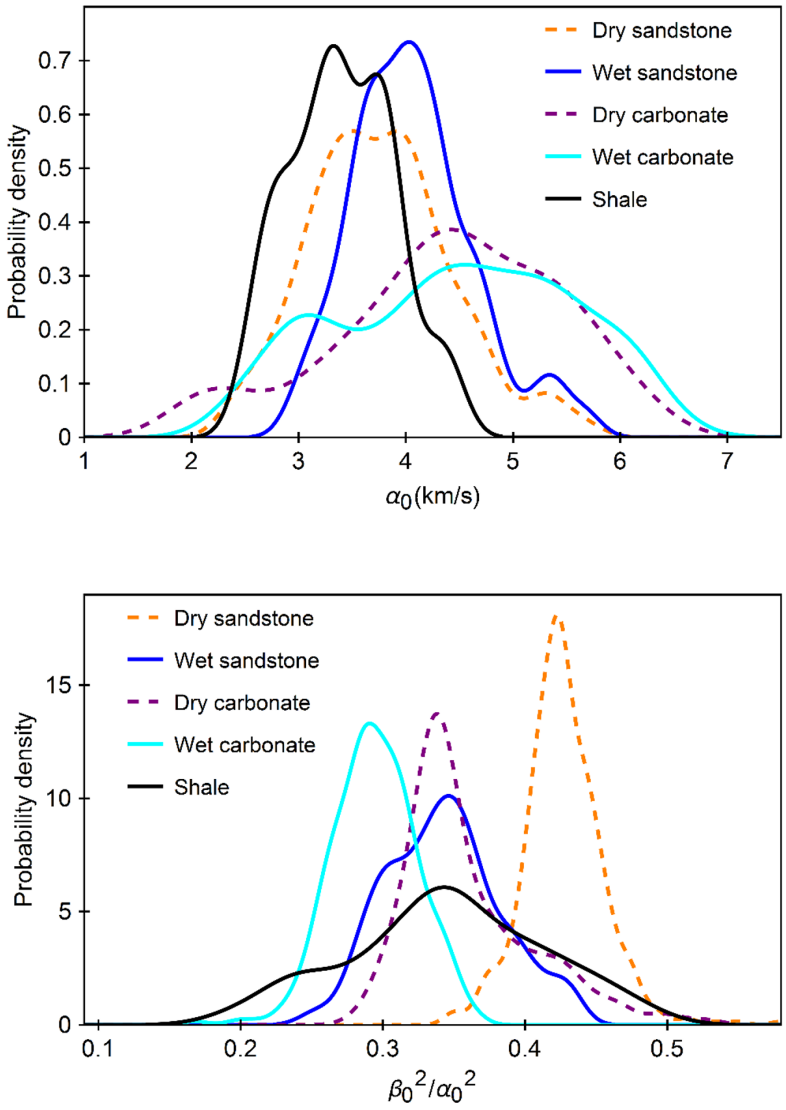

Figure 6.1 Probability densities of α_0 and β_0^2/α_0^2 of the laboratory data used in this study.

model is used. Compared to the 2- or 3-layer-cake model, the 15-layer-cake model may be more proper to simulate the complex subsurface conditions.

6.4 Backus Averaging

The effective elastic properties of a material consisting of fine layers with isotropic or transversely isotropic properties are transversely anisotropic. Backus (1962) brought up a model to estimate the effective anisotropic properties of a finely layered medium when the wavelength is much longer than the thicknesses of the individual layers. In the Voigt notation, the five effective TI elastic constants are computed by

$$c_{11B} = \langle c_{11} - \frac{{c_{13}}^2}{c_{33}} \rangle + \langle \frac{c_{13}}{c_{33}} \rangle^2 \langle {c_{33}}^{-1} \rangle^{-1}, \tag{6.1}$$

$$c_{13B} = \langle \frac{c_{13}}{c_{33}} \rangle \langle {c_{33}}^{-1} \rangle^{-1}, \tag{6.2}$$

$$c_{33B} = \langle {c_{33}}^{-1} \rangle^{-1}, \tag{6.3}$$

$$c_{44B} = \langle {c_{44}}^{-1} \rangle^{-1}, \tag{6.4}$$

$$c_{66B} = \langle c_{66} \rangle, \tag{6.5}$$

$$\rho_B = \langle \rho \rangle, \tag{6.6}$$

where $\langle * \rangle$ is a volume averaging operator. Equation (6.4) is actually the Reuss bound of c_{44} values of all the constituent layers. Equation (6.5) is the Voigt bound of c_{66} values of all the constituent layers. The subscript B in this study denotes that the effective property is estimated by the Backus averaging model. The Backus model is reduced to the Postma model (Postma, 1955) when the material consists of only two isotropic layers. The Schoenberg-Muir model (Schoenberg and Muir, 1989) extended the Backus model to a layered medium consisting of layers with arbitrary type of anisotropy. Since only isotropic or transversely isotropic layers are considered, the Backus averaging model is sufficient for this study.

6.5 Layering Effect on Seismic Anisotropy in Sedimentary Strata of a Single Lithology

Due to mild depositional environment changes, for the same type of rocks, the mineral composition and texture variation may also cause noticeable acoustic velocity change. The layering effect on seismic anisotropy may be different for different classifications of rocks. The effects are studied by Monte Carlo simulation and the Backus averaging. First, 15 samples are randomly selected from the experimental database for one of the five classifications of sedimentary rocks and the corresponding experimental data are used to parameterize the 15-layer-cake model. Then the Backus averaging is applied to estimate the effective anisotropic properties of the sedimentary strata. For simplicity, each layer has the same thickness. Since a sample can be repeatedly selected and samples with similar properties may be selected, variation of the layer thickness is actually simulated even an equal layer thickness model is used. For each classification of rocks, 5000 simulations are run.

Figures 6.2 to 6.4 show the simulation results of the layering effect on seismic anisotropy. In Figure 6.2, for all the classifications of rocks, the ratio α_0^2/β_0^2 is generally positively correlated with δ. Here the gray data points are for the stratified shale formation with each layer assumed isotropic with the vertical properties. It can be seen that the δ values are usually negative; after considering the intrinsic anisotropic properties of the shale layers, the δ values are usually positive. For the layer-cake models of wet sandstones and wet carbonates, the δ values are usually negative. The acoustic properties of the gas-bearing rocks should be between the wet rocks and dry

rocks but be generally more close to the dry rocks if the gas saturation is not too low. Therefore, qualitatively, gas saturation has an effect of increasing the δ value. Figure 6.3 shows the correlations between ε and δ for the five classifications of sedimentary rocks. It can be seen that for the wet sandstone and wet carbonate layers, ε is reversely correlated with δ, whereas for the dry carbonate rocks and shales, ε is positively correlated with δ. It is noticed that negative ε is not observed from 25, 000 simulations, which is quite different from Berryman's (1999) study. It is generally observed and accepted that the seismic velocity is greater along the bedding than in the perpendicular direction if the effect of fractures is not considered. The simulation results in this study should be more realistic.

Figure 6.4 shows the correlations between ε and γ. The relations between the P-wave anisotropy and S-wave anisotropy are different for different classifications of sedimentary rocks. Generally, the S-wave anisotropy is stronger than the P-wave anisotropy except for the gas-bearing carbonate layers. The ratio of S-wave to P-wave anisotropy will decrease due to the gas saturation effect. The ranges of P-wave and S-wave anisotropy for the carbonate layers are greater than the sandstone layers simply because the experimental data for the carbonate rocks have wider distributions of the acoustic properties, as can be seen from Figure 6.1. The rock samples for the experimental database come from different geological units and depths, variation of the acoustic properties shown in Figure 6.1 should be much stronger than the real subsurface scenarios when the sedimentary strata in a certain depth interval are considered. Therefore, for the real sedimentary strata, the layering effect on seismic

anisotropy should be much less significant than the simulation results, but the relationship between the P-wave anisotropy and S-wave anisotropy should still be true for different classifications of rocks.

6.6 Prediction of δ for Sedimentary Strata Consisting of Isotropic Layers

At the low-frequency limit, the layered media can be treated as an effective TI medium defined by five elastic constants: c_{11}, c_{33}, c_{44}, c_{66}, and c_{13}. The physical meanings of c_{11}, c_{33}, c_{44}, and c_{66} are straightforward and they can usually be reliably determined. The physical meaning of c_{13} is not obvious and there are often significant uncertainties in the laboratory determination of c_{13} (Yan et al., 2015). Therefore, it may be useful to find the correlation between c_{13} and other TI elastic constants.

Based on the previous simulation results, Figure 6.5 shows the correlation between c_{13} and other TI elastic constants. It can be seen that c_{13} can almost perfectly be predicted by other TI elastic constants. The correlation formula is

$$c_{13B} = -0.048 + 0.48\, c_{11B} + 0.46\, c_{33B} - 0.53\, c_{44B} - 1.27\, c_{66B}. \quad (6.7)$$

The elastic constants are in GPa and the regression coefficient is 0.999 based on 20000 simulations. Considering the different elastic properties between sandstone and carbonate, dry rocks and wet rocks, the quality of this correlation is out of expectation. Compared to the c_{13} values of common sedimentary rocks, the constant term in equation (6.7) is negligible. After dropping the constant term, using definitions of the Thomsen parameters, equation (6.7) can be converted to

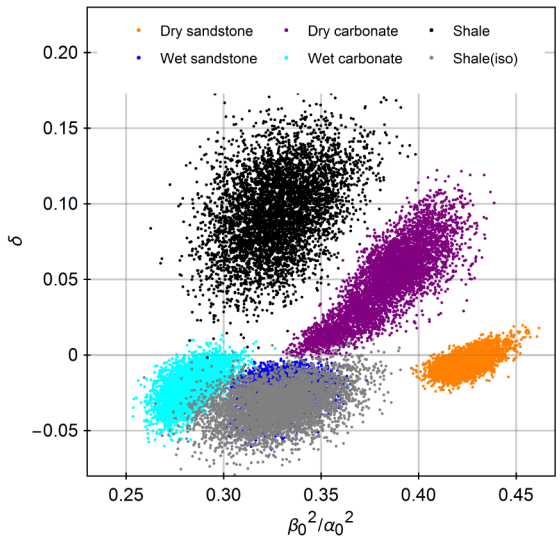

Figure 6.2 Crossplot between δ and β_0^2/α_0^2. δ and β_0^2/α_0^2 are computed from Backus averaging of a 15-layer-cake model randomly parameterized by the laboratory measurement data. Each cloud of points are from 5000 simulations. For the gray data points, the shale layer is assumed isotropic with the vertical properties.

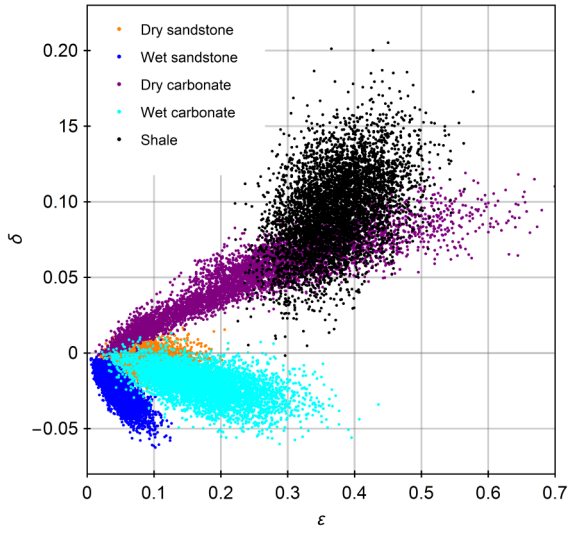

Figure 6.3 Crossplot between ε and δ. ε and δ are computed from Backus averaging of a 15-layer-cake model randomly parameterized by the laboratory measurement data. Each cloud of points are from 5000 simulations.

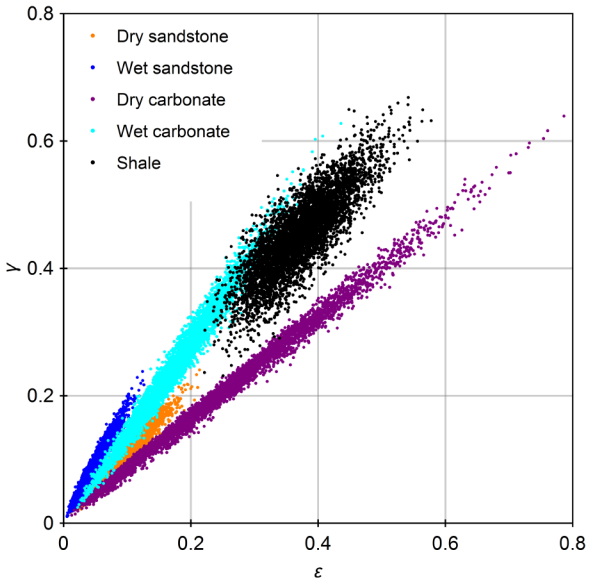

Figure 6.4 Crossplot between ε and γ. ε and γ are computed from Backus averaging of a 15-layer-cake model randomly parameterized by the laboratory measurement data. Each cloud of points are from 5000 simulations.

$$\delta = \frac{-(1-{r_0}^2)^2 + \left(0.455 + 0.466{r_0}^2 + 0.479(1+2\varepsilon_B) - 1.267{r_0}^2(1+2\gamma_B)\right)^2}{2(1-{r_0}^2)}, \tag{6.8}$$

where r_0 is the ratio of β_0/α_0.

Figure 6.6 shows a comparison between δ computed by the Backus averaging and δ predicted by equation (6.8). The result is consistent with the study in chapter 3 that δ can be predicted from the other Thomsen parameters. Figure 6.7 shows similar result as Figure 6.6, except that the sedimentary strata are simulated by random sampling of

the experimental database of dry or wet sandstones and dry or wet carbonate rocks. Each classification of rocks has equal chance to appear in the 15-layer-cake model.

Equation (6.8) only works for the sedimentary strata consisting of isotropic layers. As shown in Figure 6.8, if the shale layers with intrinsic anisotropy are included, equation (6.8) will not work and usually underestimates δ.

6.7 Approximation of δ for Sedimentary Strata Consisting of Isotropic Layers

δ is important for seismic-data processing because it determines the relation between the vertical interval velocity and the normal-moveout velocity. As Thomsen (1986) describes that δ is an "awkward" combination of the TI elastic constants and its physical meaning is ambiguous. From the Backus averaging of two and three isotropic layers, Berryman (1999) finds that

$$Sign(\delta_{B)} = Sign\left(\langle\alpha_0^{-2}\rangle - \langle\beta_0^{-2}\rangle\langle\frac{\beta_0^2}{\alpha_0^2}\rangle\right). \tag{6.9}$$

It would be nicer to rewrite the above equation in the following form,

$$Sign(\delta_{B)} = Sign\left(\frac{\langle\alpha_0^{-2}\rangle}{\langle\beta_0^{-2}\rangle} - \langle\frac{\beta_0^2}{\alpha_0^2}\rangle\right). \tag{6.10}$$

In this study, further exploration is made on the sign and the physical meaning of δ. From definition of δ,

$$\delta_B = \frac{(c_{13B} + c_{44B})^2 - (c_{33B} - c_{44B})^2}{2c_{33B}(c_{33B} - c_{44B})}. \tag{6.11}$$

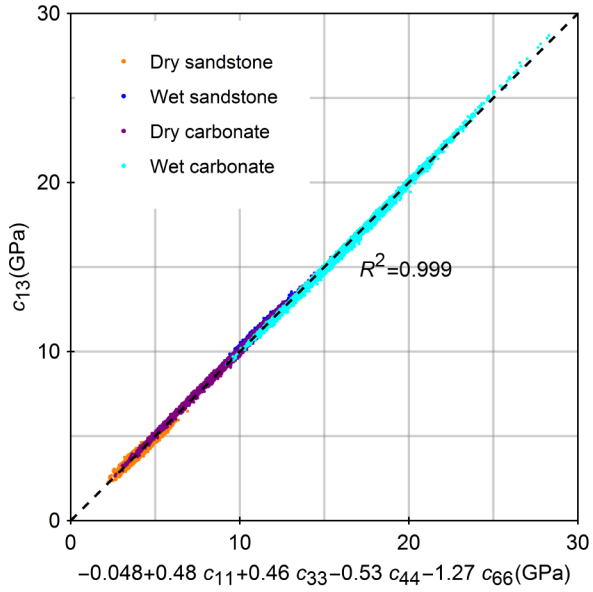

Figure 6.5 Relationship between c_{13} and other TI elastic constants based on Backus averaging of randomly selected 15-layer-cake model. 5000 simulations are run for each type of rocks.

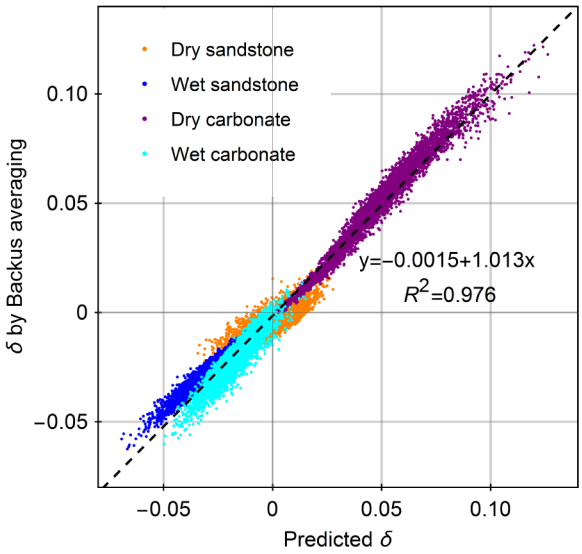

Figure 6.6 Prediction of δ from the other Thomsen parameters based on Backus averaging of randomly selected 15-layer-cake model.5000 simulations are run for each type of rocks.

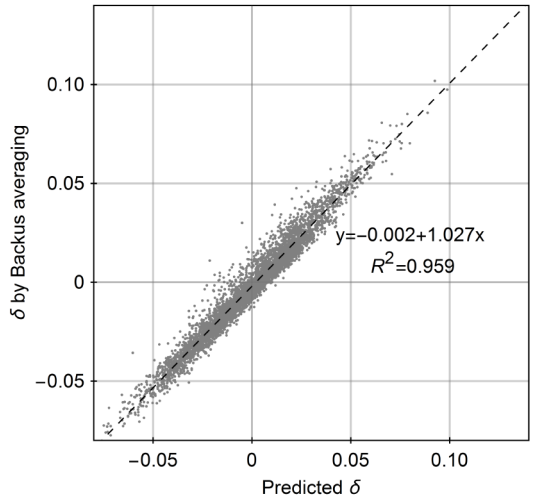

Figure 6.7 Prediction of δ from the other Thomsen parameters based on Backus averaging of a 15-layer-cake model. The elastic properties of the 15-layer-cake model are randomly selected from mixture of dry and wet sandstones, dry and wet carbonates, each classification of rocks has 25% chance to be selected. δ is predicted using equation (6.8).

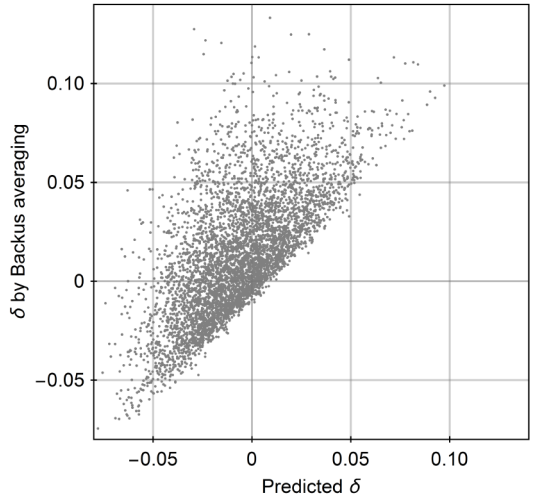

Figure 6.8 Prediction of δ from the other Thomsen parameters based on Backus averaging of a 15-layer-cake model. The elastic properties of the 15-layer-cake model are randomly selected from mixture of dry and wet sandstones, dry and

wet carbonates and shale, and each classification of rocks has 20% chance to be selected. δ is predicted using equation (6.8).

Substituting equations (6.2 to 6.4) into the above equation and making further algebraic manipulations, we have

$$\delta_B = 2\left(\frac{\langle c_{44}^{-1}\rangle^{-1}}{\langle c_{33}^{-1}\rangle^{-1}} - \langle\frac{c44}{c33}\rangle\right)\frac{1-\langle\frac{c44}{c33}\rangle}{1-\frac{\langle c_{44}^{-1}\rangle^{-1}}{\langle c_{33}^{-1}\rangle^{-1}}}. \tag{6.12}$$

Here $\langle c_{44}^{-1}\rangle^{-1}$ is the Reuss bound of the c_{44} values and $\langle c_{33}^{-1}\rangle^{-1}$ is the Reuss bound of the c_{33} values. The ratio should be less than one. It is obvious that the leftmost term in the above equation should always be positive for natural rocks; therefore,

$$Sign(\delta_B) = Sign\left(\frac{\langle c_{44}^{-1}\rangle^{-1}}{\langle c_{33}^{-1}\rangle^{-1}} - \langle\frac{c44}{c33}\rangle\right). \tag{6.13}$$

Equation (6.13) is a more accurate expression than equation (6.10) because there is no assumption of constant density. The sign of δ is determined by the difference between two types of c_{44}/c_{33} ratios by different approaches. One approach is to calculate the ratio of the Reuss bound of c_{44} to the Reuss bound of c_{33}. The other approach is to calculate the Voigt bound of the c_{44}/c_{33} ratios of the constituent layers.

From Monte Carlo simulation of the sedimentary strata consisting of isotropic layers, as shown in Figure 6.9, the ratio of $\left(1-\langle\frac{c44}{c33}\rangle\right)$ to $(1-\frac{\langle c_{44}^{-1}\rangle^{-1}}{\langle c_{33}^{-1}\rangle^{-1}})$ is generally very close to 1. Therefore, for the sedimentary strata consisting of isotropic layers, equation (6.12) can be simplified into

$$\delta \approx 2\left(\frac{\langle c44^{-1}\rangle^{-1}}{\langle c33^{-1}\rangle^{-1}} - \langle\frac{c44}{c33}\rangle\right). \quad (6.14)$$

Figure 6.10 shows a comparison between δ calculated by the Backus averaging and δ approximated by equation (6.14). The difference between the theoretical δ value and the approximated δ value is only noticeable at extremely low and high δ values.

6.8 Layering Effect on Seismic Anisotropy for Sedimentary Strata of Mixed Lithologies

Except for mild acoustic property change caused by the mineral composition and texture variation for the same type of sedimentary rocks, stronger acoustic property change in a sedimentary formation can be caused by a drastically depositional environment change that leads to lithology change. For example, the interbedding of shales with sandstones and the interbedding of shales with carbonate rocks are often-occurring geological scenarios. To model the interbedding effect on seismic anisotropy, the 15-layer-cake model is randomly parameterized by the experimental database of shales and the experimental database of one classification of the isotropic rocks. Of the 15 layers, each layer has equal chance to be the shale layer and layer of one classification of the isotropic rocks. For each combination of shale with the other classification of the isotropic rocks, 5000 simulations are run. The number of shale layers in the 15-layer-cake model should have a normal distribution with a central value around 7.5.

Figures 6.11 to 6.13 show the simulation results of the interbedding effect on seismic anisotropy parameters. Comparing Figures 6.2 to 6.4 with Figures 6.11 to 6.13, if we

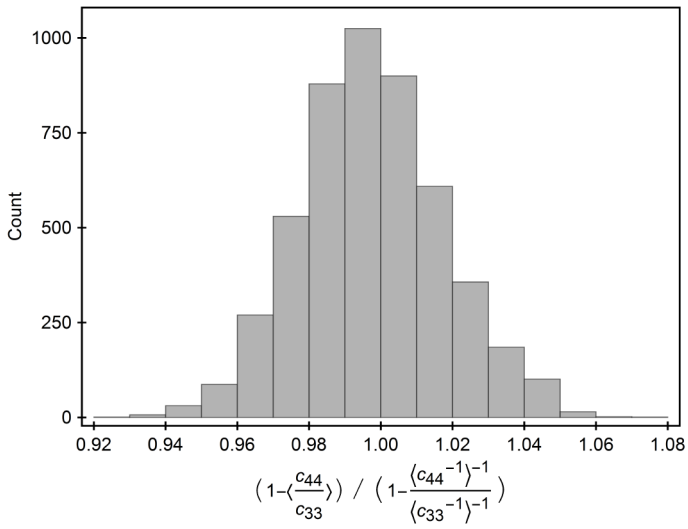

Figure 6.9 Distribution of $(1-\langle\frac{c_{44}}{c_{33}}\rangle)/(1-\frac{\langle {c_{44}}^{-1}\rangle^{-1}}{\langle {c_{33}}^{-1}\rangle^{-1}})$ from a 15-layer-cake model randomly selected from the laboratory data of dry or wet sandstones and dry or wet carbonates. Totally 5000 simulations are run.

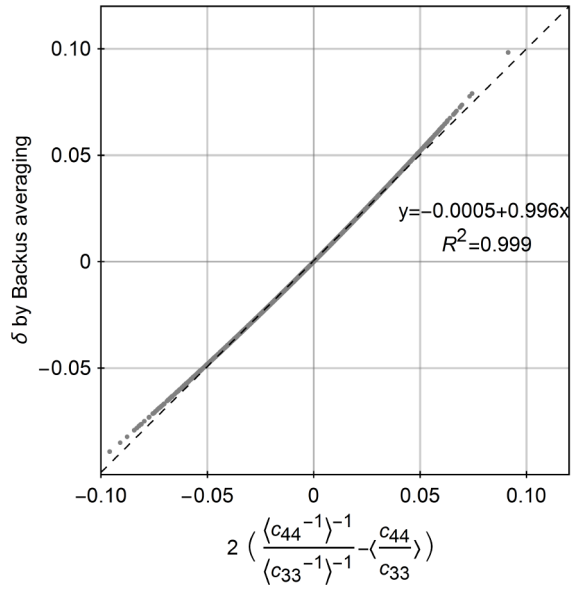

Figure 6.10 Prediction of δ by $2(\frac{\langle {c_{44}}^{-1}\rangle^{-1}}{\langle {c_{33}}^{-1}\rangle^{-1}}-\langle\frac{c_{44}}{c_{33}}\rangle)$ based on a 15-layer-cake model randomly selected from the laboratory data of dry or wet sandstones and dry or wet carbonates. Totally 5000 simulations are run.

know the layering effect on seismic anisotropy for each classification of the sedimentary rocks, the interbedding effect by two classifications of the sedimentary rocks on seismic anisotropy is generally predictable. In Figure 11, when the intrinsic anisotropy of shales is considered, the δ values are mostly positive. In Figure 6.12, generally, there is a fair correlation between ε and δ. It can be seen from Figure 6.13 that there is a good correlation between ε and γ. Shales are a type of rock with complicated mineral composition including clay minerals, quartz, carbonate, and organic materials. The interbedding effect on seismic anisotropy is in general consistent with the laboratory studies on shales (Sayers, 2005; Sondergeld and Chandra). Since the Monte Carlo simulation is based on the experimental data of real sedimentary rocks, the simulation results on the relationships among the seismic anisotropy parameters are quite different from those by Berryman's (1999) study.

6.9 Backus Averaging on Wireline Logging Data

The Backus averaging is often applied on the wireline logging data to upscale the logging data to a comparable scale of seismic data. In this study, the logging data from a tight gas reservoir area are used to illustrate the layering effect on seismic anisotropy and recognize possible issues of applying the Backus averaging to the logging data. The depth-sampling interval of the wireline logging data is 0.125 m. According to the experimental study by Marion et al. (1994), when the layer thickness is less than one tenth of the wavelength, effective properties of the layered medium are detected. If the seismic wavelength is assumed around 100 m, the layers within a depth interval around

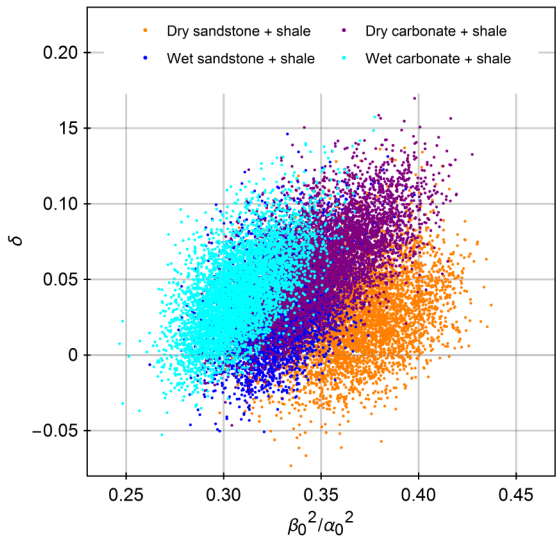

Figure 6.11 Crossplot between δ and β_0^2/α_0^2. δ and β_0^2/α_0^2 are computed from Backus averaging of 15-layer-cake model randomly parameterized by the laboratory measurement data. Each cloud of points are from 5000 simulations. Different colors represent mixture of shale with different classifications of rocks.

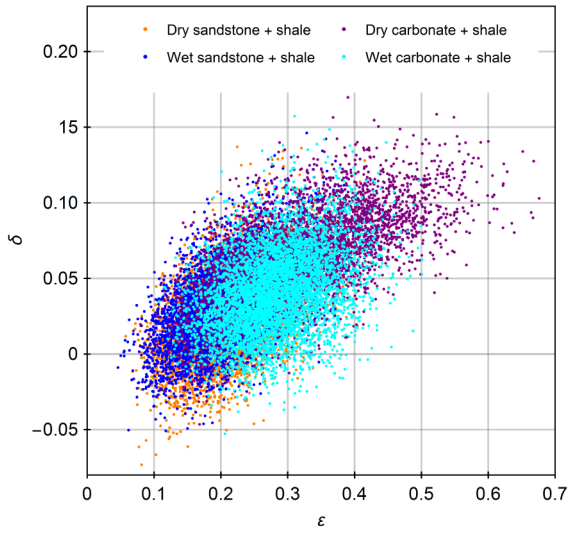

Figure 6.12 Crossplot between ε and δ. ε and δ are computed from Backus averaging of 15-layer-cake model randomly parameterized by the laboratory measurement data. Each cloud of points are from 5000 simulations. Different colors represent mixture of shale with different classifications of rocks.

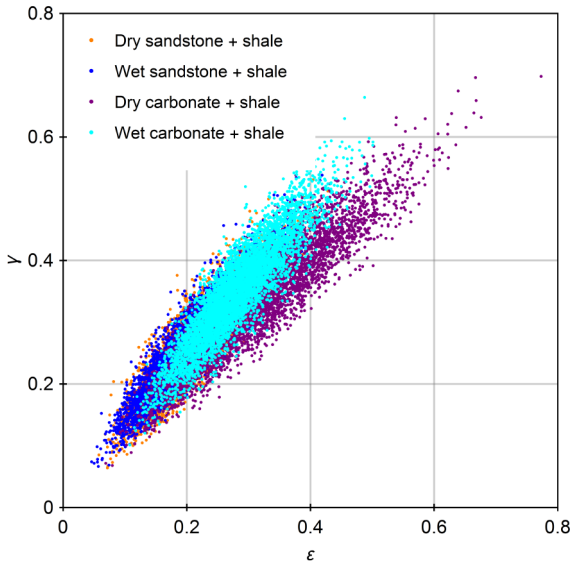

Figure 6.13 Crossplot between ε and γ. ε and γ are computed from Backus averaging of 15-layer-cake model randomly parameterized by the laboratory measurement data. Each cloud of points are from 5000 simulations. Different colors represent mixture of shale with different classifications of rocks.

10 m should be up-scaled. The moving Backus averaging is run for 80 data points from the top to the bottom of the logging data.

Figure 6.14 shows the correlation between α_0^2/β_0^2 and δ after Backus averaging is applied to the logging data. The color bar shows the saturation data, the fully saturated data points come from the shale formation, as can be seen from Figure 6.15. Since only the vertical properties are available from the wireline logging data, each layer is assumed isotropic with the vertical properties. Comparing Figure 6.14 and Figure 6.2, they are generally consistent, but the positions of the tight-gas sandstone data points are also determined by variation of the layer properties. It can be seen that there are less acoustic property variations in the sandstone formations, so that the δ value should

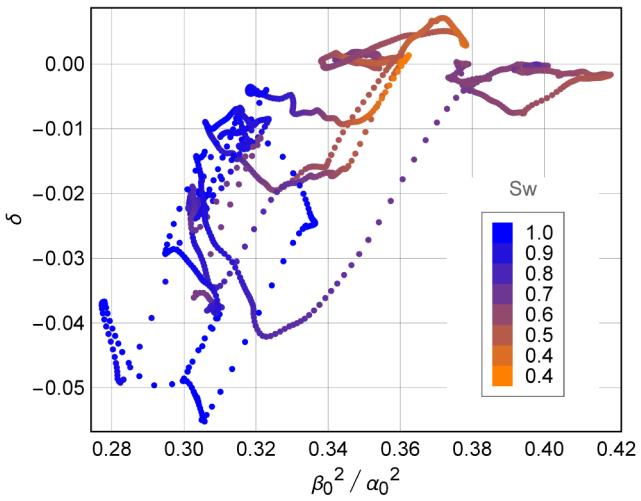

Figure 6.14 Crossplot between δ and β_0^2/α_0^2. δ and β_0^2/α_0^2 are computed from 100-data-point (12.5 m) Backus averaging of wire logging data from a tight gas sandstone reservoir. The shaly formations are assumed isotropic with the vertical properties.

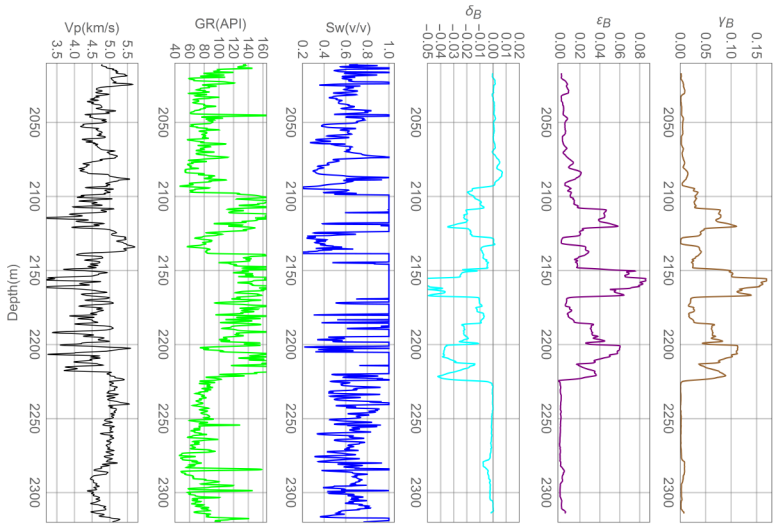

Figure 6.15 100-data-point (12.5 m) Backus averaging of wire logging data from a tight gas sandstone reservoir. The log curves in the left three column are original without applications of Backus averaging. The anisotropy log curves are computed by moving Backus average. The shaly formations are assumed isotropic with the vertical properties.

be close to zero. In Figure 6.15, the interbedding intervals have noticeable seismic anisotropy, even shales are assumed isotropic. It can be seen that the S-wave anisotropy is stronger than the P-wave anisotropy, which is consistent with the previous simulation study, but the real P-wave anisotropy and S-wave anisotropy should be stronger when the intrinsic anisotropy of shales is considered. The corresponding δ values are negative when shales are assumed isotropic. If the intrinsic anisotropic of shales is considered, the δ values should be close to zero or positive. Therefore, the interbedding effect on seismic anisotropy is very difficult to be modeled from the wireline logging data.

6.10 Conclusions

Based on a large amount of Monte Carlo simulation of sedimentary strata and Backus averaging using the laboratory database, it is found that the δ value for the sedimentary strata consisting of isotropic wet sandstones or carbonates is usually negative and the gas-bearing thin beds have an effect of increasing the δ value. When intrinsic anisotropy of shales is considered, the δ value is usually positive. For the sedimentary strata consisting of isotropic layers, the TI elastic c_{13} can be determined by other TI elastic constants and δ can be predicted from the other Thomsen parameters with confidence. A simplified expression of δ with clear physical meaning is derived for an effective TI medium consisting of isotropic layers.

6.11 Acknowledgements

We would like to thank the Fluid and DHI consortium sponsors for the financial support.

6.12 References

Alkhalifah T. and Tsvankin I. 1995. Velocity analysis for transversely isotropic media. *Geophysics* **60**, 1550-1566.

Anderson D.L. 1961. Elastic wave propagation in layered anisotropic media. *Journal of Geophysical Research* **66**, 2953-2963.

Assefa S., McCann C., and Southcott J. 2003. Velocities of compressional and shear waves in limestones. *Geophysical Prospecting* **51**, 1-13.

Backus G.E. 1962. Long-wave elastic anisotropy produced by horizontal layering. *Journal of Geophysical Research* **67**, 4427-4440.

Berryman J.G. 1999. Analysis of Thomsen parameters for finely layered VTI media. *Geophysical Prospecting* **47**, 959-978.

Fabricius I., Gommesen L., Krogsboll A., and Olsen D. 2008. Chalk porosity and sonic velocity versus burial depth: Influence of fluid pressure hydrocarbons and mineralogy: *The American Association of Petroleum Geologists Bulletin* **92**, 201-223.

Grotzinger J. and Jordan T.H. 2010. *Understanding Earth*, 6-th edition, W.H. Freeman.

Han D.-h. 1986. *Effects of Porosity and Clay Content on Acoustic Properties of Sandstones and Consolidated Sediments*. Ph.D. thesis, Stanford University.

Helbig K. 1984. Anisotropy and dispersion in periodically layered media. *Geophysics* **49**, 364-373.

Helbig K. and Thomsen L. 2005. 75-plus years of anisotropy in exploration and reservoir seismic: A historical review of concepts and methods. *Geophysics* **70**, 9ND-23ND.

Jakobsen M. and Johansen T.A. 2000. Anisotropic approximation for mudrocks: A seismic laboratory study. *Geophysics* **65**, 1711-1725.

Johnston, J.E. and Christensen N. I. 1995. Seismic anisotropy of shales. *Journal of Geophysical Research* **100**, 5591-6003.

Kenter J, Podladchikov F., Reinders M., van der Gaast S., Fouke B., and Sonnenfeld M. 1997. Parameters controlling sonic velocities in a mixed carbonate–siliciclastic Permian shelf-margin (upper San Andres Formation, Last Chance Canyon, New Mexico). *Geophysics* **62**, 505-520.

Marion D., Mukerji T. and Mavko G. 1994. Scale effects of velocity dispersion: From ray to effective medium theories in stratified media. *Geophysics* **59**, 1613-1619.

Postma G.W. 1955. Wave propagation in a stratified medium. *Geophysics* **20**, 780-806.

Rafavich F., Kendall C., and Todd T. 1984. The relationship between properties and the petrographic character of carbonate rocks. *Geophysics*, **49**, 1622-1636.

Sayers C.M. 2005. Seismic anisotropy of shales. *Geophysical Prospecting* **53**, 667-676.

Schoenberg M. and Muir F. 1989. A calculus for finely layered anisotropic media. *Geophysics* **54**, 581-589.

Sondergeld C.H. and Chandra S.R. 2011. Elastic anisotropy of shales. *The Leading Edge* **30**, 325-331.

Sone H. 2012. *Mechanical Properties of Shale Gas Reservoir Rocks and Its Relation to In-situ Stress Variation Observed in Shale Gas Reservoirs*, Ph.D. thesis, Stanford University.

Thomsen L. 1986. Weak elastic anisotropy. *Geophysics* **51**, 1954-1966.

Vernik L. and Liu X. 1997. Velocity anisotropy in shales: A petrophysical study. *Geophysics* **62**, 521-532.

Wang, Z. 2002. Seismic anisotropy in sedimentary rocks, part 2: Laboratory data. *Geophysics* **67**, 1423-1430.

Woodside, J., Kenter J., and Köhnen A. 1998. Acoustic properties from logs and discrete measurements (sites 966 and 967) on Eratosthenes Seamount: controls and ground truth, in *Proceedings of the Ocean Drilling Program: Scientific Results*, **160**, 535-543.

Yan F., Han D.-h. and Yao Q. 2015. Physical constraints on c_{13} and δ for transversely isotropic hydrocarbon source rocks. *Geophysical Prospecting*, doi: 10.1111/1365-2478.12265

Chapter 7

Comparison of Seismic Anisotropy of Sedimentary Strata at the Low- and High-frequency Limits

7.1 Abstract

The layer-induced seismic anisotropy of sedimentary strata is frequency dependent. At the low-frequency limit, the effective anisotropic properties of the layered media are estimated by the Backus averaging model. At the high-frequency limit, the apparent anisotropic properties of the layered media can be estimated by ray theory. Based on Monte Carlo simulation of the layered media using the laboratory ultrasonic-measurement database, the layering effects on seismic anisotropy at the high-frequency limit are compared with those at the low-frequency limit. Relative to the Backus averaging, ray theory usually underestimates the Thomsen parameters ε and γ, and overestimates δ. For an effective layered medium consisting of isotropic sedimentary rocks, the differences are very significant. These differences decrease when shales with intrinsic anisotropy are included.

7.2 Introduction

Sedimentary strata consist of layered sedimentary rocks. Observed from the outcrops and seismic profiles, the most prominent feature of sedimentary basins is often its layered structure. The elastic properties of a layered medium can be described by transverse anisotropy and the properties are frequency dependent (Postma, 1955; Anderson, 1961; Backus, 1962; Helbig, 1984).

The frequency effect on seismic velocities in a layered medium was experimentally studied by Marion and Nur (1994). Significant velocity variations are observed when the layer thicknesses are around one tenth of the wavelength. The experimental results are theoretically interpreted by Hovem (1995). The studies only show the frequency dependence of seismic velocities in the direction of the TI symmetry axis. The low-frequency limit and high-frequency limit of seismic velocities in the TI symmetry axis are represented by the Backus averaging and the Wyllie time-averaging (or ray theory), respectively (Stovas and Bjorn Ursin, 2007). Extra assumptions are usually needed to solve the frequency effect on the elastic anisotropic properties in the non-oblique directions. The assumptions include infinite periodic layers and a plane harmonic wave (Helbig, 1984; Shapiro, 1994; Potel et al., 1995; Wang and Rokhlin, 2002). These assumptions may not be proper for seismic exploration of sedimentary basins.

At the high-frequency limit, the equivalent or apparent seismic properties of a layered medium should be transversely isotropic because it is obvious that seismic velocities are azimuthally independent in the bedding plane and only dependent on the incident angle. Seismic ray theory describes the high-frequency limit of acoustic wave

propagation in heterogeneous media. Seismic velocity-analysis is based on the ray theory. The seismic anisotropy parameters can be estimated from seismic data using similar procedure of velocity-analysis that is often applied under the assumption of an isotropic layer-cake model (Alkhalifah and Tsvankin, 1995; Alkhalifah, 1997; Tsvankin, 2005; Tsvankin, 2012). Silva and Stovas (2006) compared the equivalent anisotropic properties of an isotropic layer-cake model estimated by the Backus averaging and ray theory, respectively. The layer-cake model consists of two isotropic layers with given elastic properties. The study is quite limited due to an over-simplified model and lack of freedom in parameterization of the layer properties.

The vertical property variations of a sedimentary formation are usually more complicated than the two-layer-cake model and some sedimentary layers may be intrinsically anisotropic. In this study, Monte Carlo simulation will be applied to simulate more realistic geological formation variations. Then the Backus averaging and ray theory will be applied to observe the differences in the anisotropic properties.

7.3 Frequency Limits of the Layering Effect on Seismic Anisotropy

The study in the last chapter models the layering effect on seismic anisotropy at the low-frequency limit using the Backus averaging. The laboratory anisotropy-measurement usually uses ultrasonic waves of around 1 MHz, which is much higher than the central frequency of seismic data. Ray theory describes wave propagation at the high-frequency limit. Due to its simplicity, ray theory is often applied in seismic-data processing for velocity analysis and travel-time field computation. Therefore, it is

important to study the layering effect on seismic anisotropy at the high-frequency limit and compare it with the layering effect at the low-frequency limit.

To compute the equivalent anisotropy parameters at the high-frequency limit, the approach introduced in Chapter 6 for seismic anisotropy-parameter estimation is used. From the study in the last chapter, using the methodology by Alkhalifah and Tsvankin (1995) and Tsvankin (2012), it is shown that the anisotropy parameters can be perfectly inverted for the constituent layers when noises are not introduced. If all the constituent layers are treated as a unit, equation (5.1) can be used to invert the equivalent properties of the layered media as a whole. The slowness wavefront of the SH-wave is elliptic; therefore, equation (5.1) can be easily adapted for shear wave anisotropy-parameter estimation:

$$t^2(x) = {t_0}^2 + \frac{x^2}{V^2_{\mathrm{SHnmo}}}. \tag{7.1}$$

For SH-wave in a TI medium,

$$V_{SHnmo} = V_{SH90} = V_{SH0}\sqrt{(1+2\gamma)}\,, \tag{7.2}$$

where V_{SH0} is the shear wave velocity in the vertical direction and it is computed by ray theory. Therefore, all the anisotropy parameters and TI elastic constants can be inverted from velocity analysis on the synthetic-seismic data produced from the layer-cake model.

A 15-layer-cake model is used and parameterization of the layer properties is based on the same experimental database used in Chapter 6. Because a large amount computation is needed for ray tracing, conversions between the group velocity and the phase velocity, the group angle and the phase angle at each layer interface, and multiple parameter nonlinear regression, only 1000 simulations are run for each testing. The procedure of Monte Carlo simulation of the sedimentary strata is the same as used in studying of the layering effecting at the low-frequency limit. Similarly, the simulation analysis is first applied for each classification of the sedimentary rocks.

Figures 7.1-7.4 show the comparisons of the layering effects on seismic anisotropy at the low-frequency limit and high-frequency limit for each classification of rocks. In Figure 7.1, compared to the Backus averaging, the P-wave anisotropy parameter ε is slightly underestimated for the shale layers, and it is significantly underestimated for the sedimentary strata consisting of isotropic layers. For the sandstone and wet carbonate layers, ε estimated by ray theory is less than half of that estimated by the Backus averaging; for the dry carbonate layers, ε estimated by ray theory is less than 1/3 of that estimated by the Backus averaging. Compared to the estimation of ε, the S-wave anisotropy parameter γ is significantly underestimated by ray theory relative to the Backus averaging. In Figure 7.2, for the sedimentary strata consisting of isotropic layers, γ estimated by ray theory is only about 1/5 of that estimated by the Backus averaging.

In Figures 7.1 and 7.2, the ratio between the anisotropy parameters estimated by the Backus averaging and ray theory has little variation for the same classification of sedimentary rocks. Considering the compaction and diagenesis trend, random sampling from the experimental database may overestimates the elastic property variation of sedimentary strata. The high ε or γ values for some simulations can rarely happen in the real subsurface conditions. For the real sedimentary strata consisting of isotropic sedimentary rocks, the magnitude of ε or γ of may be much less than the simulation results, but the ratio between the anisotropy parameters estimated by the Backus averaging and ray theory should be same as the simulation results. Therefore, the simulation study still provide meaningful information.

Figure 7.3 shows a comparison of estimating δ by the Backus averaging and ray theory. Except for the dry carbonate layers, the δ values estimated by ray theory are generally greater than those estimated by the Backus averaging. The δ values estimated by the Backus averaging for wet sandstone layers and wet carbonate layers are usually negative, but it is shown that the δ values estimated by ray theory are always positive. If ε and δ are known, the anellipticity parameter η is a redundant parameter, but this parameter is still important for its physical meaning in determining the relation between the normal-moveout velocity and the horizontal velocity. In Figure 7.4, η estimated by ray theory is much lower than estimated by the Backus averaging, and it is similar to the case of estimating ε.

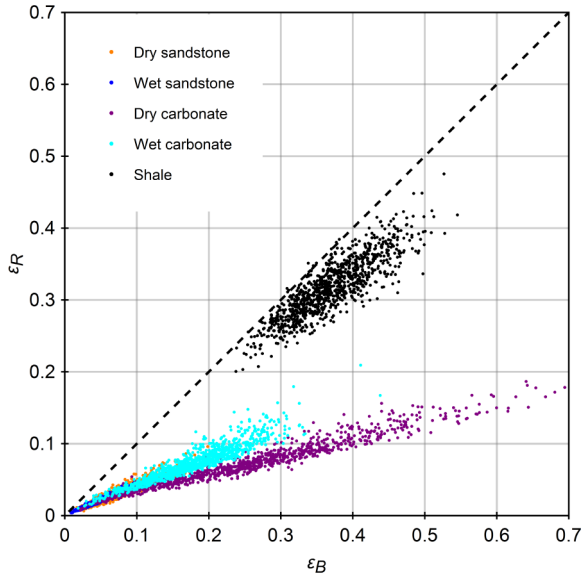

Figure 7.1 Comparison of ε estimated by the Backus averaging and ray theory for different classifications of rocks. 1000 simulations are run for each types of rocks. The subscript "B" denotes Backus averaging and "R" denotes ray theory in this study.

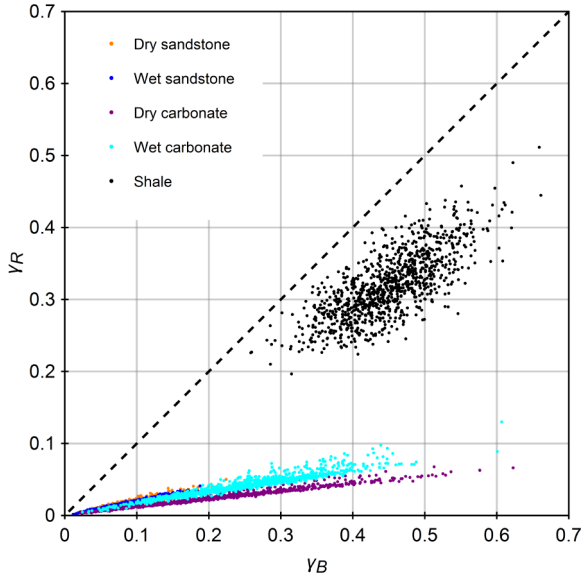

Figure 7.2 Comparison of γ estimated by the Backus averaging and ray theory for different classifications of rocks. 1000 simulations are run for each types of rocks.

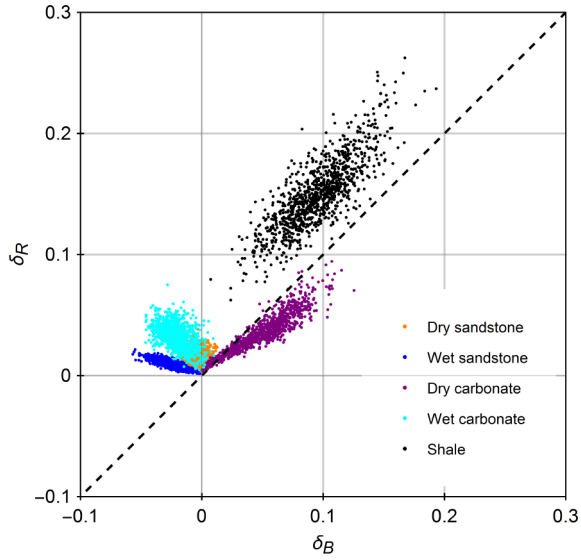

Figure 7.3 Comparison of δ estimated by the Backus averaging and ray theory for different classifications of rocks. 1000 simulations are run for each type of rocks.

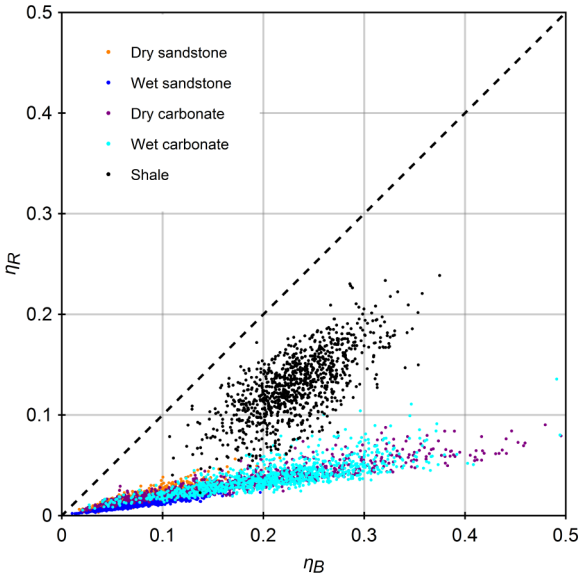

Figure 7.4 Comparison of η estimated by the Backus averaging and ray theory for different classifications of rocks. 1000 simulations are run for each type of rocks.

7.4 Frequency Limits of the Layering Effect on the TI Elastic Constants

To have better understanding of the differences of the Thomsen parameters estimated by the Backus averaging and ray theory, it may be more instructive to compare the differences in estimating the TI elastic constants. Figures 7.5 to 7.9 shows the comparisons of the estimated TI elastic constants by the Backus averaging and ray theory, respectively. In Figure 7.5, c_{11} estimated by ray theory is in general slightly less than estimated by the Backus averaging, which means that there is usually no significant difference in the estimated horizontal P-wave velocities by ray theory and the Backus averaging. In Figure 7.6, c_{33} estimated by ray theory is always higher than estimated by the Backus averaging because c_{33} estimated by the Backus averaging is the Reuss lower bound. The difference is determined by the difference between the Wyllie time-average and the Reuss bound. For sandstone and shale layers, the difference in estimated c_{33} values is small; the difference is more noticeable for the carbonate layers. According to the definition of the Thomsen parameter, $\varepsilon = (c_{11} - c_{33})/(2c_{33})$, underestimation of c_{11}, overestimation of c_{33}, which is also in the denominator term, will all cause the estimated ε by ray theory to be much smaller relative to that estimated by the Backus averaging. Comparing Figure 7.7 and Figure 7.6, the case of estimating c_{44} is similar to that of estimating c_{33}. Figure 7.8 shows a comparison of c_{66} estimated by the Backus averaging and ray theory. Compared to Figure 7.5, the difference in estimating c_{66} is much greater than the difference in estimating c_{11} by the two different approaches. One possible explanation is that c_{66} estimated by the Backus averaging is the Voigt high bound; whereas c_{11} estimated by

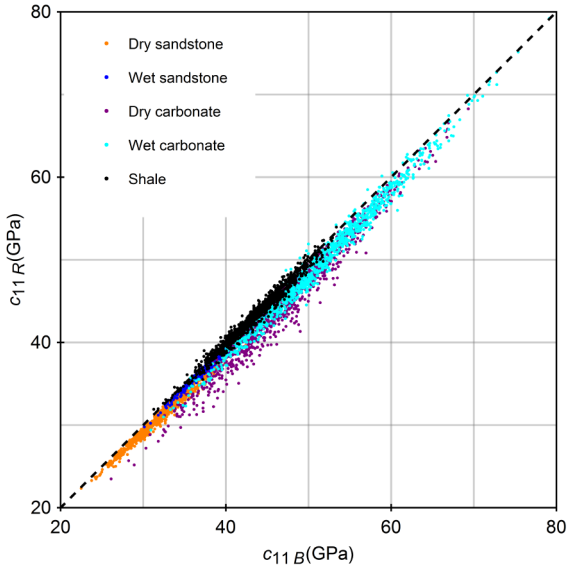

Figure 7.5 Comparison of c_{11} estimated by the Backus averaging and ray theory for different classifications of rocks. 1000 simulations are run for each types of rocks.

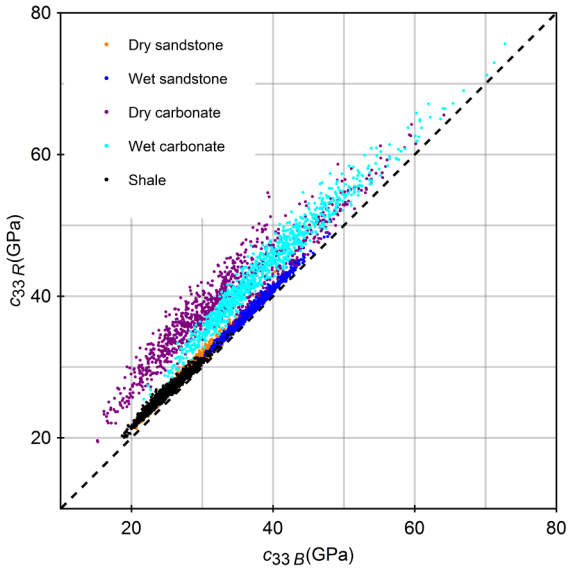

Figure 7.6 Comparison of c_{33} estimated by the Backus averaging and ray theory for different classifications of rocks. 1000 simulations are run for each types of rocks.

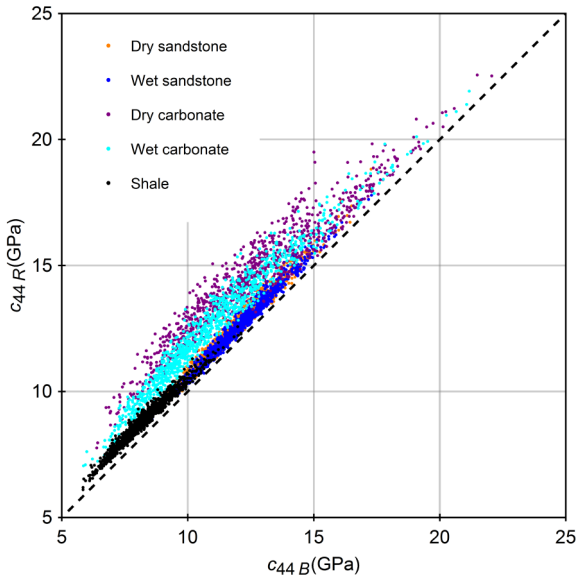

Figure 7.7 Comparison of c_{44} estimated by the Backus averaging and ray theory for different classifications of rocks. 1000 simulations are run for each types of rocks.

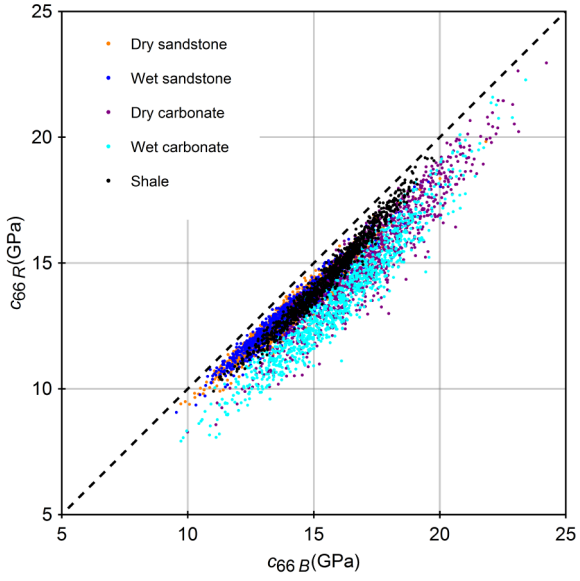

Figure 7.8 Comparison of c_{66} estimated by the Backus averaging and ray theory for different classifications of rocks. 1000 simulations are run for each types of rocks.

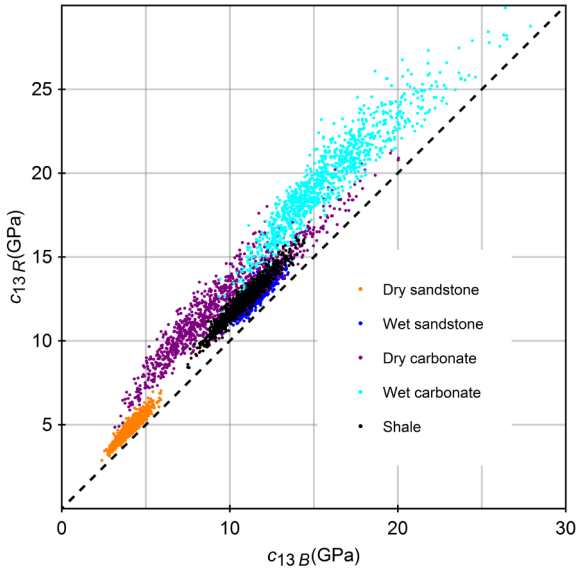

Figure 7.9 Comparison of c_{13} estimated by the Backus averaging and ray theory for different classifications of rocks. 1000 simulations are run for each types of rocks.

the Backus averaging is less than the Voigt upper bound. Another reason may be that equation (7.1) for the SH wave normal moveout is a second order Taylor approximation; whereas equation (5.1) for the P-wave normal moveout is a 4-th order Taylor approximation. Relative to the Backus averaging, c_{66} is significantly underestimated and c_{44} is overestimated by ray theory; therefore, the S-wave anisotropy parameter γ estimated by ray theory is significantly lower than estimated by the Backus averaging. Figure 7.9 shows a comparison of c_{13} estimated by the Backus averaging and ray theory. The c_{13} estimated by ray theory is generally greater than estimated by the Backus

averaging. δ is most sensitive to c_{13}. This is consistent with the fact that δ estimated by ray theory is generally greater than estimated by the Backus averaging.

Comparing the estimation of the Thomson parameters in Figures 7.1 to 7.3 and the estimation of the TI elastic constants in Figures 7.5 to 7.9, two apparent features are found. For the estimation of the Thomson parameters, the ratios of the anisotropic parameters that estimated by the Backus averaging and ray theory have little variation for the same classification of rocks. For the estimation of the TI elastic constants, the trends of overestimation or underestimation are generally parallel to the perfection estimation for the same classification of rocks. These two apparently different features should be intrinsically related.

The differences in the layering effects on seismic anisotropy that estimated by the Backus averaging and ray theory are more noticeable for the carbonate layers. It may be related to the wider distributions of the acoustic properties of the carbonate rocks in the experimental database, as can be seen from Figure 6.1. In Figure 7.10, the statistic descriptions of the randomly selected layering model are cross-plotted with the ratios of the TI elastic constants estimated by the Backus averaging and ray theory. Variation of the elastic properties of the constituent layers in the 15-layer-cake model is described by the ratio of the standard deviation and the mean of the elastic constant under study. Generally, the wider is the normalized distribution of c_{33} or c_{44} of the layer-cake model, the more the ratios deviate from 1.0; and therefore, the larger the differences between the TI elastic constants estimated by the Backus averaging and ray theory. These differences may be less significant for the real subsurface conditions. Nevertheless, the

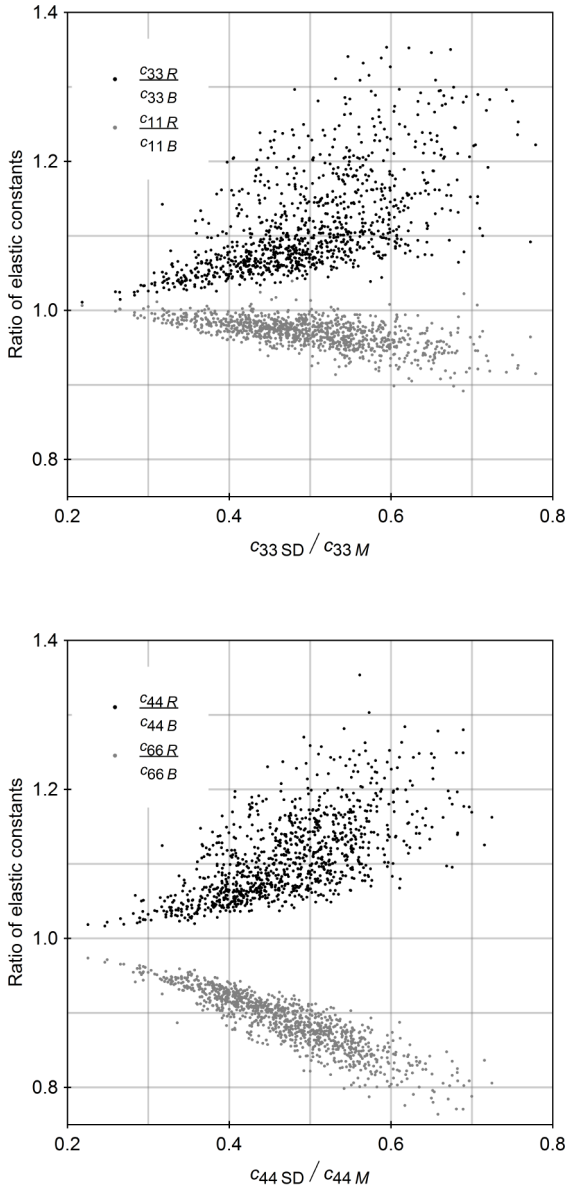

Figure 7.10 Relationship between the ratio of the TI elastic constants estimated by the Backus averaging and ray theory and the statistic parameter of the layer-cake model. 1000 simulations are run. Here the subscript "SD" denotes standard deviation and "M" denotes averaging. c_{33SD} is the standard deviation of c_{33} for different layers of the randomly selected 15-layer-cake model. Here the model parameterization uses the experimental database sandstones and carbonates.

relative differences in the estimation of ε and γ are still significant, as can be seen from Figures 7.1 and 7.2.

7.5 Frequency Limits of the Interbedding Effect on Seismic Anisotropy

One more important and realistic factor for causing seismic anisotropy may be the interbedding of shales with sandstones or carbonate rocks. To model the difference of the interbedding effect on seismic anisotropy at the low-frequency limit and high-frequency limit, the sedimentary strata is modeled by randomly selecting statistically half of the layers parameterized by the experimental database of the shale samples and the other layers parameterized by the experimental database of one classification of the isotropic rock samples. Figures 7.11 and 7.12 show the comparisons of ε and δ estimated by the Backus averaging and ray theory for different mixtures of rocks. Comparing Figure 7.11 with Figure 7.1, the difference in estimating ε for the interbedding formation is less drastic than the case of the sedimentary strata consisting of isotropic layers. Relative to the Backus averaging, underestimation of ε by ray theory generally increases with ε. The difference in estimating ε is more significant for the interbedding of shales with carbonate rocks than the interbedding of shales with sandstones. In Figure 7.12, δ is generally overestimated by ray theory and the overestimation trend is approximately parallel to the perfect match. Comparing Figure 7.12 with Figure 7.3, we can see that the thin beds of shales with intrinsic anisotropy are more important in determining the value of δ.

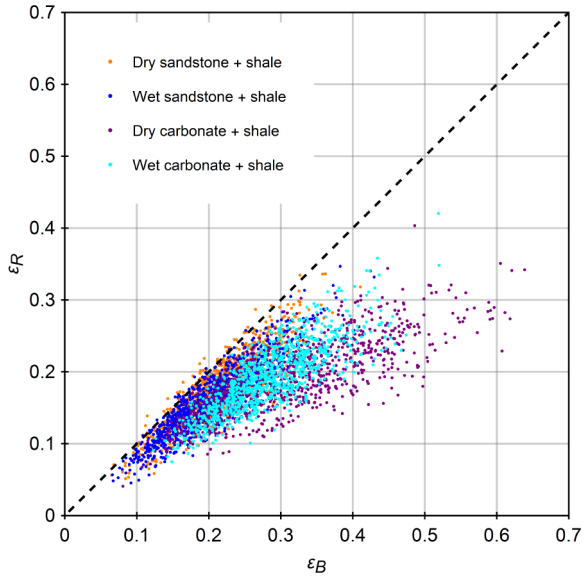

Figure 7.11 Comparison of ε estimated by the Backus averaging and ray theory for different mixtures of rocks. Each cloud of points are from 5000 simulations. Different colors represent mixture of shale with different classifications of rocks.

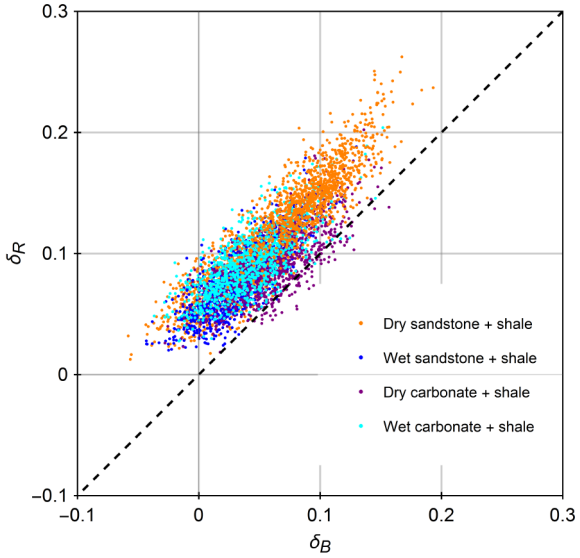

Figure 7.12 Comparison of ε estimated by the Backus averaging and ray theory for different mixtures of rocks. Each cloud of points are from 5000 simulations. Different colors represent mixture of shale with different classifications of rocks.

7.6 Conclusions

Based on Monte Carlo simulation of the sedimentary strata, the layering effects on seismic anisotropy at the low-frequency limit and at the high-frequency limit are compared. It is found that ε and γ estimated by ray theory are usually less than those estimated by the Backus averaging and δ estimated by ray theory is usually greater than estimated by the Backus average. For the sedimentary strata consisting of isotropic layers, the difference in the estimated ε and γ by ray theory and the Backus average are very significant. The difference is less significant when the layer-cake model includes shale layers with intrinsic anisotropy.

7.7 Acknowledgements

We would like to thank the Fluid and DHI consortium sponsors for the financial support.

7.8 References

Alkhalifah T. and Tsvankin I. 1995. Velocity analysis for transversely isotropic media. *Geophysics* **60**, 1550-1566.

Alkhalifah T. 1997. Velocity analysis using nonhyperbolic moveout in transversely isotropic media. *Geophysics* **62**, 1839-1854.

Anderson D.L. 1961. Elastic wave propagation in layered anisotropic media. *Journal of Geophysical Research* **66**, 2953-2963.

Backus G.E. 1962. Long-wave elastic anisotropy produced by horizontal layering. *Journal of Geophysical Research* **67**, 4427-4440.

Helbig K. 1984. Anisotropy and dispersion in periodically layered media. *Geophysics* **49**, 364-373.

Hovem J.M. 1995. Acoustic waves in finely layered media. *Geophysics* **60**, 1217-1221.

Marion D., Mukerji T. and Mavko G. 1994. Scale effects of velocity dispersion: From ray to effective medium theories in stratified media. *Geophysics* **59**, 1613-1619.

Potel C., de Belleval J.F. and Gargouri Y. 1995. Floquet waves and classical pane waves in an anisotropic periodically multilayered medium: Application to the validity domain of homogenization. *Journal of the Acoustical Society of America* **97**, 2815-2825.

Postma G.W. 1955. Wave propagation in a stratified medium. *Geophysics* **20**, 780-806.

Shapiro S.A., Zien H. and Hubra P. 1994. A generalized O'Doherty-Anstey formula for waves in finely layered media. *Geophysics* **59**, 1750-1762.

Silva M. B. C. and Stovas A. 2009. Correspondence between the low- and high-frequency limits for anisotropic parameters in a layered medium. *Geophysics* **74**, WA25–WA33.

Stovas A. and Ursin B. 2007. Equivalent time-average and effective medium for periodic layers, *Geophysical Prospecting* **55**, 871-882.

Tsvankin, I. 2005. *Seismic Signatures and Analysis of Reflection Data in Anisotropic Media*, 2nd ed. Elsevier.

Tsvankin, I. 2012. *Seismic Signatures and Analysis of Reflection Data in Anisotropic Media*, 3rd ed.: SEG.

Wang L. and Roklin S.I. 2002. Floquet wave ultrasonic method for determination of single ply moduli in multidirectional composites. *Journal of the Acoustical Society of America.* **112**, 916-924.